Photonic Crystal Slab Sensors in Microfluidics

Sørensen, Kristian Tølbøl

Publication date:
2018

Document Version
Publisher's PDF, also known as Version of record

Citation (APA):
Sørensen, K. T. (2018). *Photonic Crystal Slab Sensors in Microfluidics*. DTU Nanotech.

Photonic Crystal Slab Sensors in Microfluidics

Kristian Tølbøl Sørensen
PhD Thesis Januaray 2017

DTU Nanotech
Department of Micro- and Nanotechnology

DTU Nanotech
Department of Micro- and Nanotechnology

Technical University of Denmark

Kristian Tølbøl Sørensen

Photonic Crystal Slab Sensors in Microfluidics

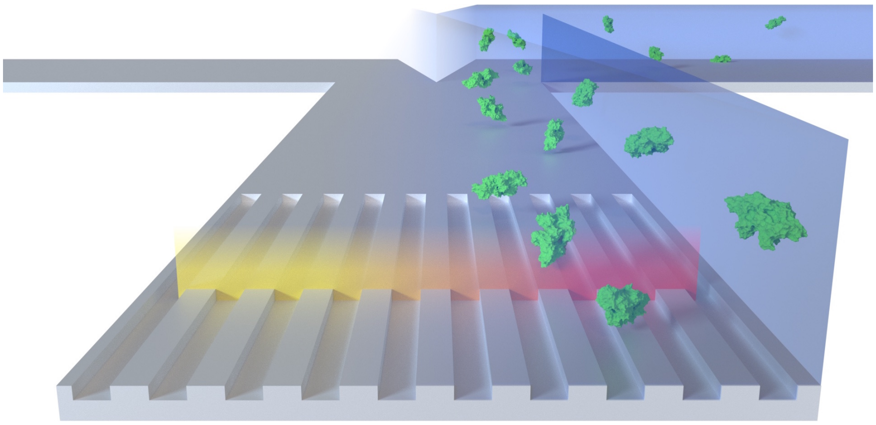

PhD thesis
January 2018

to Julie

Abstract

THIS Ph.D. thesis discusses the design and application of so-called photonic crystal slab (PCS) sensors, with an emphasis on microfluidic integration. PCS sensors can measure the refractive index of fluids, which makes them universal in the sense that almost any change to a fluid will alter its refractive index. The underlying phenomenon is called guided-mode resonance (GMR), which responds to changes in the refractive index of fluids only within the first few hundred nanometers from the sensor surface. PCS sensors can be fabricated entirely out of polymers, and read out using instrumentation as simple an LED and a photo diode. This work has thus far resulted in three manuscripts and one patent, which are attached.

The first manuscript, which has been submitted to Computer Physics Communications, describes an open-source algorithm, which integrates with many electromagnetics simulation tools to provide adaptive resolution. This algorithm can routinely make GMR simulations more than 100 times faster.

The second manuscript, submitted to Optics Express, describes the practical application of polymeric PCS sensors. As with any refractive index sensor, the devices are highly sensitive to temperature drift and fluctuations. We demonstrate a facile method for real-time compensation of these thermal disturbances.

The third manuscript, which has been published in Micromachines, concerns the integration of PCS sensors into a microfluidic H-filter. We show that by monitoring the refractive index (and thus concentration) gradient, the diffusion length of molecules in flow can be determined.

PCS sensors have been in development for the last few decades, and both readout systems and sensor substrates are commercially available. However, products on the market predominantly target high-end applications such as pharmaceutical development, where their high pricetags are justifiable. In order to lower the entry barrier of the technology, we patented what is currently being marketed as The NanoCuvette, a spectrophotometer cuvette with an embedded PCS sensor. Along with user-friendly software, this enables the use of an existing, unmodified spectrophotometer to make refractometric measurements, such as bulk concentration measurements on non-absorbing compounds. This effectively lowers the entry barrier for PCS sensors from tens of thousands of euros to tens of euros.

Resumé

DENNE Ph.D.-afhandling omhandler design og anvendelse af såkaldte fotonisk krystal sensorer, med særligt fokus på indlejring i mikrovæske-systemer. Disse sensorer kan måle hvordan væsker bryder lys, væskens brydningsindeks, og fordi enhver ændring i en væske vil påvirke brydningsindekset, kan sensorerne bruges indenfor utallige anvendelsesområder. For eksempel indenfor lægemiddelindustrien, hvor det præcise indhold af et bestemt stof i en opløsning er yderst vigtigt. Sensoren måler kun indenfor de første par hundrede nanometer fra sensorens overflade, og kan fremstilles udelukkende af polymerer, hvilket gør dem yderst konkurrencedygtige på prisen. Da sensorerne udlæses med udstyr så simpelt som et par lysdioder, kræves der heller ikke dyrt udstyr til for at anvende dem.

Ud af arbejdet er der foreløbigt kommet tre manuskripter og ét patent, som er vedlagt afhandlingen: Det første manuskript, som er blevet indsendt til tidsskriftet *Computer Physics Communications*, beskriver en open-source algoritme, som kan integreres med mange værktøjer til simulation af elektromagnetisme, såsom *GD-Calc* pakken. Algoritmen tilpasser simulationens opløsning dynamisk, og i mange tilfælde kan den gøre sensor-simulationer hundrede gange hurtigere.

Det andet manuskript, indsendt til *Optics Express*, beskriver anvendelsen af polymersensorerne i praksis og de udfordringer der kan opstå. Som enhver anden brydningsindekssensor er disse polymersensorer særligt følsomme for udsving i temperatur. Vi viser i manuskriptet en simpel metode, der direkte kan kompensere for sådanne udsving i temperatur.

Det tredje manuskript, som er udgivet i tidsskriftet *Micromachines*, handler om indlejring af sensorerne i et såkaldt H-filter. I manuskriptet viser vi at det derved bliver muligt at bestemme molekylers diffusionslængde, idet de indlejrede sensorer kan afsløre formen på stoffers koncentrations-profil.

Fotonisk krystal sensorer har været under udvikling i nogle årtier, og både sensorerne og deres udlæsnings-systemer er efterhånden kommet i handlen. Produkterne på markedet henvender sig dog mest til mere eksklusive anvendelser, såsom udvikling af nye lægemidler, hvor et højt prisniveau kan forsvares. For at sænke teknologiens indgangsbarriere, har vi patenteret hvad der markedsføres som en NanoCuvette, en væskebeholder med en indbygget fotonisk krystal sensor. Den kan bruges i et standard spektrofotometer, og sammen med brugervenlig software gør NanoCuvette det muligt at måle på stoffer, som ellers ikke absorberer lys. Dette sænker effektivt indgangsbarrieren for teknologien fra nogle hundrede tusinde kroner, til nogle hundrede kroner.

Preface

THIS thesis is submitted in partial fulfillment of the requirements for acquiring the Ph.D. degree at the Technical University of Denmark (DTU). The work was partially funded by the Danish Council for Strategic Research (DSF)[1] and was supervised by Professor Anders Kristensen, to whom I am grateful for suggesting I “stepped outside the comfort zone” and grapple with the realm of nanophotonics, and for enthusiastically supervising the project from start to finish. I am also grateful to Christoph Vannahme for his excellent supervision during the first year of the Ph.D. Likewise, for the first year, my former office mate Pétur Gordon Hermannsson essentially acted as another co-supervisor and first introduced me to nanophotonics theory.

I am furthermore grateful to the current and former members of the Optofluidics group for their talent and friendly nature, and especially to my current office mate Chen Zhou for his support, both scientifically and morally. Darmin Catak has also been particularly helpful with injection molding of chips and early testing of ultrasonic bonding. I also wish to acknowledge Rodolphe Marie, who has acted as a bit of a mentor on the sideline, and to Emil Højlund-Nielsen for introducing me to rigorous coupled-wave analysis (RCWA), which has been quite useful in my project. Many student helpers have been involved from time to time, primarily assisting with the somewhat tedious microfabrication of sensors: thank you, Sigurd Friis Truelsen, Andreas Spandet Havreland, Ardeshir Esteki, Dorte Rubæk Danielsen, Kirstine Engell Sandager Nielsen, Sophie Kargo, and Oseze Esther Iyore!

Over the years, much time has been spent trying out new potential applications for the sensors used in this work. As it is often the case in science, many alleys turn out to be blind, but now and then, a path turns out to be feasible. Whether or not our endeavors bore fruit, I am grateful to the collaborative efforts I have shared with Martin Dufva, Marie Louise Laub Busk, Andreas Hjarne Kunding, Ioannis Chronakis, Ana Carina Loureiro Mendes, Karen Stephansen, Kaare Hartvig Jensen, Lars Peter Nielsen, Per Jørgensen, and Line Hagner Nielsen.

At the time of writing, one patent and three manuscripts result from this Ph.D. project. To allow the thesis to be read independently from the manuscripts, central paragraphs have been reproduced verbatim where suitable.

During this project, I have had the pleasure of co-supervising two master’s theses together with Line Hagner Nielsen, from whom I have learned much about supervision. The two hard-working master’s students Charlotte Bonde Ingvorsen and Marco Crosio also deserve special

---

[1] under Grant Agreement No. 10-092322 (PolyNano).

mentioning, as their work has contributed directly to this thesis. I also enjoyed co-supervising Neethu Mariam Mathew and Ardeshir Esteki in shorter projects.

About midway through the Ph.D. project, Emil Højlund-Nielsen, Anders and I filed a patent for a sensor-integrated cuvette that allows a standard spectrophotometer to now also measure concentrations of non-absorbing liquids. This paved the way for a proof-of-concept grant from DTU and a 5-month leave of absence from my Ph.D. to participate in the Danish Tech Challenge. Along with Emil and Thomas Tølbøl Sørensen, I learned a great deal about the business side of science, and I am grateful to them and the rest of the Copenhagen Nanosystems team for their persistence and patience while I returned to and finished my thesis.

Finally, I am highly grateful to my friends, family and Julie, for their support and understanding of my periodically being off the grid. Without you, this thesis would not have come to be.

Kristian Tølbøl Sørensen
Copenhagen, January 2018

List of publications

Journal papers

1. **Kristian Tølbøl Sørensen** and Anders Kristensen. Label-Free Monitoring of Diffusion in Microfluidics. *Micromachines*, 8(11):1-7, 2017.
2. **Kristian Tølbøl Sørensen**. asasim: Adaptive Sampling for Electromagnetic Simulations. Submitted to *Computer Physics Communications*.
3. **Kristian Tølbøl Sørensen**, Charlotte Bonde Ingvorsen, Line Hagner Nielsen, and Anders Kristensen. On the practical achievement of high performance using a polymeric photonic crystal slab sensor. Submitted to *Optics Express*.

Patent applications

4. **Kristian Tølbøl Sørensen**, Emil Højlund-Nielsen, and Anders Kristensen. Cuvette and Method for Measuring Refractive Index in a Spectrophotometer. International application number WO 2017/129196 A1.

Contributions to other work

5. Pétur G. Hermannsson, Christoph Vannahme, Cameron L.C. Smith, **Kristian Tølbøl Sørensen**, and Anders Kristensen. Refractive index dispersion sensing using an array of photonic crystal resonant reflectors. *Applied Physics Letters*, 107(6):061101-1–4, 2015.
6. Pétur G. Hermannsson, **Kristian Tølbøl Sørensen**, Christoph Vannahme, Cameron L.C. Smith, Jan J. Klein, Maria-Melanie Russew, Gabi Grützner, and Anders Kristensen. All-polymer photonic crystal slab sensor. *Optics Express*, 23(13):16529–16539, 2015.
7. **Kristian Tølbøl Sørensen**, Joanna M. Lopacinska, Niels Tommerup, Asli Silahtaroglu, Anders Kristensen, and Rodolphe Marie. Automation of a single-DNA molecule stretching device. *Review of Scientific Instruments*, 86(6):063702-1–6, 2015.
8. Christoph Vannahme, **Kristian Tølbøl Sørensen**, Carsten Gade, Martin Dufva, and Anders Kristensen, Refractometric monitoring of dissolution and fluid flow with distributed feedback dye laser sensor. *Optics Express*, 23(5):6562–6569, 2015.

9. Joanna M. Łopacińska-Jørgensen, Jonas N. Pedersen, Mads Bak, Mana M. Mehrjouy, **Kristian Tølbøl Sørensen**, Peter F. Østergaard, Brian Bilenberg, Anders Kristensen, Rafael J. Taboryski, Henrik Flyvbjerg, Rodolphe Marie, Niels Tommerup, and Asli Silahtaroglu. Enrichment of megabase-sized DNA molecules for single-molecule optical mapping and next-generation sequencing. *Scientific Reports*, 7(1):17893-1–10, 2017.

Oral conference presentations

10. **Kristian Tølbøl Sørensen**, Andreas S. Havreland, Sigurd F. Truelsen, Pétur G. Hermannsson, Christoph Vannahme, and Anders Kristensen. Nanoimprinted photonic crystal slab sensor for label-free diffusion monitoring. Oral presentation given at *the 41st International Conference on Micro and Nano Engineering (MNE)*, 2015, Haag, The Netherlands.
11. **Kristian Tølbøl Sørensen**, Chen Zhou, and Anders Kristensen. Label-Free Sensing in Optofluidics. Invited oral presentation given at *the 37th Progress In Electromagnetics Research Symposium (PIERS)*, 2016, Shanghai, China.

Contents

List of Figures

List of Tables

Nomenclature

Acronyms

Note: In the digital version of this thesis, permanently available at kristian.tolbol.dk/phd.pdf, most pdf-readers can display the meaning when hovering the mouse over an acronym.

BIA	biomolecular interaction analysis
BOM	bill of materials
BSA	bovine serum albumin
CAD	computer-aided design
CMOS	complementary metal-oxide semiconductor
COC	cyclic oleofin copolymer
CPU	central processing unit
DFB	distributed feedback
DLS	dynamic light scattering
DMR	dynamic mass redistribution
DSC	differential scanning calorimetry
DSF	the Danish Council for Strategic Research
DTU	the Technical University of Denmark
ELISA	enzyme-linked immunosorbent assay
FDTD	finite-difference time-domain
FDTS	perfluorodecyltrichlorosilane
FSR	free spectral range
GI	gastro-intenstinal
GMR	guided-mode resonance
HTS	high-throughput screening
IBSD	ion-beam sputter deposition
IDUN	Center for Intelligent Drug Delivery and Sensing Using Microcontainers and Nanomechanics
ITC	isothermal titration calorimetry
ITO	indium tin oxide
LDLS	laser-driven light source
LOC	lab-on-a-chip
MEMS	micro-electromechanical systems
MFCS	microfluidic flow control system
MVD	molecular vapor deposition
NIL	nanoimprint-lithography
NMR	nuclear magnetic resonance
OWLS	optical waveguide lightmode spectroscopy

PCS photonic crystal slab

PDMS polydimethylsiloxane

PEG polyethylene glycol

PMMA poly(methyl methacrylate)

POC point of care

PSO particle swarm optimization

PWV peak wavelength value

QCM quartz crystal microbalance

RCWA rigorous coupled-wave analysis

RIE reactive ion etching

RLT residual layer thickness

RMS root-mean-square

RWG resonant waveguide grating

SEM scanning electron microscope

SERS surface-enhanced Raman scattering

SNR signal-to-noise ratio

SPR surface plasmon resonance

TE transverse electric

TM transverse magnetic

TMAH tetramethylammonium hydroxide

UV ultraviolet

VASE variable angle spectroscopic ellipsometry

Symbols

a translation distance

A absorption

α extinction coefficient

c concentration

C constant

χ channel fraction

D diffusion coefficient

$\Delta\lambda$ free spectral range

e the Euler number

$\hat{e}$ penetration depth

ϵ permittivity

η viscosity

F duty cycle

F_0 Fourier modulus

γ peak half-width

h channel height

i index

I intensity

k_B the Boltzmann constant

l path length

L channel length

L_e entrance length

λ wavelength

λ_r resonance wavelength

Λ grating period

n count

n_D	refractive index at the sodium D-line (589 nm)
$n_{\mathbf{eff}}$	effective refractive index
n_1	superstrate refractive index
n_2	waveguide core refractive index
n_3	substrate refractive index
N_A	the Avogadro constant
NA	numerical aperture
m	mode order
Q	flow rate
R	reflectance
r^2	coefficient of determination
$r_{\mathbf{hyd}}$	hydrodynamic radius
$R_{\mathbf{hyd}}$	hydraulic resistance
S	sensitivity
σ	standard deviation
t	time
T	temperature
v	velocity
w	width
x	coord. across channel, parallel to sensor
$\bar{x}$	diffusion length
y	coord. along channel, parallel to sensor
z	coord. orthogonal to sensor
ζ	sensitivity-weighted velocity

Chapter 1

Introduction

For better or worse, technological advances have redefined every aspect of our lives, from how we move and eat to how we communicate and socialize. Many diseases that previously plagued humanity have been all but eradicated from industrialized countries, by the power of modern vaccines. At the doctor, we can have our biological samples sent to centralized laboratories, which can diagnose for a plethora of pathogens. One area of intense current research, is that of diagnostic tests which can be performed at the point of care (POC) [1]. These allow an instant diagnose, such that appropriate treatment can be initiated immediately. Furthermore, as facilities and trained personnel is at a shortage in many developing countries, POC devices could bring state of the art healthcare one step closer to those locations [2]. The requirements for storage and personnel also make current vaccines largely unavailable in the poorest regions, where people suffer from common diseases against which vaccines exist. This is one reason why much effort is directed towards drug delivery systems. If the active ingredients of vaccines could be stored in the form of tablets, oral vaccines could be realized [3], which might benefit developing countries. By similar mechanisms that could make a drug survive the harsh environment of the gastro-intenstinal (GI) tract, drug deliveryystems also hold great promise for the delivery of drugs to the relevant sites within the human body. This outlook is particularly in demand for the treatment of cancer, the great killer in industrialized countries. A drug delivery system capable of releasing a potent drug at the exact site necessary is sometimes referred to as the “magic bullet”, the holy grail of nanobioscience.

Whether for diagnostic tests or for technological progress in general, sensor technologies play a pivotal role. Our understanding of the immune system has revolutionized not only medicinal treatment, but also diagnostics. The immune system detects a foreign invader by recognizing a characteristic part of it, known as an antigen. This triggers the production of antibodies, which are proteins that recognize that particular antigen. By harvesting antibodies and immobilizing them, a surface is created which can recognize a particular pathogen with incredible affinity. This is the basis of enzyme-linked immunosorbent assay (ELISA) [4], an essential workhorse of diagnostics and biotechnology alike. In order to tell whether an antigen has been bound, a secondary antibody can be added, which produces, e.g., a fluorescent signal. If the antigen is present, the fluorophore lights up when illuminated in a particular manner. When the antigen is absent, the reporter antibody has nothing to bind to, and is washed away. However, the need for labelling makes the process more slow, com-

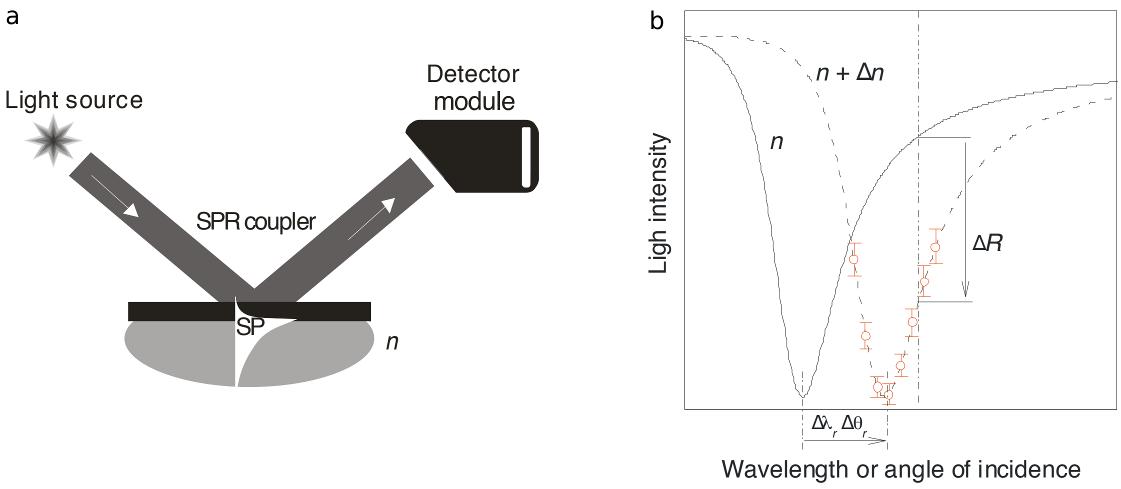

Figure 1.1. Basic principle of surface plasmon resonance (SPR). When a) light shines onto the SPR surface through a coupling element such as a prism, b) the resonance wavelength or angle shifts in response to changes in sample refractive index, n. Adapted from ref. [10].

plex and expensive. Label-free biosensors promise the same sensitivity as traditional assays [5], but without the needed for labelling. Apart from the improvements this might impart on existing diagnostic methods, label-free sensing also opens the door to lab-on-a-chip (LOC) devices which can be used at the POC. With LOC devices, developing countries could finally access state of the art diagnostics without the need for a specialized laboratory with trained personnel.

This thesis describes work on the integration of label-free sensors into microfluidics as step toward LOC devices, in the context of the state of the art of the field as presented in this chapter. First, we will look at the tip of the nanophotonics literature iceberg.

1.1 Light

A plethora of sensor technologies exist which do not rely on labelling with fluorescent, magnetic or radioactive tags. Examples include quartz crystal microbalance (QCM) [6, 7], electrochemical detection via impedance spectroscopy [8], and surface acoustic wave biosensors [9]. However, optical sensors have the unique advantages of contact-free coupling and the potential for cheap fabrication. The field of optical sensors itself contains a large number of sensor types, including surface plasmon resonance (SPR) [10], optical waveguide lightmode spectroscopy (OWLS) [11], surface-enhanced Raman scattering (SERS) [12], distributed feedback (DFB) laser sensors [13], and photonic crystal slab (PCS) sensors [14].

SPR has become the most widespread optical sensor platform [15, 16, 10], and relies on the excitation of surface plasmons on a metallic surface layer, typically gold. The principle is shown in figure 1.1. The excitation light must be coupled via a prism or a grating, which is a disadvantage of the method. By modulating the angle of incidence θ or the wavelength

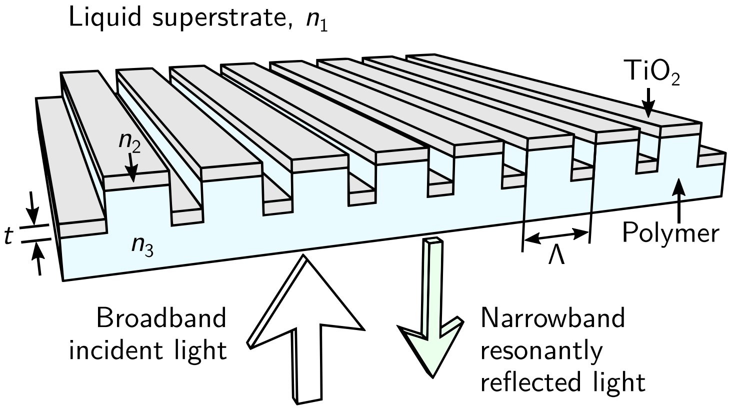

Figure 1.2. Schematic illustration of photonic crystal slab (PCS) sensor. Illumination with white light at normal incidence gives rise to a narrow resonant reflection. The resonance wavelength λ_r shifts with changes in superstrate refractive index n_1. From ref. [25].

of light λ, the resonance angle θ_r or resonance wavelength λ_r [16] can be determined. This value depends on the refractive index n very close to the surface, on the order of ~100 nm. Therefore, when an antigen binds to an immobilized antibody, the density and thus refractive index changes, shifting the readout signal. This has been extensively used for biomolecular interaction analysis (BIA) [16].

As alternatives to SPR, many optical sensor technologies are based on photonic crystals. These meta-materials have structures that are smaller than the wavelength of visible light (approx. 400 nm to 700 nm), and are therefore also referred to as sub-wavelength structures. Furthermore, because they restrict the propagation of certain colors of light, they are said to have an optical bandgap. With proper design, a PCS can be engineered to resonantly reflect a very narrow range of wavelengths, using a phenomenon referred to as guided-mode resonance (GMR) [17]. The principle is illustrated in figure 1.2. Like in SPR, the resonantly reflected wavelength λ_r is highly sensitive to the refractive index very close to the surface, making it suitable for biosensing. In this way, PCS sensors have been used to monitor the dynamic mass redistribution (DMR) of cells [18, 19, 20], adhesion of bacteria [21], growth of monolayers [15], and detection of biomarkers [22, 23] or single nano-particles [24].

Fabrication of nanostructured surfaces is quite an engineering feat made possible by the technological development of micro-electronics. As the number of transistors in integrated circuits have been doubling every two years for decades, in accordance with Moore's law, transistors have gone from millimeters to nanometers. These same micro- and nanofabrication methods are now being employed to fabricate sub-wavelength structures capable of taming light. In general, PCS sensors consist of a low-refractive index substrate, a high-refractive index core layer, and a sub-wavelength grating. The substrate can be made of materials such as glass [18], polymer [26] or sol-gel [15]. Examples of core layer materials include titania (TiO_2) [15, 22, 23, 27, 14], hafnium dioxide (HfO_2) [28, 27], tantalum pentoxide (Ta_2O_5) [18], indium tin oxide (ITO) [18], diamond-like carbon [29] or polymer [26]. The nanostructured grating is typically defined by nanoimprint-lithography (NIL) using a stamp produced by electron-beam lithography [25], laser-interference lithography and etching [18], by injection molding [23] or roll-to-roll imprinting [14].

Because PCS sensors confine light very tightly, also laterally, they also have uses for imag-

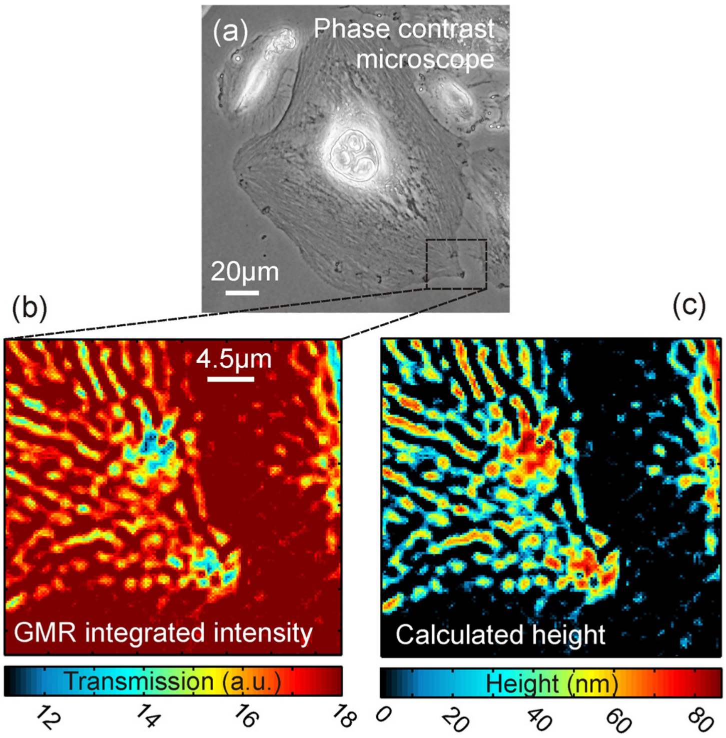

Figure 1.3. Fibroblast cell imaged on a sensor substrate, using a standard microscope. a) Brightfield-image of the full cell. b) A smaller part is imaged by merit of the PCS substrate. c) With proper calibration, the resonant signal can be converted into a height measurement. From ref. [18].

ing. Using an imaging spectrometer and a motorized stage, the surface can be scanned to record a refractometric image [24]. However, the frame rate is limited by the stage movement speed. Alternatively, it has been demonstrated that using multi-periodic nanostructures along with a cylindrical lens, a refractometric image can be assembled with no moving parts [30]. When the readout parameter is intensity rather than wavelength or angle, a standard color camera can even be used instead of expensive spectrometers [22]. By integrating a PCS on a microscope slide, 3D-imaging has been demonstrated using a standard optical microscope [18], as shown in figure 1.3. For imaging relatively thick cell layers, the evanescent decay length of the sensor can be a limitation. Although it can be tuned by the design of the photonic crystal, it is difficult for the penetration depth to exceed a few hundred nanometers [31]. However, when the substrate refractive index is lower than that of the superstrate, known as a reverse symmetry, the penetration depth has no upper limit [21]. This can be achieved, e.g., using nanoporous silica as substrate, which has a low refractive index of $n_D = 1.19$ [32]. These demonstrations of label-free sensing could open new doors within biotechnology, and even for traditional fluorescence microscopy, PCS substrates can play a role by enhancing the fluorescence intensity [33].

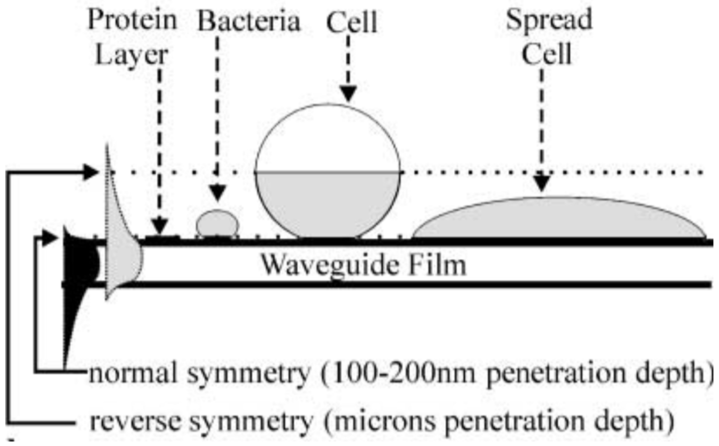

Figure 1.4. Reverse symmetry waveguide principle. The lower substrate refractive index allows the penetration depth to far exceed that of normal symmetry sensors. From ref. [31].

1.2 Liquid

The world of microfluidics is fascinatingly different from fluids on an everyday scale. Modern microfabrication allows the creation of channels with a diameter that is a fraction of a human hair, and fluids flowing in such narrow channels are virtually unaffected by the force of gravity. Instead, forces that are quite weak on our macroscopic scale, become dominating on the microscopic scale. An example is capillary forces, that cause water in a glass cup to climb slightly up the sides of the glass, maybe by a few millimeters. When the vessel containing the liquid shrinks to the microscopic scale, however, the effect can carry water more than 100 meters into the air, to the leaves of the world's largest trees.

Whereas nature has been self-assembling intricate networks of fine, microfluidic channels for hundreds of millions of years, microfluidics systems are a relatively recent branch of man-made objects. The first capillary experiments were conducted by Hagen and Poiseuille almost 180 years ago, but microfluidics was not put into practical use until the advent of microfabrication technology for micro-electromechanical systems (MEMS) in the 1980s [34]. Today, microfluidics biosensors are available in many supermarkets, in the form of pregnancy tests [20], and many novel microfluidics applications are sprouting up in the scientific community. Although pressure is commonly used to drive the flow, a certain branch has a particularly large overlap with the strategy employed by trees: paper microfluidics. Exemplified in figure 1.5, a simple microfluidic system can be produced from paper (nitrocellulose membranes) [2], with a potentially miniscule cost price.

Evolution has produced the highly efficient and specialized enzymes which all contemporary life relies on. We artificially harness the power of enzymes whenever we wash our clothes or brush our teeth, and baking and brewing would not be possible without them. Nature has been optimizing these enzymes for billions of years through natural selection. Most random mutations result in an enzyme that performs worse than the wildtype, but every now and then, a mutation occurs which improves it ever so slightly. This is also the basis of directed evolution, made possible by microfluidics and high-throughput screening (HTS). Pi-

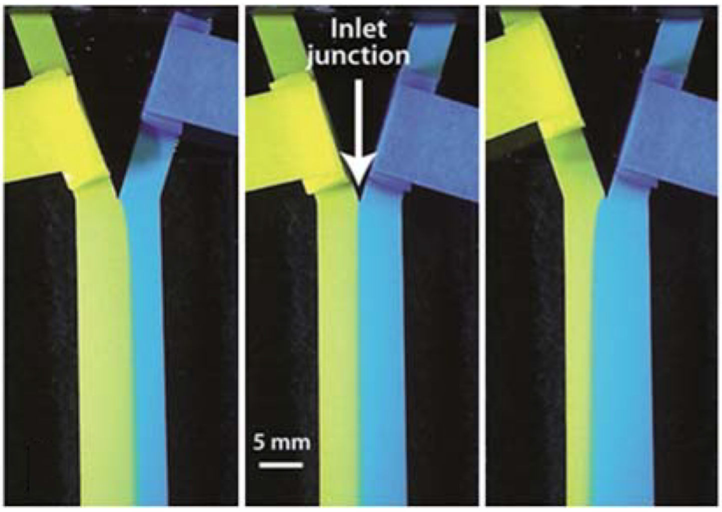

Figure 1.5. Example of paper microfluidics. Capillary flow drives two dyed liquids through the paper network. From ref. [2].

coliter droplets containing mutated genes and the enzymes they express can be screened for enzyme activity [35]. By artificially selecting beneficial mutations, directed evolution seeks to accelerate the evolution of superior enzymes to meet concrete industrial challenges.

The ability of droplet microfluidics to compartmentalize miniscule reagent volumes has a wide array of applications besides directed evolution. Other prominent examples include x-ray crystallography in droplets [37], droplet-based bioassays [36] (figure 1.6) and digital microfluidics through electrowetting [34].

When a small particle in water is observed in a microscope, it appears to be constantly bouncing around in a random walk. This is referred to as brownian motion, and is caused by incessant collisions between the particle and surrounding water molecules. This behavior not only applies to observable particles, but also to non-observable molecules. The propensity of molecules to gradually spread out from a region of high concentration, is referred to as diffusion. Einstein showed that the average diffusion distance scales with the square root of time, and so diffusion is incredibly fast on small length scales, and incredibly slow on long length scales: on average, it takes a sugar molecule about 0.1 ms to diffuse 1 µm, but about 16 min to diffuse 1 mm. In a microfluidics system, where channel dimensions are typically quite small, diffusion is therefore an essential process. Deliberately designed microstructures can ensure turbulent mixing in a microfluidics segment, but otherwise, devices are commonly operated under laminar flow conditions, such that convective mixing does not occur. The first [34] practical application of controlling diffusion in a laminar flow was done in order to fractionate proteins, as demonstrated by Giddings et al. in 1976 [38]. Proteins are large molecules which diffuse slowly, and diffusivity is therefore often rate-limiting in microfluidics applications [39]. Microfluidics architectures can be designed with diffusive properties in mind when diffusion data is available, but this is often not the case. To measure diffusivity, a number of techniques are available, including the Aris-Taylor method [40], the diaphragm-cell method [41], using light scattering [42], nuclear magnetic resonance (NMR) [43, 44] or the

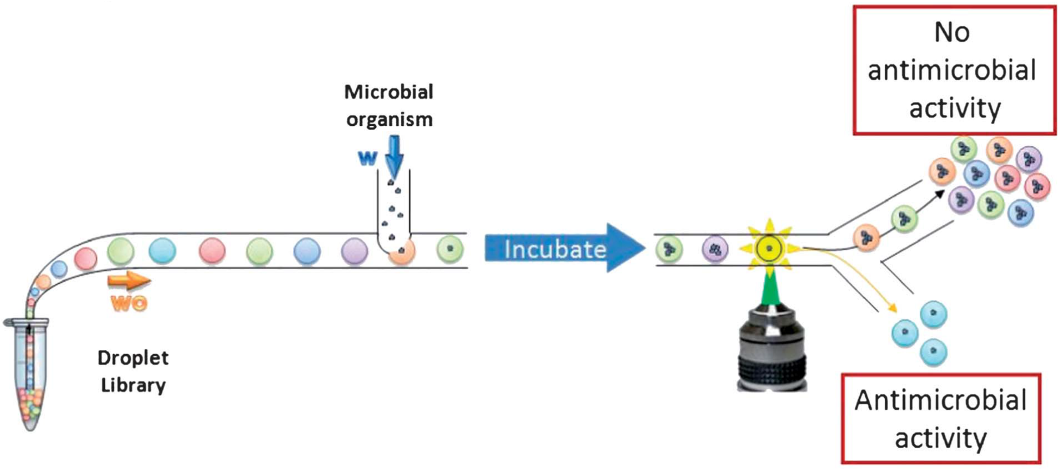

Figure 1.6. Bioassay realized in microfluidic droplets. From ref. [36].

peak parking (synonymous with arrested flow- or stopped flow-) methods [45]. The stopped-flow method requires stopping the flow for 4 min to 8 min [46] to observe nnnnthe diffusive broadening, delaying readout. In general, measuring diffusion coefficients of spectrally inactive compounds is rarely straight-forward.

Outline

The state of the art in the fields of PCS sensors and microfluidics hereby introduced form the context of this work. The next two chapters respectively provide the theoretical and methodological foundation, upon which the following four chapters build: First, a conceptually simple method for improving efficiency of electromagnetic simulations is presented. Next, the sensor platform is optimized in multiple aspects, from readout instrumentation to analysis algorithms. Then, the optimized sensors are integrated into microfluidics to allow direct diffusion monitoring. Finally, biologically relevant sensor applications are investigated. In the last chapter, an overall conclusion and outlook is provided.

Chapter 2

Theoretical concepts

THE theoretical framework for PCS sensors has been laid gradually throughout times, with a first examination of this “most remarkable grating” [47] by R. W. Wood in 1902. He observed what would later be referred to as Wood’s anomaly, and proposed it as a new method for aligning to normal incidence. He also observed a red-shifting of the resonance wavelength upon diffusing glycerol into water in a 300 µm thin channel, thereby arguably demonstrating the world’s first PCS sensor-integrated microfluidics system. In 1992, Magnusson and Wang proposed “a basic new optical element” [17], namely a GMR filter, one of many synonyms for PCS sensors, as they are referred to here (in part, in order to avoid confusion with microfluidic H-*filters*). Another popular term is resonant waveguide gratings (RWGs) [19, 48, 49, 20], but they all refer to the same. This chapter introduces the theory necessary to understanding the following chapters, with an emphasis on PCS sensors and microfluidics. As both these topics are tremendously deep, only the essentials needed in the context of this project’s experimental work are provided. Where nothign else is stated, the equations governing light are based on ref. [50], whereas those governing liquid is based on ref. [51].

2.1 Nanophotonics

A slab waveguide is illustrated in figure 2.1, which for the sake of simplicity is symmetric, i.e., it has the same refractive index n_1 on both sides of the core, which has a refractive index n_2. With this notation, the refractive index as a function of spatial coordinate x can be written

$$n(x) = \begin{cases} n_2 & \text{if } |x| < d/2 \\ n_1 & \text{otherwise} \end{cases} \tag{2.1}$$

2.1.1 Transverse electric modes

By definition, a mode has a well-defined field amplitude at each point in space and time [50]. Transverse electric (TE) modes have their electrical field in perpendicular to the plane of incidence, i.e., along the y-axis of figure 2.1. The amplitude of the electric field is

$$E_y(x,z,t) = E_m(x)\exp\big(i(\omega t - \beta z)\big) \tag{2.2}$$

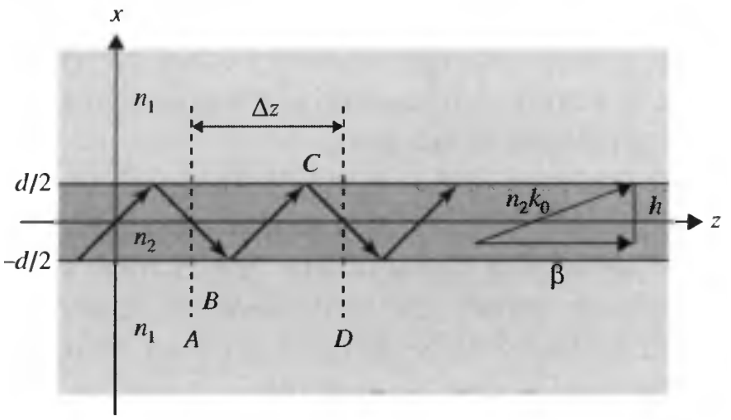

Figure 2.1. Schematic representation of a symmetric slab waveguide.

where $\omega = 2\pi f$ is the angular frequency, β is the mode propagation constant, and E_m is the wave function of the m'th mode, given as

$$E_m(x) = \begin{cases} A\sin hx + B\cos hx & \text{if } |x| < d/2 \\ C\exp(-qx) & \text{if } x > d/2 \\ D\exp(qx) & \text{if } x < -d/2 \end{cases} \tag{2.3}$$

Here, A, B, C, and D are constants, while h and q are given by

$$h = \sqrt{\left(\frac{n_2\omega}{c}\right)^2 - \beta^2} \tag{2.4}$$

$$q = \sqrt{\beta^2 - \left(\frac{n_1\omega}{c}\right)^2} \tag{2.5}$$

where c is the speed of light in vacuum. These equations are related through

$$\tan(hd) = \frac{2hq}{h^2 - q^2} \tag{2.6}$$

Normalization of the propagation constant yields n_{eff}, the effective refractive index of the mode:

$$n_{\text{eff}} = \frac{\beta}{\omega/c} = \frac{c}{v_p} \tag{2.7}$$

where v_p is the phase velocity. When a mode is confined, it has en effective refractive index somewhere between the values of the core and cladding,

$$n_{\text{clad}} < n_{\text{eff}} < n_{\text{core}} \tag{2.8}$$

2.1.2 Transverse magnetic modes

As both TE- and transverse magnetic (TM)-mode devices are employed in this work, a similar account will now be given for guided TM modes. These modes have their magnetic field perpendicular to the plane of incidence, with field amplitudes

$$\begin{aligned} H_y(x,z,t) &= H_m(x)\exp\big(i(\omega t - \beta z)\big) && (2.9)\\ E_x(x,z,t) &= \frac{i}{\omega\mu}\frac{\partial}{\partial z}H_y && (2.10)\\ E_z(x,z,t) &= -\frac{i}{\omega\mu}\frac{\partial}{\partial x}H_y && (2.11)\\ & && (2.12)\end{aligned}$$

and similar to equation 2.3, the wavefunction $H_m(x)$ is given by

$$E_m(x) = \begin{cases} A\sin hx + B\cos hx & \text{if } |x| < d/2 \\ C\exp(-qx) & \text{if } x > d/2 \\ D\exp(qx) & \text{if } x < -d/2 \end{cases} \tag{2.13}$$

and again, h and q are related by

$$\tan(hd) = \frac{2h\bar{q}}{h^2 - \bar{q}^2} \tag{2.14}$$

where

$$\bar{q} = \frac{n_2^2}{n_1^2}q \tag{2.15}$$

2.1.3 Asymmetric slab waveguides

The symmetric slab waveguides described above can be considered a special case of asymmetric slab waveguides, which are much more prevalent in real-world applications. Now, the refractive index profile has three regions,

$$n(x) = \begin{cases} n_1 & \text{if} \quad 0 < x \\ n_2 & \text{if} \quad -t < x < 0 \\ n_3 & \text{if} \quad x < -t \end{cases} \tag{2.16}$$

Traditionally, sensors are designed such that the substrate refractive index is higher than that of the superstrate, i.e., $n_3 > n_1$. In terms of fabrication, this may be more readily achieved, as few suitable materials have a refractive index lower than that of water. However, the opposite case has also been demonstrated, and is referred to as a reverse symmetry waveguide [31]. A main advantage of such a design is the arbitrarily long superstrate penetration depth, which for certain applications (e.g., sensing of thick cell layers) is desirable [32].

To avoid non-physical steps in the wavefunctions, E_y must be continuous at both interfaces, i.e., $x = 0$ and $x = -t$. This is fulfilled using

$$E_m = \begin{cases} C\exp(-qx) & \text{if} \quad 0 \le \quad x \\ C\left(\cos(hx) - \frac{q}{h}\sin(hx)\right) & \text{if} \quad -t \le \quad x \le 0 \\ C\left(\cos(ht) - \frac{q}{h}\sin(ht)\right)\exp\left(p(x+t)\right) & \text{if} \qquad\quad x \le -t \end{cases} \tag{2.17}$$

where C is a constant, h and q are given by equations 2.4 and 2.5, respectively, and p is

$$p = \sqrt{\beta^2 - \left(\frac{n_3\omega}{c}\right)^2} \tag{2.18}$$

Likewise, H_z must also be continuous at both interfaces. It is given by

$$H_z = \frac{i}{\omega\mu}\frac{\partial E_y}{\partial x} \tag{2.19}$$

and so the x-derivative of E_y must also be continuous at both interfaces, leading to

$$h\sin(ht) - q\cos(ht) = p\left(\cos(ht) + \frac{q}{h}\sin(ht)\right) \Rightarrow \tag{2.20}$$

$$\tan(ht) = \frac{p+q}{h(1 - pq/h^2)} \tag{2.21}$$

This is the mode condition which the propagation constant must satisfy in order for a mode to be guided.

Similarly, for TM modes,

$$H_y(x,z,t) = H_m(x)\exp\left(i(\omega t - \beta z)\right) \tag{2.22}$$

where $H_m(x)$ is

$$H_m(x) = \begin{cases} -C\left(\frac{h}{\bar{q}}\cos(ht) + \sin(ht)\right)\exp\left(p(x+t)\right) & \text{if} \qquad\quad x \le -t \\ C\left(-\frac{h}{\bar{q}}\cos(hx) + \sin(hx)\right) & \text{if} \quad -t \le \quad x \le 0 \\ -\frac{h}{\bar{q}}C\exp(-qx) & \text{if} \quad 0 \le \quad x \end{cases} \tag{2.23}$$

Continuity leads to

$$\tan(ht) = \frac{h(\bar{p}+\bar{q})}{(h^2 - \bar{p}\bar{q})} \tag{2.24}$$

where

$$\bar{p} \equiv \frac{n_2^2}{n_3^2} p \tag{2.25}$$

The guided mode will propagate in the core layer, but in-plane coupling of light into a very thin slab waveguide is difficult and inconvenient. By nanostructuring a part of the waveguide, light can conveniently be coupled in by out-of-plane illumination.

2.1.4 Nanostructured waveguides

When a structure is periodic, i.e., it has translational symmetry, the permittivity tensor ϵ and refractive index n at one location must be the same as the value translated by a period Λ

$$\epsilon(z) = \epsilon(z + \Lambda) \tag{2.26}$$

$$n(z) = n(z + \Lambda) \tag{2.27}$$

Whereas the mode conditions (equations 2.21 and 2.24 for TE- and TM-mode, respectively) describe the propagation constant of allowed modes within the waveguide, the presence of a grating further imposes a phase matching condition [52] on the allowed propagation constants:

$$\beta = \frac{2\pi}{\Lambda} + k_0 n_1 \sin\theta \tag{2.28}$$

By combination of the mode condition and the phase matching condition, the resonance wavelength can be predicted semi-analytically, as shown by Hermannsson et al. [52]. By investigating the resonance wavelength shift in response to changing superstrate, the device sensitivity can furthermore be determined. When the waveguide supports multiple modes, multiple solutions are found, and so then model also applies in those cases.

The penetration depth is defined as the distance at which the mode amplitude has reduced to 1/e (~37%), e.g.,

$$H(\hat{e})/H(0) = 1/e \Rightarrow \tag{2.29}$$

$$\hat{e} = 1/q = 1/\sqrt{\beta^2 - \left(\frac{n_1\omega}{c}\right)^2} \tag{2.30}$$

The penetration depth can thus be designed for a given penetration depth, although a reverse symmetry waveguide is required for the deepest penetration depths.

2.1.5 Intra-cavity interference

Standing waves can also occur within larger cavities, and can often be detrimental to sensor-embedded microfluidic channels. This is known as Fabry-Pérot interference, and it occurs when a shallow channel is bounded by a reflective floor and ceiling. At normal incidence, the distance between interference fringes, the free spectral range (FSR), is given by [53]

$$\Delta\lambda = \frac{\lambda^2}{2nh} \tag{2.31}$$

where λ is the light wavelength and n is the refractive index in the cavity of height h. The interference is most disturbing when the FSR is similar to the resonance line width, and it can be tuned by modifying h. When the period is smaller than the detector resolution, it is not detected at all, and when it is much larger than the resonance linewidth, it merely contributes to the background.

2.2 Microfluidics

As the name implies, microfluidics deals with fluids on the micrometer scale. Because of how the governing laws scale, effects that are negligible on our everyday (macro-) scale can become extraordinarily important on the micro-scale. Likewise, effects that are essential on our macro-scale (such as gravity) can become unimportant on the micro-scale. Fascinating and non-intuitive phenomena in microfluidics enable applications that would not be possible on larger scales.

2.2.1 Pressure-driven flow

Microfluidics flow is governed by the Navier-Stokes equation, which for incompressible fluids (such as water) is given by

$$\rho\left(\frac{\partial \boldsymbol{v}}{\partial t} + (\boldsymbol{v}\cdot\nabla)\boldsymbol{v}\right) = -\nabla p + \eta\nabla^2\boldsymbol{v} + \boldsymbol{f} \tag{2.32}$$

where ρ is density, $\boldsymbol{v}$ is the velocity field, t is time, p is pressure, η is viscosity and $\boldsymbol{f}$ is external forces. The lefthand-side represents the sum of intertial forces, and on the righthand-side, the terms represent pressure forces, viscous forces, and external forces, respectively. This central equation allows numerical simulations of fluid flow, in conjunction with the continuity equation,

$$\frac{\partial \rho}{\partial t} + \nabla\cdot(\rho\boldsymbol{v}) = 0 \tag{2.33}$$

For a parallel plate geometry, illustrated schematically in figure 2.2, the Navier-Stokes equation has an analytical solution. The first term on the left-hand side of equation 2.32 vanishes due to the assumption of steady flow (velocity constant over time) characteristic of

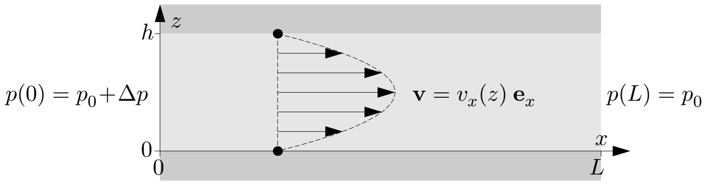

Figure 2.2. Parallel plate microchannel. The channel is much wider (in the y-dimension) than the channel height h. The velocity field has a parabolic profile. From ref. [51].

Hagen-Poiseuille flow. Under the assumption of uni-directional flow, the second term on the left likewise vanishes, simplifying the equation to

$$\frac{\partial^2 v_x(z)}{\partial z^2} = -\frac{\Delta p}{\eta L} \tag{2.34}$$

Due to no-slip boundary conditions, $v_x(0) = v_x(h) = 0$, and the solution is the parabolic flow profile

$$v_x(z) = \frac{\Delta p}{2\eta L}(h - z)z \tag{2.35}$$

For pressure-driven flow, the relationship between pressure gradient Δp, flow rate Q and hydraulic resistance R_{hyd} is given by the Hagen-Poiseuille law [51]

$$\Delta p = QR_{\text{hyd}} = 12\eta LQ/(h^3 w) \tag{2.36}$$

where L is the length of the wide and shallow channel ($h \ll w$). The hydraulic resistance R_{hyd} depends on the shape of the channel, as indicated by table 2.1.

The new opportunities afforded by microfluidics are made possible by the ability to finely control fluid flow. With careful design of system architectures and operation at sufficiently low flow rates, chaotic and turbulent behavior of fluids can be completely suppressed. In the absence of turbulence, the flow is said to be laminar, and molecules are neatly transported by convection. The only way for a molecule to move away from its designated streamline is through diffusion. This is extensively exploited in a microfluidic H-filter. The degree of laminarity in a flow of viscosity η is described by Reynold's number,

$$\text{Re} = \frac{\rho v L}{\eta} \tag{2.37}$$

where L is the characteristic length. When Reynold's number is small, e.g., Re $\ll 1$, the flow is laminar. When it is large, the flow is turbulent. However, no hard cutoff exists where a fluid flow suddenly transitions from being laminar to being turbulent. As we shall see next, diffusion is a very fast process on small length scales, and a very slow process on large length scales. In the latter case, inducing turbulence may be the only way to ensure mixing in a microfluidic device.

Table 2.1. Hydraulic resistance in various channel geometries. From ref. [51].

shape		R_{hyd} expression	R_{hyd} $[10^{11}\ \frac{\text{Pa s}}{\text{m}^3}]$
circle	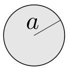	$\frac{8}{\pi}\,\eta L\,\frac{1}{a^4}$	0.25
ellipse	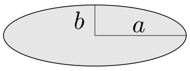	$\frac{4}{\pi}\,\eta L\,\frac{1+(b/a)^2}{(b/a)^3}\,\frac{1}{a^4}$	3.93
triangle	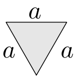	$\frac{320}{\sqrt{3}}\,\eta L\,\frac{1}{a^4}$	18.48
two plates	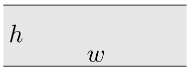	$12\,\eta L\,\frac{1}{h^3 w}$	0.40
rectangle	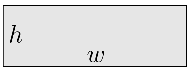	$\frac{12\,\eta L}{1-0.63(h/w)}\,\frac{1}{h^3 w}$	0.51
square	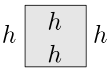	$\frac{12\,\eta L}{1-0.917\times 0.63}\,\frac{1}{h^4}$	2.84

2.2.2 Diffusion

Einsteins defined the diffusion length $\bar{x}$, the root-mean-square (RMS) extent of transport, as

$$\bar{x} = \sqrt{2Dt} \tag{2.38}$$

where D is the diffusion coefficient.

Stokes defined the frictional force F_d, which would become known as the Stokes' drag, as

$$F_d = 6\pi\eta R v \tag{2.39}$$

where R is the radius of a spherical object moving through a liquid of dynamic viscosity η and v is the flow velocity relative to the sphere.

The Einstein-Smoluchowski relation relates the diffusion coefficient of a particle to its "mobility" μ_m as

$$D = \mu_m k_B T \tag{2.40}$$

where k_B is Boltzmann's constant and T is temperature. Mobility is the inverse of Stokes' drag, giving rise to the Stokes-Einstein relation

$$D = \frac{k_B T}{6\pi\eta r_{\text{hyd}}} \tag{2.41}$$

where r_{hyd} is the hydrodynamic radius.

Consider a random walk in one dimension, with length scale Δx, time scale Δt, and $N(x,t)$ the number of particles at position x at time t. Each time step, half of particles move left, and the other half moves right. Because of this, the net movement to the right is

$$-\frac{1}{2}\left(N(x+\Delta x,t)-N(x,t)\right) \tag{2.42}$$

The flux J is the net movement of particles through an area a, normal to the direction of movement during a time interval Δt:

$$J=-\frac{1}{2}\left(\frac{N(x+\Delta x,t)}{a\Delta t}-\frac{N(x,t)}{a\Delta t}\right)\Leftrightarrow \tag{2.43}$$

$$J=-\frac{(\Delta x)^2}{2\Delta t}\left(\frac{N(x+\Delta x,t)}{a(\Delta x)^2}-\frac{N(x,t)}{a(\Delta x)^2}\right) \tag{2.44}$$

The definitions of concentration (ϕ, particles per unit volume) and 1-dimensional diffusion coefficient (D) are:

$$\phi(x,t)=\frac{N(x,t)}{a\Delta x} \qquad \text{and} \qquad D=\frac{(\Delta x)^2}{2\Delta t} \tag{2.45}$$

Inserting into 2.44 gives

$$J=-D\left(\frac{\phi(x+\Delta x,t)}{\Delta x}-\frac{\phi(x,t)}{\Delta x}\right) \tag{2.46}$$

When Δx is infinitesimal, this equation becomes Fick's first law

$$J=-D\frac{\partial\phi}{\partial x} \tag{2.47}$$

According to mass conservation,

$$\frac{\partial\phi}{\partial t}+\frac{\partial}{\partial x}J=0 \tag{2.48}$$

Inserting Fick's first law (equation 2.47) gives

$$\frac{\partial\phi}{\partial t}-\frac{\partial}{\partial x}\left(D\frac{\partial}{\partial x}\phi\right)=0 \tag{2.49}$$

Assuming D to be constant allows the following reordering, known as Fick's second law

$$\frac{\partial\phi}{\partial t}=D\frac{\partial^2\phi}{\partial x^2} \tag{2.50}$$

A microfluidic H-filter, illustrated in figure 2.3, exploits the propensity of small molecules to diffuse much faster than larger particles, allowing a size-based separation of the contents of a fluid stream. When monitoring processes in the interdiffusion zone, rather than performing separation of compounds, the device is sometimes referred to as a T-sensor. Although

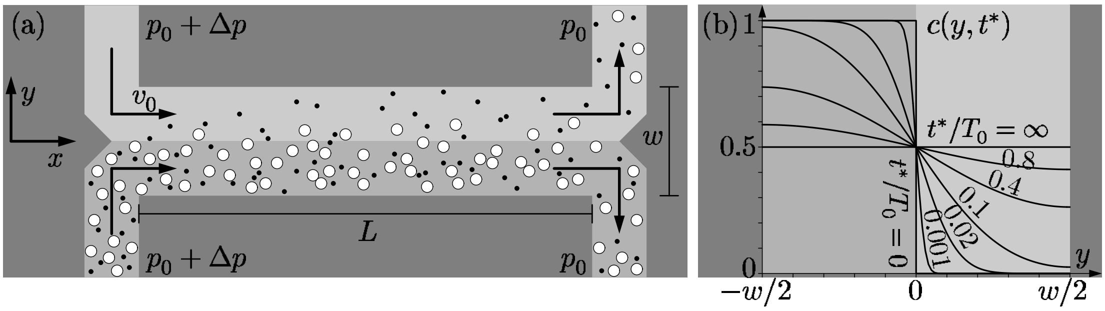

Figure 2.3. Working principle of a microfluidic H-filter illustrated schematically. Due to their much larger diffusion coefficient, smaller molecules transport from one stream into the other, to a much greater extent than larger molecules, allowing size-based separation. From ref. [51].

monitoring is also the focus in this work, to avoid confusion with the optical sensor component, the term H-filter will be used here. In one dimension, Fick's second law has the solution

$$\phi(y) = \phi_0 \mathrm{erfc}\left(\frac{y}{2\sqrt{Dt}}\right) \tag{2.51}$$

where ϕ_0 is the initial concentration. Thus, by monitoring the diffusion profile $\phi(y)$, equation 2.51 can be fitted to reveal diffusion length and, if t can be accurately estimated, also diffusion coefficient.

2.2.3 Diffusion-convection coupling

The diffusion-convection equation is given by

$$\frac{\partial c}{\partial t} = \overbrace{\nabla \cdot (D \nabla c)}^{\text{Diffusion}} - \overbrace{\nabla \cdot (\boldsymbol{v} c)}^{\text{Convection}} + \overbrace{R}^{\text{Source}} \tag{2.52}$$

$$\tag{2.53}$$

In the case of the H-filter, there are no sources (or sinks), so $R = 0$. The diffusion coefficient is assumed to be a constant, so $\nabla \cdot (D\nabla c) = D\nabla^2 c$. Assuming incompressible flow, we have zero divergence, $\nabla \cdot (\boldsymbol{v} c) = \boldsymbol{v} \cdot \nabla c$. Additionally, we are mainly interested in situations where steady state have been achieved, i.e., $\frac{\partial c}{\partial t} = 0$, and so the diffusion-convection equation simplifies to

$$\boldsymbol{v} \cdot \nabla c = D \nabla^2 c \tag{2.54}$$

Under laminar flow conditions, convection only occurs in the axial direction. Assuming axial diffusion can be neglected, we have

$$0 = \boldsymbol{v} \cdot \frac{\partial c}{\partial x} - D\frac{\partial^2 c}{\partial y^2} - D\frac{\partial^2 c}{\partial z^2} \tag{2.55}$$

Axial diffusion can be neglected when the rate of advective transport is much greater than the rate of diffusive transport, a relation quantified by the Péclet number

$$Pe = \bar{v}L/D \tag{2.56}$$

where L is the characteristic length and $\bar{v}$ is the average flow velocity. Thus, when Pe is small, the system is dominated by diffusion, and when it is large, advection dominates.

Chapter 3

Method

Sensor technology development has been accelerated by breakthroughs in microfabrication, driven mainly by the constant need for faster central processing units (CPUs) [34]. Likewise, microfluidics are typically produced at least partially using cleanroom fabrication techniques, such as photolithography and reactive ion etching (RIE). This chapter presents the techniques used for fabrication and characterization of PCS sensors, microfluidics systems, and devices integrating both.

3.1 Sensor microfabrication

Silicon masters, fabricated by electron beam lithography, were used for nanoimprint lithography. The masters contained grating areas of $2\times2\,\mathrm{mm}^2$ in a 4×4 pattern, spaced 9 mm apart. Each square contained a linear grating of period $\Lambda = 368\,\mathrm{nm}$, height $h = 100\,\mathrm{nm}$, and duty cycle 50%. To facilitate stamp release after imprinting, the stamp had a perfluorodecyltrichlorosilane (FDTS)-coating applied by molecular vapor deposition (MVD).

Substrates were defined by CO_2-laser cutting slabs of 2 mm thick poly(methyl methacrylate) (PMMA) to a diameter of 100 mm, which were then cleaned by sonication in Triton X-100, followed by rinsing, spin-drying and plasma ashing.

PCS sensors were microfabricated by placing a droplet of low-refractive index polymer Efiron PC409-AP (Luvantix, Korea), diluted to 85% w/w in 2-butanone (Sigma), between stamp and PMMA-substrate. After allowing the polymer to spread by gravity and capillary forces, it was cured using a 1000 W UV lamp for 16 min. The two parts could then be separated using a razor blade, leaving the substrate with a grating and the stamp ready for reuse.

3.1.1 Waveguide core

For TM-mode sensors, a TiO_2 waveguide core layer of nominal thickness 80 nm was deposited by ion-beam sputter deposition (IBSD) (IonFab 300, Oxford Instruments, Abingdon, England). Prior to loading a sample, an approx. $1\times1\,\mathrm{cm}^2$ silicon wafer fragment was attached using polyimide tape. This opaque substrate allowed the film thickness to be subsequently measured by variable angle spectroscopic ellipsometry (VASE) (M2000V, J.A. Woollam Co., Inc., Lincoln, NE, USA).

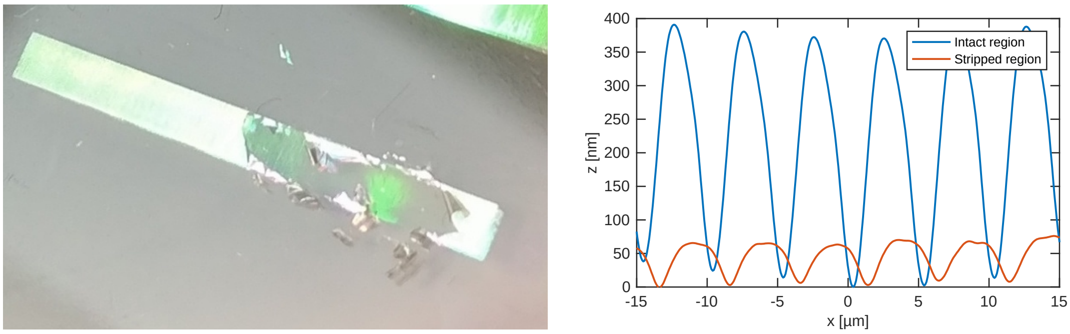

Figure 3.1. Persistent grating effect observed after removal of the nanostructured layer. a) Photograph of the stripped region. The green colors are due to diffraction, indicating the persistence of a grating, as supported by b) profilometer measurements of intact and stripped regions.

For wholly polymeric TE-mode devices, also the high-refractive index waveguide core layer was comprised of polymer. The experimental polymer HI01XP by micro resist technologies GmbH (Berlin, Germany) was chosen for this purpose, as was detailed in ref. [26]. This polymer is a glass-like, UV-curable, organic-inorganic hybrid polymer, which has a refractive index of $n_D = 1.59$, due to the incorporation of embedded ZrO_2 nanoparticles. To reduce its viscosity and allow spin coating, it was diluted to 15% w/w in the thinner ma-T 1050 (micro resist technologies), and spin coated at 3000 rpm for 1 min. HI01XP is known to form an inhibition layer upon exposure to UV light in the presence of oxygen [26], and so the 5-minute curing exposure was performed in a nitrogen atmosphere.

When surface adhesion is insufficient, the low-refractive index material can come loose when exposed to mechanical stress, e.g., pressurized air, as illustrated in figure 3.1. Interestingly, a grating color effect is still observed in the absence of the nanostructured layer, which was verified by profilometry. If part of the grating would remain on the substrate after stripping, this might enable NIL with zero residual layer thickness (RLT), which is challenging to achieve by other means. However, after scanning electron microscope (SEM) inspection (figure 3.2), it would appear that the NIL also imposes a surface relief in the PMMA substrate, i.e., not only in the low-refractive index layer, giving rise to a double-grating in the substrate layer.

3.2 Microfluidics integration

3.2.1 Rapid prototyping

For rapid prototyping of microfluidics systems with relatively large dimensions, adhesion bonding and laser cutting can be employed, as described by Patko et al. [54]. Microfluidic design was performed in Corel Draw X3. For the simplest designs, channels and inlets could simply be designed by fusing circles and rectangles. Channels were then defined by adhesion bonding, where the adhesion layer was defined using a CO_2-laser (Epilog Mini 18, 30 W,

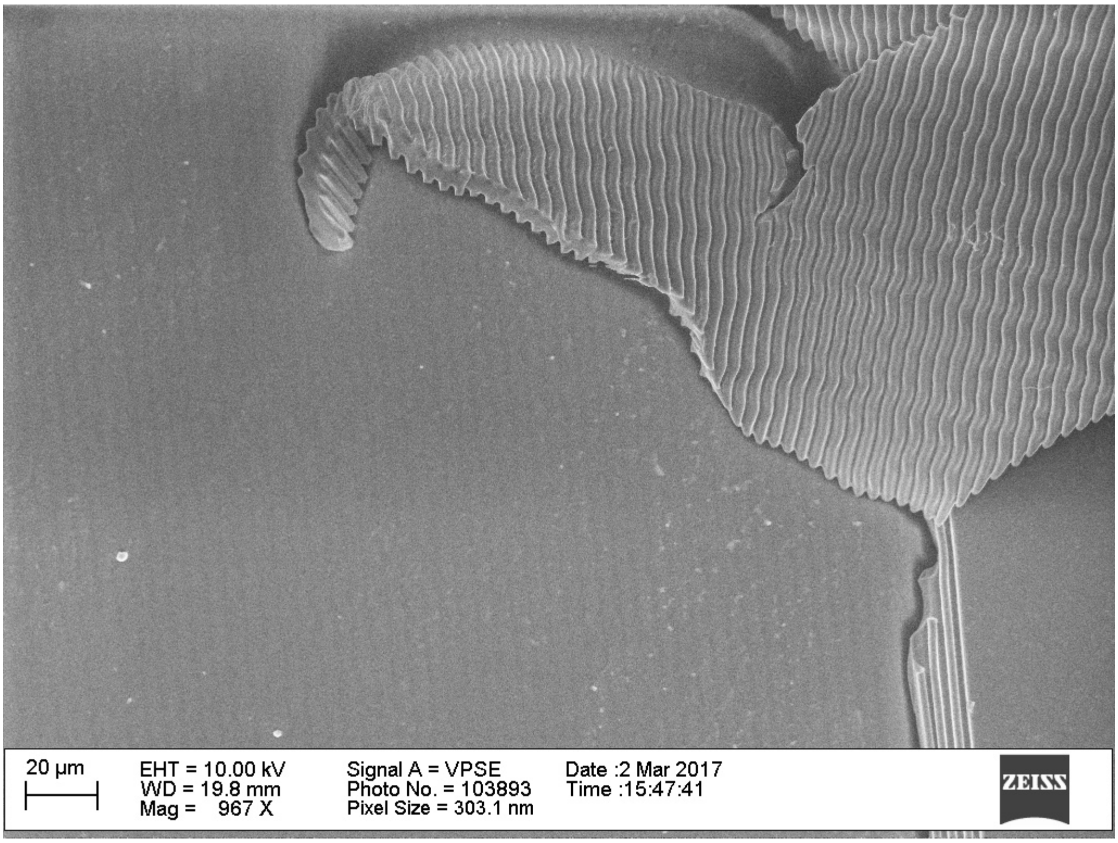

Figure 3.2. Scanning electron micrograph of foil peeling away from the substrate upon mechanical stress. Interestingly, the substrate itself also appears to have an undulating surface shape.

Epilog, Golden, CO, USA). The adhesion layer was prepared by placing a layer of yellow tape on a slab of PMMA, from which the subsequent layers would release. Then, a layer of cleanroom blue-tape was placed, which is glue-free and forms a reversible bond. On top of this, a high-tack double-adhesive tape layer was placed. The entire stack was compressed using a roller to push out air. By laser-cutting at maximum speed and power, all layers were cut through. The blue-tape could then be separated from the yellow tape, along with the layer of double-adhesive on top, and carefully aligned on the sensor slab with the sensor in the correct orientation and position within the channel system. Using blue-tape as a carrier layer allowed subsequent removal of the microfluidic system and rinsing of the wafer for reuse. On top of the double-adhesive layer, once it had been placed on the wafer and its lining layer removed, a piece of laser-cut PMMA, injection molded cyclic oleofin copolymer (COC) or cast polydimethylsiloxane (PDMS) was placed to form the channel “roof” and provide fluid interfacing. In the case of COC, fluid inlets were pre-defined by the mold, for PMMA, they were laser cut and for PDMS, access holes were made using a biopsy punch. The liquid was driven either using 100 µL Hamilton glass syringes (Sigma-Aldrich, St. Louis, MO, USA) and a syringe pump (Model 11 Plus, Harvard Apparatus, Holliston, MA, USA), or using an electronic microfluidic flow control system (MFCS) (Flex, Fluigent, Inc., Villejuif, France).

Using laser cutting and adhesion bonding, proof-of-concept microfluidic systems could be prototyped within minutes, and due to the reversible bonding, could be removed after use. This is particularly useful for costly substrates, such as titania sensors. However, the channel dimensions were limited by the CO_2-laser resolution, as well as the tape layer thicknesses. It was estimated that channels of width and height down to ~100 µm could be produced by this method.

A main argument for using PMMA rather than glass wafers for support, apart from cost considerations, was the option for increased thickness. With the refractive index of glass wafers and typical thickness on the order of 0.5 mm, the interference was highly disturbing. This could be reduced by application of index-matching oil between the glass wafer and a thick slab underneath, which works well for a “bare” sensor. However, the bonding of microfluidics structures can impose strain on the wafer, imparting on it a slightly concave shape, enough to make the index-oil flow towards the wafer perimeter due to capillary forces. For this reason, the Fabry-Pérot interference could not be alleviated using index-matching oil, when a microfluidics system was implemented. Instead, the sensors were fabricated directly on a thick PMMA substrate. An even thicker PMMA slab would in principle have been preferable as it could reduced the interference period even further, but substrates exceeding 2 mm thickness were incompatible with many cleanroom processes.

3.2.2 Ultrasonic bonding

In order to produce channels of height less than the adhesive thickness, a number of approaches were attempted. Traditionally, our group has focused on ultraviolet (UV)-assisted thermal bonding of injection molded COC chips [55], however, as the high temperature (≈140 °C) was suspected to damage the gratings, and because thermal bonding of two dissimilar materials is known to be challenging, this approach was abandoned.

Instead, ultrasonic welding was investigated for bonding of microfluidic chips, such as

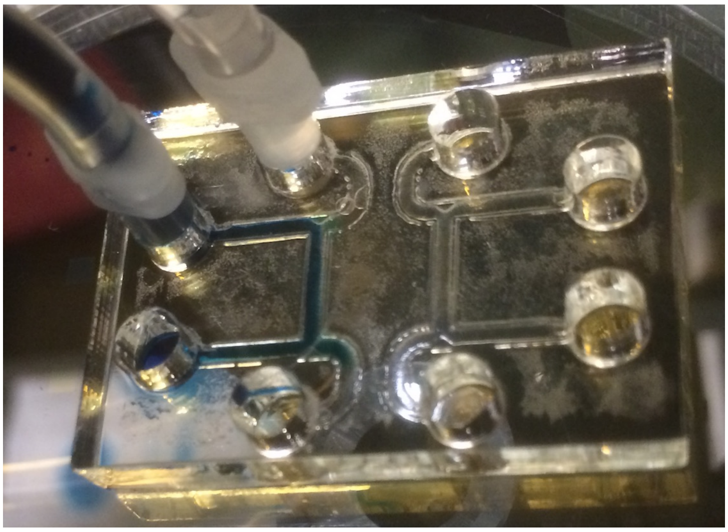

Figure 3.3. Ultrasonically bonded H-filter prototype. Water with blue food coloring flows from the left inlet, and pure water flows from the right inlet. The channels are water tight, but the optical quality suffers when devices are produced by laser ablation. Channels are 2 mm wide.

the one shown in figure 3.3. This technique is widespread in industrial production settings, but has been largely overlooked by the microfluidics community as an option for bonding [56]. The technique works by inducing ultrasonic vibrations in a polymer piece while pressing it against another piece. Friction causes the polymer to melt at the points of contact, forming a seal, as schematically illustrated in figure 3.4. In order to acheive a water tight seal, it is imperative that energy directors be appropriately designed, as they determine the points of contact. Although it is possible to bond dissimilar materials in this manner, provided that they have comparable glass transition temperatures, the technique works best for identical materials. Thus, in order for a microfluidic chip part to bond to a sensor substrate, the energy directors have to first penetrate the material layers constituting the sensor. To this end, energy directors were designed to protrude to a distance exceeded the cumulative sensor thickness, and fabricated by laser ablation or injection molding.

For laser ablation, performance was compared using extruded and cast PMMA, as the properties of these two subtly different materials are known to differ significantly in response to laser ablation. For one, extruded PMMA remains clear upon laser engraving, whereas cast PMMA becomes opaque. Of importance to the effort of creating energy directors, the weld lines forming at the perimeter of a laser ablation line also differs greatly between the two substrates. Using laser ablation, a channel was produced by raster engraving, whereas energy directors were defined by vector engraving. These device could be produced leak-free (albeit with a low yield), but the laser engraving was detrimental to the optical quality of the channels. In addition, because the rough channel ceiling might act like a herringbone mixer, potentially causing lateral convection, this method was not pursued further. Instead, a shim for injection-molding was attempted micro-milled, but achieving channel depths of 10 μm is quite challenging by this method. For such shallow channels, photolithography is more suitable.

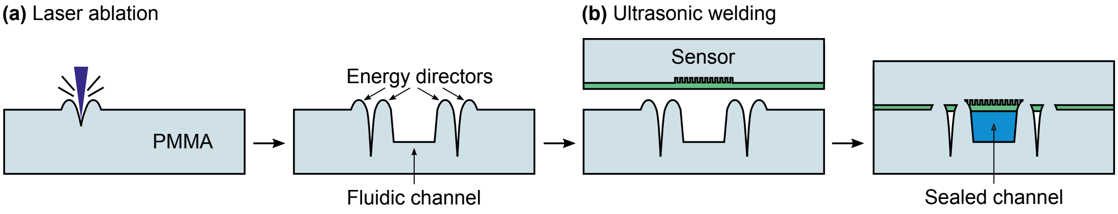

Figure 3.4. Schematic illustration of ultrasonic bonding process. a) First, a substrate is laser ablated to define channels and energy directors. b) Upon ultrasonic bonding, the energy directors penetrate the sensor materials to form a seal with the underlying substrate.

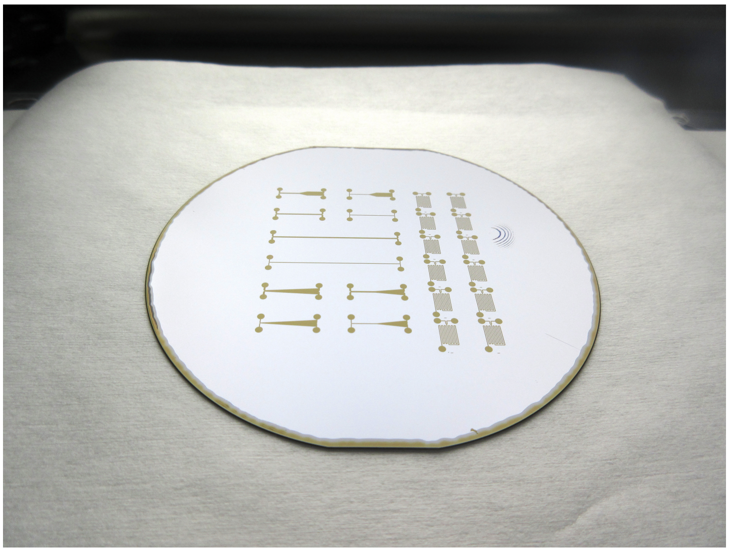

Figure 3.5. Photograph of H-filter mold, as defined by photo lithography. Multiple design variations are included.

3.2.3 Photolithography & casting

To define silicon stamps for casting of PDMS, UV photolithography was employed. A 9 µm-film of the positive resist AZ-4562 was deposited by spincoating, and exposed through a custom chromium mask, designed in L-Edit (Tanner Research Inc., Monrovia, CA, USA) and produced by Delta Mask B.V. (Enschede, The Netherlands). After development in 2.38% tetramethylammonium hydroxide (TMAH) using a Gamma 2M robot (Süss MicroTec, Garching bei München, Germany), the stamp was FDTS-coated to facilitate demolding.

Microfluidic structures were cast in PDMS (Sylgard 184, Dow Corning, Midland, MI, USA) by mixing the monomer with precursor in a 10:1 ratio, degassing, then pouring over the silicon stamp and curing for 2 h at 80 °C. Individual chips were then excised using a scalpel, and inlet holes were defined using a 0.5 mm biopsy punch (World Precision Instruments Ltd., Sarasota, FL, USA). It is crucial that the biopsy punches remain very sharp in order to avoid cracking around the inlets, which will cause them to leak. For bonding, the PDMS-chip and all-polymer wafer were exposed to an oxygen plasma for 60 s at 150 W. Working swiftly, the

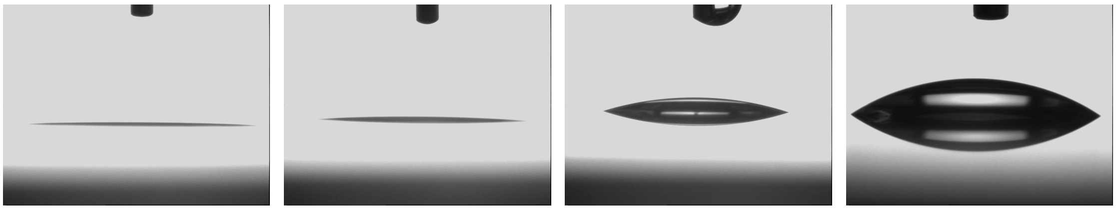

Figure 3.6. Recovery of contact angle after plasma ashing of high-index polymer HI01XP. Contact angle is measured to be a) 1.8° after 13 min, b) 2.7° after 19 h, c) 17.2° after 42 h, and d) 45.7° after 360 h.

PDMS part was aligned to the wafer, assisted by in-plane guided light, making the sensors “shine” by coupling light out out-of-plane. After contact, an irreversible bond was established covalently.

In order to facilitate bonding, the surface was plasma ashed. As expected, this was found to effectively decrease the contact angle, as shown in figure 3.6a. The surface remains relatively hydrophilic for ~1 day (figure 3.6b), after which the surface starts to recover its hydrophobic nature (figure 3.6c). This is of consequence to microfluidics applications, as the surface energy of the device then changes over time following fabrication. It is unknown whether the hydrophobic recovery is halted by, e.g., storage in water. However, for applications such as water-in-oil emulsions, where hydrophobic channels are desirable, it might be an acceptable production requirement that the device be left in air for a week prior to shipping.

Summary

In this chapter, methods have been presented for fabricating titania-based (TM-mode) as well as wholly polymeric (TE-mode) sensors. Multiple methods for subsequent integration of said sensors into microfluidics systems have furthermore been discussed: Laser ablation and adhesion bonding has the fastest turnaround, with minutes between idea and its realization. However, the technique provides a minimum spatial dimension of approx. 100 µm, which may be too crude for many applications. As an alternative, injection molding and ultrasonic bonding can be employed. With injection molding, a large number of identical chips can be produced quickly, cheaply, and with high performance. Like injection molding, ultrasonic bonding is favored by industry, as it is amenable to mass-production. However, for sensor integration, energy directors must penetrate several thinfilms before bonding is achieved. A substantial effort was needed to produce tight chips as a proof-of-concept, but the yield was generally low. The spatial dimensions are in part limited by the method used to produce the molding shim. To this end, micro-milling was employed, but lithography, etching and electroplating would also have been an option. A third approach was to produce a mold using UV photolithography, and casting the microfluidics part from PDMS. These chips could readily be plasma-bonded to polymeric sensors, and were found to work best as H-filters, given their shallow channels on the order of 10 µm.

Chapter 4

Simulation

RESEARCH into light-matter interactions on the nanometer-scale has enabled the development of the rigorous coupled-wave analysis (RCWA) and finite-difference time-domain (FDTD) simulation methods. These are powerful work horses of many photonics endeavors, and routinely form the basis of design and optimization prior to fabrication. PCS sensors are defined by several parameters as listed in table 4.1, and sensor optimization thus becomes a many-dimensional optimization problem. This is especially true for multi-periodic and two-dimensional gratings, where the number of parametric permutations is virtually infinite. As biological evolution can be considered the ultimate many-dimensional optimization challenge, nature is often looked to for inspiration. Genetic algorithms [57] define a fitness expression, such that more desirable solutions (e.g., higher sensitivity) are more likely to “survive” between iterations. In particle swarm optimization (PSO) [58], parameter sets are iteratively chosen to be similar to the currently most desirable solution, causing other parameter sets to “flock” towards it. This ensures that similar parameter sets are investigated in order to find even better solutions, whereas the random component of the swarm “flight” reduces the risk of getting stuck at a local optimum. These methods are commonly used for design optimization [59, 60], however, as full numerical solutions of Maxwell’s equations are required [60], computation times can be very long. This chapter describes efforts to reduce the time required for simulations, with less *a priori* information required and without compromising resolution.

The concept of multiscale simulations can refer to simulations on the macro-scale, that depend on input from the micro-scale. In a broader sense, it is referred to here as simulations that need a high local resolution in small parts of a broad interval. Simulating the full interval at a sufficiently high resolution will be inhibitively time-consuming, but a coarse-grained simulation will not provide the necessary local resolution in the regions of interest, and may be insufficient to detect regions of interest at all. Figure 4.1 illustrates this central problem in simulating resonance spectra. When the point spacing is static, flat regions have a much higher resolution than necessary, which may yet be insufficient in the peak regions. Using the adaptive sampling algorithm developed here, the information emphasis is effectively reversed. This “needle-in-a-haystack” type of problem means that either sufficient *a priori* information must be obtained in order to reduce the length of the simulated interval (e.g., using the analytical model described in the next section, lest the majority of simulated points will reveal little new information.

Table 4.1. Parameters describing PCS sensors, along with typical values. Optimization simulations may be set up in order to arrive at a given set of result parameters, by varying the design parameters.

Parameter	Symbol	Example value
Design parameters		
Grating period	Λ	368 nm
Grating height	h_g	100 nm
Duty cycle	F_g	50 %
Core thickness	t_c	300 nm
Superstrate dispersion	$n_1(\lambda)$	1.33 RIU
Core dispersion	$n_2(\lambda)$	1.59 RIU
Substrate dispersion	$n_3(\lambda)$	1.40 RIU
Azimuthal angle	ϕ	0°
Polar angle	θ	0°
Result parameters		
Resonance wavelength	λ_r	550 nm
Resonance intensity	I_r	100 %
Line width	FWHM	0.5 nm
Quality-factor	Q	1100
Sensitivity	$d\lambda_r/dn$	30 nm/RIU
Noise	$\sigma(\lambda_r)$	1 pm
Limit of detection	LOD	1×10^{-5} RIU
Penetration depth	$\hat{e}$	138 nm

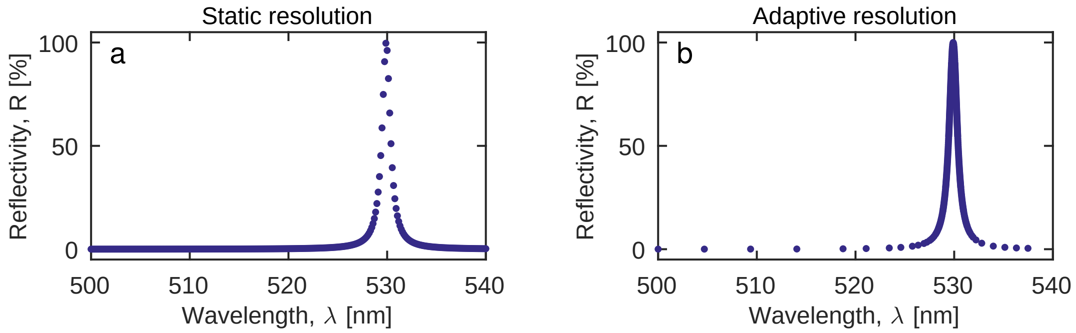

Figure 4.1. Simulated point density using a) static and b) dynamic methods. The former emphasizes the background whereas the latter emphasizes the peak region. From ref. [61].

The challenges of multiscale simulations are present in many fields. For example, Rouet-Leduc et al. proposed a solution for elastodynamic shock propagation simulations [62]. Here, results of atomistic molecular dynamics simulations at each spatial coordinate are used to determine subsequent optimum sampling points. They refer to this method as the heterogeneous multiscale method, and show that a stress field can be constructed at N grid points using only $\sim 50 \times N^{0.14}$ micro-scale simulations. Awile et al. similarly demonstrated a solution for simulating particle-particle interactions with adaptive resolution [63]. Particle-particle simulations are relevant not only to physical entities like atoms, but can also be used as abstractions for traffic flow and financial instruments. In priciple, all particles are affected by all other particles, but in practice, only those within a given cutoff radius have a significant influence. The authors present a method for efficiently determining which particle-particle interactions need simulating.

However, these approaches are not directly compatible with RCWA simulations, which often suffer from challenges similar to those of true multiscale systems, i.e., finding and sufficiently resolving narrowband spectral features in a broad spectrum. To address this challenge, in a manner that is designed for interfacing with many other simulation packages, the `asasim` algorithm was written, and submitted to Computer Physics Communications (appendix A).

4.1 Analytical model

As described in section 2.1.3, the equations governing resonance wavelength are intricately coupled. Thus, a wholly analytical solution does not exist. Instead, simulation methods such as FDTD and RCWA are commonly employed to predict sensor performance and characteristics. Such solutions represent tried and true software with a high degree of versatility. However, this often also comes at a high monetary cost. Therefore, in 2014, Hermannsson et al. demonstrated a semi-analytical approach [52] to predicting the GMR wavelength. Briefly, when the sensor grating properties (period and material dispersions) are known, the refractive indices can be calculated at an initial guess-wavelength. From these new refractive index values, another resonance wavelength value is calculated, which gives rise to slightly different material refractive indices. When the values converge, the resonance wavelength is considered found. This algorithm can be implemented much more simply than setting up a full RCWA simulation, in which narrow resonances can furthermore be difficult to detect in a broad interval. However, this elegant semi-analytical method is incapable of predicting line shapes and additional spectral features. RCWA provides this ability, as addressed in the following section.

4.2 Rigorous coupled-wave analysis

In this thesis, light-matter interactions were simulated using RCWA in GD-Calc, a MATLAB-package distributed by KJInnovation (Santa Clara, CA, USA). In the terminology of the GD-Calc simulation package, a model is first defined with each layer described as a “stratum”, and each of these strata contain “stripes”. The geometry is thereby set up as shown in figure

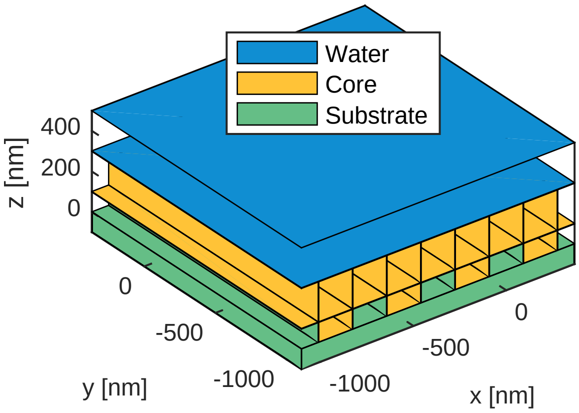

Figure 4.2. Model setup for RCWA simulation, as generated by GD-Calc using the provided parameters, e.g., a linear grating is simulated with a period of $\Lambda = 368$ nm.

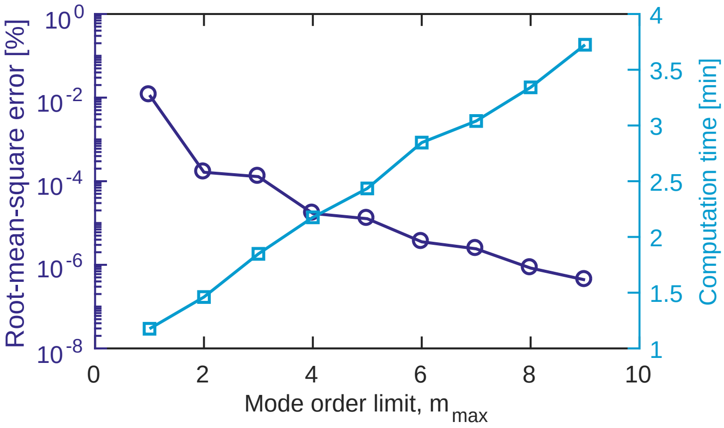

Figure 4.3. Influence of mode order truncation on RCWA simulations. Increasing the truncation limit improves precision at the cost of computation time.

4.2 by providing a period and duty cycle for the stripes, and thickness for the strata. Furthermore, the permittivities of the constituent materials must be provided. Dispersion data was recorded using VASE (J.A. Woollam, NE, USA). The simulation package then simulates the diffraction efficiencies of s- and p-polarized light at the given polar and azimuthal angle of incidence, taking into account a number of diffraction orders given by m_{max}.

Time of computation scales with the number of simulated diffraction orders, but at a certain limit, the increased precision of the simulation adds little to its conclusion. The diffraction order truncation limit m_{max} should thus be set appropriately. Setting the limit too low can introduce systematic errors, whereas an excessively high limit may improve accuracy unnoticably at the cost of increased time for computation. Figure 4.3 illustrates a standard RCWA simulation of a grating at order truncation limits ranging from 1 to 10. The RMS error

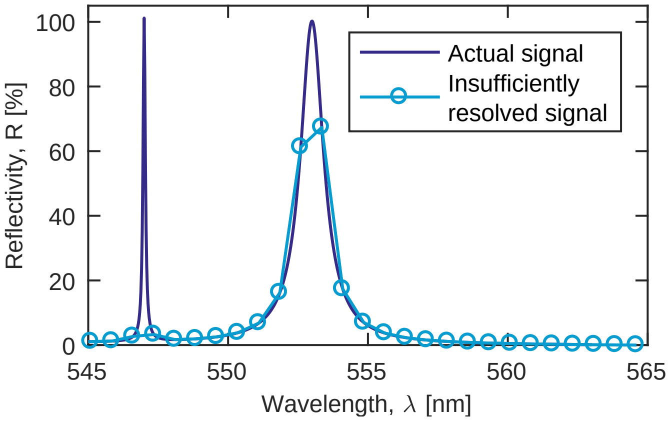

Figure 4.4. The detection problem of multiscale simulations. When resolution is insufficient, peaks risk being completely absent from the simulation. When the peak width is large enough, it will always cause a "bump" in the spectrum, no matter how the points happen to fall.

on the reflectivity, with a mode truncation limit of $m_{\text{max}} = m$ is calculated as

$$\text{RMSE}(m) = \sqrt{\frac{\sum_{i=1}^{n}(R_{i,m} - R_{i,10})}{n}} \tag{4.1}$$

where i is the index of the simulated wavelength, n is the total number of simulated wavelengths, and R is the simulated reflectivity. Each point is thus compared to $R_{i,10}$, i.e., the reflectivity at a given wavelength simulated with a mode order truncation limit of $m_{\text{max}} = 10$. As figure 4.3 illustrates, the computation time increases linearly with the maximum order, whereas the error decreases roughly exponentially. For such a simple geometry, the error is already very small when just a few orders are taken into account.

4.3 Optimal peak detection

Apart from adjusting the number of diffraction orders to simulate, in practice, the only other knob for the user to turn is which wavelengths to simulate. This can most simply be done by shortening the wavelength interval, requiring *a priori* information about the resonance wavelength, or by reducing the resolution. Being a multiscale problem, broadband information is desired (at low resolution) simultaneously with narrowband information (at high resolution). This can be achieved by first performing a simulation at low resolution in order to detection subregions for refinement, then refining these regions of interest to the desired resolution. However, the initial resolution must be carefully chosen in order to detect all peaks of interest. Figure 4.4 illustrates this problem - when resolution is too low, points may fall on either side of a narrow peak, which will then be misleadingly absent from the simulation. The question therefore is, what initial resolution will ensure that all spectral features of a minimum half-width are always detected, so that they may be subsequently refined?

A resonant reflection is typically well-described by a lorentzian [64],

$$y(x) = \frac{1}{\pi\gamma\left[1 + \left(\frac{x-x_0}{\gamma}\right)^2\right]} \tag{4.2}$$

where γ is the scale parameter (effectively half-width at half-maximum) and x_0 is the location parameter. In the context of reflectivity R, taking on values between 0 and 100%, it can be expressed as a function of wavelength λ and half-width γ, centered at an arbitrary wavelength, i.e., $\lambda_0 = 0$,

$$R(\lambda) = \frac{1}{1 + \frac{\lambda^2}{\gamma^2}} \tag{4.3}$$

$$\lambda = \sqrt{\gamma^2\left(\frac{1}{R} - 1\right)} \tag{4.4}$$

It is a fortuitous property of lorentzian curves that they tend to have “fat tails”, i.e., the perturbation from the peak extends further than would be the case for, e.g., a gaussian. While spectral resolution is traditionally defined on the independent axis (λ), with adaptive sampling, it is possible to define a desired resolution in terms of R.

Because of the subdivisioning-scheme employed, whenever a peak is detected, it is certain to come out fully resolved. Detection in this context entails that the perturbation from a peak causes two neighboring points, spaced apart by $\Delta\lambda$ on the first axis, to have a sufficient difference on the second axis, $\Delta R > \Delta R_{\max}$. The narrowest peak of half-width γ that is certain to be detected is then a peak that is so narrow, that its perturbation only just causes ΔR between any two neighboring points to exceed $\Delta R_{\max}$, even when the peak is placed right between those two neighboring points. In this case, ΔR is zero between them, so for detection, the difference to the *next* neighbor must instead satisfy $\Delta R > \Delta R_{\max}$. If the distance from the peak center to the first symmetrically placed neighbor is $\lambda_1 = \Delta\lambda/2$, then the distance to *its* next neighbor must be $3\lambda_1$:

$$\Delta R = R_1 - R_2 \tag{4.5}$$

$$= \frac{1}{1 + \frac{\lambda_1^2}{\gamma^2}} - \frac{1}{1 + \frac{(3\lambda_1)^2}{\gamma^2}} \tag{4.6}$$

which does not have a simple solution for the optimal point spacing $\Delta\lambda = 2\lambda_1$. However, it can be isolated as

$$\Delta\lambda = \pm\left(\frac{2}{3}\sqrt{\frac{\gamma^2(4-5\Delta R) \pm 2\sqrt{2}\sqrt{\gamma^4(2\Delta R^2 - 5\Delta R + 2)}}{\Delta R}}\right) \tag{4.7}$$

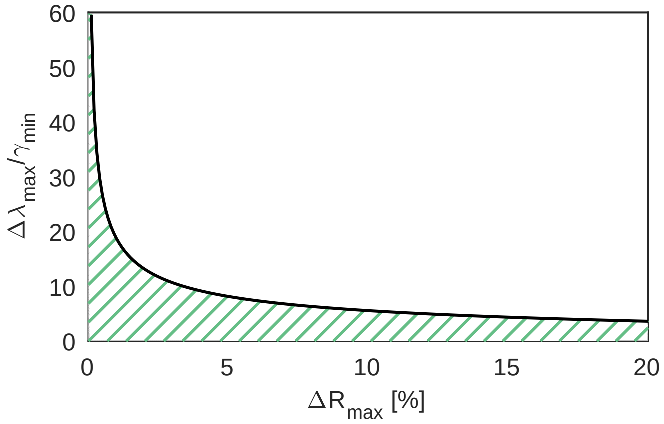

Figure 4.5. Optimum simulation parameter ratio. The hatched region indicates safe parameter sets, i.e., where peaks of a given minimum half-width γ_{min} are always detected. Using parameter sets above the curve, there will be a risk of peaks being completely absent from the simulated spectrum.

There are four solutions, as the value ΔR is found on both sides of the peak, and both near the top of the peak and at the tail. The solution which has a plus sign in both positions describes the location at the positive tail, and will be used in the following.

This equation also describes the optimum ratio between the parameters $\Delta\lambda_{\text{max}}$ and ΔR_{max} for a given γ_{min}, as shown in figure 4.5. Parameter-sets below the curve represent the “safe zone”, yet may be sub-optimal in the sense that they cause more simulation points to be calculated than strictly necessary. Increasing $\Delta\lambda$ such that $\Delta\lambda > \Delta\lambda_{\text{max}}$, there is a risk that peaks of a given half-width γ_{min} will be missing altogether from the spectrum, like in figure 4.4, as such peaks will only be resolved serendipitously. In practice, γ_{min} should be chosen such that it is smaller than the expected minimum peak width. Of course, it is better to err on the side of slightly increased computation time and correct simulations, than faster and misleading simulations. With this approach, a peak of half-width of 0.05 nm is certain to be detected and fully resolved to 0.5%, even when the initial point spacing is $\Delta\lambda = 1.33$ nm.

4.4 Adaptive sampling

A simplified illustration of the working principle is presented in figure 4.6, with the goal of producing a (λ, R)-spectrum using ΔR_{max} (goal resolution) and γ_{min} (minimum peak half-width) as input parameters. First, an optimum initial point spacing $\Delta\lambda_{\text{max}}$ is automatically calculated, such that any peak of a given minimum half-width γ_{min} is certain to cause a perturbation exceeding the threshold ΔR_{max} within the interval, flagging the region for further refinement. A rough simulation is then performed, with the purpose of detecting all spectral features of interest.

After each round of simulations, the difference ΔR between neighboring points is evaluated, to identify regions that exceed ΔR_{max}. These will be further refined by subdivisioning. New points inherit the ΔR-value of its parent in that round, such that subdivisioning does not continue indefinitely.

When the difference between two points no longer exceeds ΔR_{max}, the space is subdi-

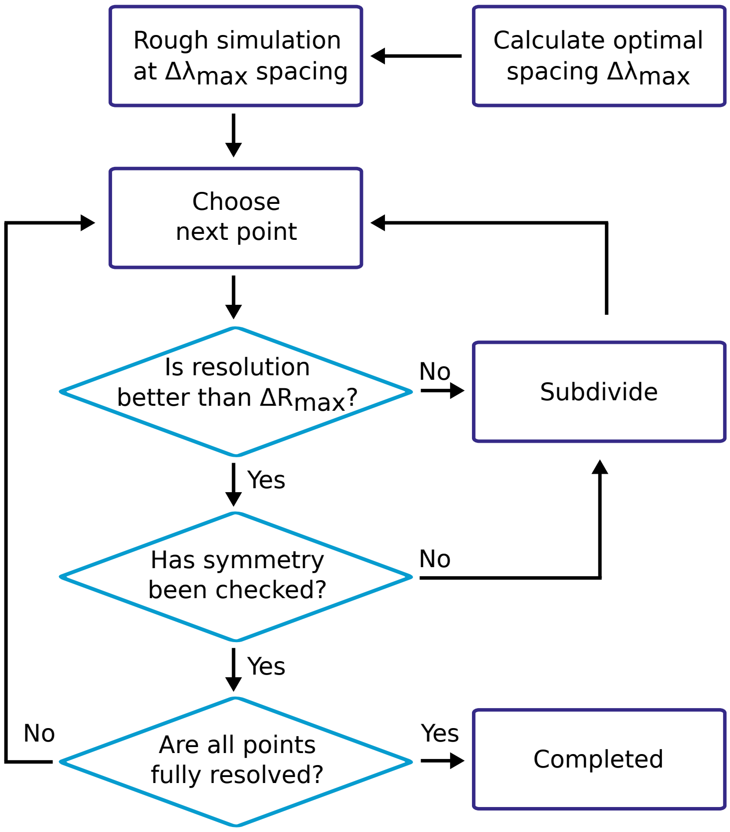

Figure 4.6. Working principle behind the algorithm. An initial rough simulation is performed in order to detect all relevant features. Then, each peak is further resolved by adaptive subdivisioning until the desired resolution is achieved. At this point, a symmetry-check is performed in order to ensure that two points with similar values are not just placed symmetrically around a peak. From ref. [61].

vided one last time as a symmetry-check. It is entirely possible for two points to be placed symmetrically around a peak, in which case their difference ΔR could be zero, without the upper part of the peak having been resolved. The symmetry-check safe-guards against this. If the difference still does not exceed ΔR_{max}, the region is considered fully resolved. Thus, once a peak is detected, i.e., at least one point satisfies the criterion $\Delta R > \Delta R_{\mathrm{max}}$, the entire peak always becomes fully resolved.

4.5 Systems integration

The code is written to be self-documenting in accordance with The Elements of MATLAB Style by Richard Johnson [65]. To demonstrate the algorithm, it was applied to three functions, namely a generator-function, which generates model-spectra as superpositions of lorentzians of given scale- and location parameters, useful for testing, a wrapper-function which calls the RCWA-toolbox GD-Calc, and a wrapper-function for the `MNPBEM` package. The latter package simulates SPR phenomena in the context of nanoparticles.

When simulations contain discontinuous steps of height exceeding the desired ΔR_{max}, no solution exists that satisfies the resolution criterion. In this case, the algorithm would futilely continue to refine the region indefinitely, therefore, a maximum iteration limit of 32 is implemented. As the x-axis step size is halved for each iteration, this limit allows a refinement to $1/2^{32}$th of the original x-axis resolution, which is much more than sufficient for a continuous spectrum.

As the algorithm itself merely analyzes the function outputs in order to determine optimal subsequent function inputs, in principle, any 1D simulation function can be implemented. Although the algorithm was originally developed specifically for optical spectra, where the transmission or reflection is always between 0 and 100%, it might be useful to many other types of simulations where a narrow peak is simulated within a wide interval. When the peak maximum is not 100% but an arbitrary number Y, the algorithm will still be useful by simply multiplying the y-resolution by Y. However, if peak height can vary over several orders of magnitudes for varying input parameters, an absolute value for y-axis resolution is no longer suitable. It may be possible to implement a scheme for dynamically setting a relative y-axis resolution, and could be within the scope of a future version of `asasim`.

4.6 Computation time

Significant speed gains are possible by utilizing the multi-core architecture of modern computers. In order to enable parallelization, the simulation effort must be split into well-defined packages to be distributed on the processor cores. However, as the wavelengths to simulate are only known after each iteration, where regions to further resolve are identified, for parallelization, the spectrum is iteratively scanned with increasingly high resolution in the relevant regions. This also makes it impossible for the system to display a progress bar, as the end-point is effectively unknown.

In terms of computation time, decreasing ΔR_{max} causes more points to be calculated on the R-axis, but this also increases $\Delta\lambda_{\mathrm{max}}$, reducing the number of points to be calculated

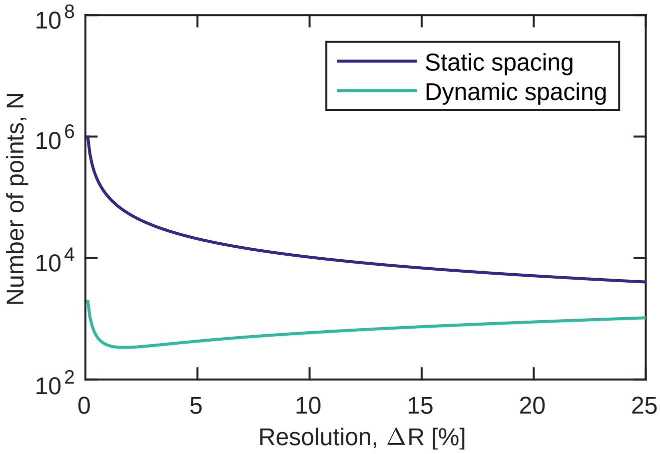

Figure 4.7. Number of points simulated as function of R-axis resolution, using $\gamma = 0.5$ nm. As the number of points simulated scales linearly with time, the dynamic method is a couple of orders of magnitude faster than the static, and in this example, the dynamic method has a time-optimum parameter set at ΔR=1.7%. From ref. [61].

initially on the λ-axis. In the simplest possible model, consider a spectrum only containing a single lorentzian peak with a half-width of γ. The number of points simulated on the fully resolved peak is $N_R = 2/\Delta R$, and the number of points to be simulated statically across the spectrum is $N_\lambda = (\lambda_{\max} - \lambda_{\min})/\Delta\lambda$. The total number of points to be simulated adaptively is then roughly

$$N = \frac{2}{\Delta R_{\max}} + \frac{\lambda_{\max} - \lambda_{\min}}{\Delta\lambda_{\max}} \tag{4.8}$$

Using this equation for estimating the number of simulation points, the two methods were compared for speed as shown in figure 4.7. It is clear that the adaptive method is generally a couple of orders of magnitude faster than the static method. The figure also illustrates the computational optimum for the ΔR and thus $\Delta\lambda$ parameters, at a given minimum necessary peak half-width $\gamma_{\min}$. Time-optimal parameters could be determined by combination of equations 4.7 and 4.8 and solving $\frac{dN}{d\Delta R_{\max}} = 0$, but this becomes rather unwieldy. As figure 4.7 indicates, the total number of simulated points does not vary steeply for similar values of ΔR, and so the choice of resolution is perhaps more a question of personal preference.

For comparison, in order to achieve the same R-axis resolution with static sampling as with adaptive sampling, the static first-axis point spacing must equal the smallest distance between two points separated by $\Delta R_{\max}$ on the second axis. When only a low resolution on the R-axis is required, or when the spectrum is dense with peaks, the advantage of `asasim` diminishes. However, the method especially shines for single-mode resonances in broad intervals. For example, to resolve a peak of half-width $\gamma = 0.5$ nm at $\Delta R = 1\%$ resolution on the steepest part in an 800 nm interval, the adaptive resolution varies between 0.0046 nm and 4.6 nm, depending on the local spectral features. To achieve a static resolution of 0.0046 nm, more than 170,000 points would be required. With adaptive resolution, the same is achieved with 468 points, making the simulation 374× faster.

Summary

To summarize, the `asasim` algorithm has been described and elaborated in aspects which were omitted from the publication [61] (appendix A). The working principle has been explained, optimum parameters have been derived and a speed comparison has been given. The analysis here was focused on lorentzian lineshapes, but an identical derivation could be performed for other line shapes as well. The maximum permittable point spacing would then be shorter, as the perturbation would not extend as far from the peak center, as in the case of the "fat tails" characteristic of a lorentzian. For simple resonance spectra, simulation time can routinely be reduced by two orders of magnitude without compromising resolution in regions of interest, and with a minimum of *a priori* information. The algorithm was employed for simulating sensor behavior in ref. [66] (appendix B), and this is the topic of the following chapter.

Chapter 5
Optimization

PHOTONIC crystal slab sensors are commonly fabricated by deposition of high-quality dielectric thin films in vacuum. Many of the sensors used in this project were fabricated in this manner, with a thin layer of TiO_2 as waveguide core. These sensors provide a sensitivity in water of approx. 90 nm/RIU. However, the necessity of typical cleanroom equipment makes fabrication much more expensive, and prone to long periods of standstill during equipment downtime.As an alternative, polymeric PCS sensors were focused on, as originally described by Hermannsson et al. [26]. Despite their advantages of cheaper and simpler fabrication, their approx. three times lower sensitivity and environmental responsiveness are primary drawbacks. However, with proper optimization, polymeric PCS sensors can still be competitive with more expensive, traditional sensors.

This chapter presents optimization efforts in most aspects involved with the sensor. It is found that thermal drift and fluctuations are in fact amplified several times by the materials constituting the sensor, further necessitating the proposed method for thermal compensation. Due to high-performance thermal compensation, waveguide core instability was observed, as will be discussed. Finally, the resulting sensor signal is really only as good as the instrumentation that reads it out, and the algorithm that processes it. Therefore, the experimental setup is optimized, and a number of analysis algorithms are compared for performance and speed.

5.1 Fabrication

For TM-mode devices, an 80 nm high-refractive index layer of TiO_2 was deposited by IBSD. Although all internal temperature readings appeared nominal at $T < 30\,^\circ\mathrm{C}$, there was a tendency for the yield of functional sensors to decrease throughout the day, as illustrated by the sensor micrographs toward the righthand side of figure 5.1. The standard deviation of the resonance wavelength also had some correlation with chamber temperature as indicated by figure 5.2. Thus, it was concluded that the internal thermometers of the IBSD did not measure the actual sample temperature, which these observations indicated had been much higher. The glass transition temperature of Efiron PC409-AP is 70 °C, so for loss of nanostructuring, the actual temperature would have to exceed this. From this investigation, a process recipe employing improved cooling was created and used for all subsequent TiO_2 depositions. The yield from thermal damage then approached 100%.

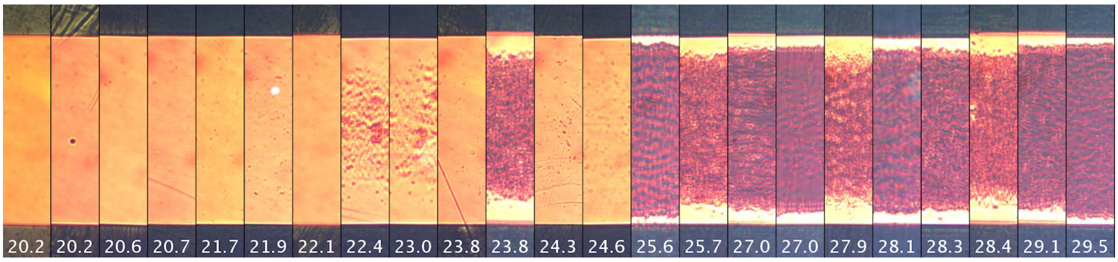

Figure 5.1. Fabrication quality control micrographs. The clarity of PCS sensors would deteriorate in correlation with chamber process temperature, shown in degrees Celsius below each micrograph.

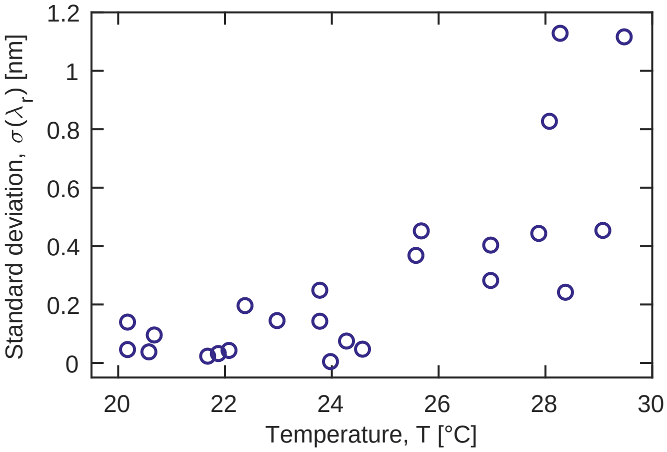

Figure 5.2. Fabrication quality control resonance investigation. The standard deviation of the resonance wavelength across the sensor increases with chamber temperature.

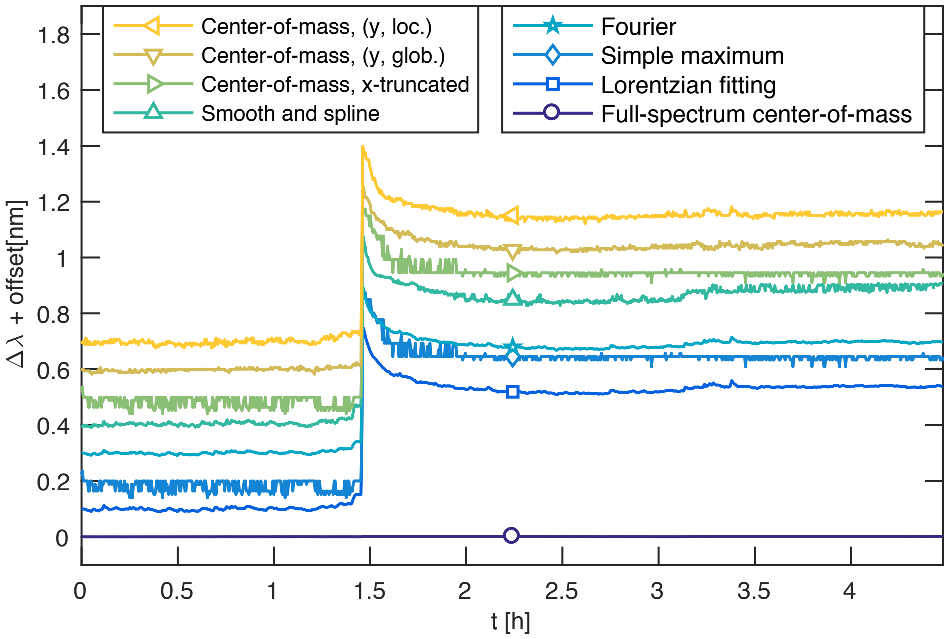

Figure 5.3. Comparison of data processing methods, offset by 0.1 nm. Most methods achieve similar sensitivity (S), but the amount of noise (σ) and thus detection limit varies.

5.2 Analysis

In practice, the resonance wavelength λ_r is tracked by recording a wavelength-resolved spectrum of reflectivity. At resonance, the reflectivity approaches 100%, giving rise to a lorentzianeak centered at the resonance wavelength. When λ_r is the descriptor of interest, each spectrum must be reduced from a vector of wavelength-resolved reflectivity values, to a single resonance wavelength value, sometimes referred to as the peak wavelength value (PWV).

The algorithm used to extract resonance wavelength, also referred to as the PWV[14], appreciably influences interpretation and limit of detection. Just like optimizations to the readout instrumentation or the sensor itself could improve performance, the right choice of algorithm plays an important role.

5.2.1 Finding the resonance

Implementations where the readout parameter is an intensity value rather than a wavelength value greatly simplifies detection hardware (a single photodiode is sufficient) and analysis. However, recording the full spectrum enables other advantages, such as having more points for fitting, multiplexing, and the possibility of reference regions. Using an imaging spectrometer, 1D [67], 2D [68, 14] or even 3D [18] spatial resolution can furthermore be achieved.

Table 5.1. Comparison of algorithm performance. [a]Normalized by division of the shortest time. Best limit of detection (LOD) highlighted.

Method	LOD (x10^{-4})	Noise (x10^{-}3)	Sensitivity	CPU-time^{a}
Full-spectrum center-of-mass	124.0	0.3	0.02	1
Lorentzian fitting	8.7	25.3	29.04	2,216
Simple maximum	18.9	59.2	31.31	1
Fourier	8.0	20.9	26.25	14,584
Smooth and spline	9.8	30.6	31.24	1,055
Center-of-mass, x-truncated	18.8	58.7	31.30	3
Center-of-mass, (y, glob.)	6.3	18.8	29.94	3
Center-of-mass, (y, loc.)	10.9	33.5	30.74	5

In order to compare, the different analysis methods were applied to the same time series, where the sample refractive index is artificially increased at $t = 1.5$ h by adding sucrose. This enables an estimation of sensitivity, whereas the long flat period before the addition is used to estimate the steady-state noise. Figure 5.3 shows the results, as summarized in table 5.1. The simplest and computationally fastest way to express the resonance wavelength is the wavelength at which the reflectivity is highest. However, this approach is limited by the resolution of the spectrometer detector, as λ_r can never assume values between two “bins” on the detector. Furthermore, as this approach effectively uses data in only one bin, there is a large waste of available information. This also makes the method exceedingly fragile to noise in the spectrum, as shot noise will constantly cause neighboring bins to momentarily be at the maximum. It is, however, computationally fastest, and thus it is used to benchmark alternative methods against. The CPU-times in table 5.1 are normalized to this “simple max” duration.

Conceptually a combination of the plain maximum and polynomial fitting approaches, an alternative is to find the maximum after smoothing, thereby taking into account data at neighboring pixels and reducing the impact of noise. Smoothing by spline fitting is one way to achieve this, and the method exhibits a decent detection limit, but computation time is ~1000 times longer, compared to the simple-max method.

Much like the mathematical spline, “anything” can be fitted to a Fourier series. Among the examined algorithms this is the slowest, being >14 000 times slower than the simple maximum. It does, however, perform very well, achieving a detection limit that is among the lowest in this study.

Theoretically, resonant reflections are described by a lorentzian but due to imperfections in the sensor itself and/or readout instrumentation, the peak is often skewed from a symmetric lorentzian, instead displaying a Fano lineshape. Furthermore, lorentzian fitting is >2000 times as computationally demanding, compared to the simple-max approach.

The method tested here that yields the lowest noise without sacrificing sensitivity, and thus achieves the best detection limit, is the globally y-truncated center-of-mass approach. Incidentally, this was also independently found in a study of SPR analysis methods. This

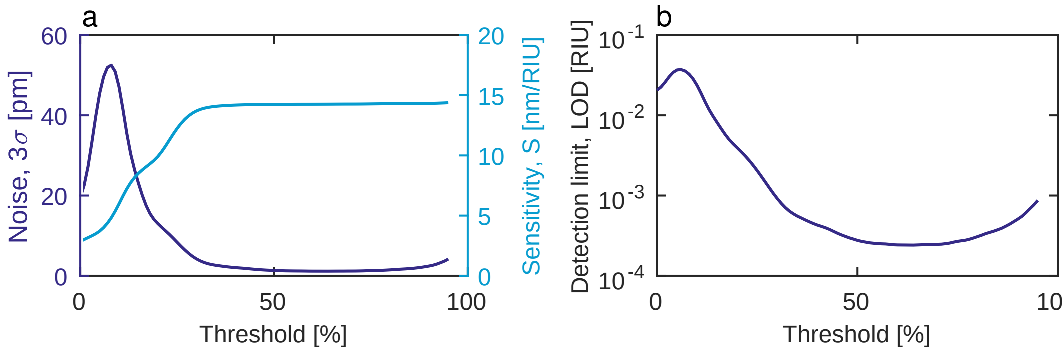

Figure 5.4. Influence of centroid threshold on a) noise and sensitivity, and b) detection limit. Intermediate threshold values provide optimum performance. The poor LOD is due to the particular sensor used being subpar.

method is also computationally comparable to the simple-max approach. In the y-truncated approach, a y-axis threshold is provided. Data points below this value receive zero weighting in the the center-of-mass calculation. Thus, only the relevant data points (those relating to the resonant peak) are used in the analysis, and the points to be analyzed is determined by their value on the intensity-axis, rather than by selecting a window on the wavelength-axis. It should be noted that even lower noise can be achieved by selecting a narrow, static wavelength interval. This approach may be suitable when very small shifts are expected, but for larger changes, the peak might leave the interval. Broadening the interval then causes a loss of sensitivity, trending toward the situation of the full-spectrum center-of-mass, which has almost zero sensitivity: as the peak only occupies a limited portion of the spectrum, the weight of the background diminishes sensitivity. On the other hand, the noise is lowered, as the peak location fluctuations are equally blurred by the weight of the full spectrum. However, as indicated in table 5.1, this is a poor tradeoff, as the detection limit achieved with this algorithm is the worst among the algorithms tested.

5.2.2 Choice of window

The method used to determine the fitting region can be as important as the fitting method itself, and is rarely stated in the papers that utilize the approach. If a constant interval is chosen, what happens if the peak approaches the edge of the window? Fewer data points will be included, and if the peak shape is asymmetric, the system sensitivity could become slightly non-linear. If an interval is chosen dynamically per-frame, e.g., as the data interval exceeding a certain absolute value, then the interval itself will be subject to noise, which can destabilize the fitting. If the interval is chosen based on a distance from the peak, then a chicken-and-egg situation is at hand, as the method used to find the peak initially may add noise. The choice of threshold also matters to the y-truncated CoM approach. Figure 5.4 illustrates the influence of the choice of threshold on noise, sensitivity and detection limit. Setting it too low means excessive weighting of the background, limiting sensitivity. Setting it too high means fewer points being included, increasing noise. In situations where part of the background occasionally exceeds the threshold, the center-of-mass value is violently shifted away from the resonance, increasing noise tremendously. Thus, an optimal threshold exists, which varies from sensor to sensor. However, as figure 5.4 shows, both sensitivity and noise varies slowly at a threshold around 50%, so this value is usually a good starting point.

Hot pixels are artifacts of unusually high intensity that can sometimes occur on detectors, arising from shot noise or electrical interference rather than actual reflectivity. Hot pixels can significantly disturb the determined resonance wavelength, appearing as transient spikes in a time series. To safeguard against these, the best compromise was found to be to perform a time-average of the full time series, then calculating an absolute intensity threshold based on the relative threshold value. This approach was implemented in the function `speCoM`, which calculates center-of-mass resonance values based on an input relative threshold, after performing a global average to avoid hot pixels.

With detection limit defined as the ratio of noise to sensitivity [20, 22], $\mathrm{LOD} = 3\sigma/S$, the ideal algorithm achieves a low noise without sacrificing sensitivity. For real-time applications, the computation time also has merit.

As discussed, the centroid method was found to yield the best performance and fastest processing speed. Thus, this method was implemented in the function `speCoM`, which calculates the centroid wavelength after thresholding at an input value. It can process 2D or 3D matrices of data. In order to safe-guard against rare yet disturbing hot pixels, i.e., transient bright pixels randomly occurring from noise, a global absolute value is first determined for each line, based on a temporal average of all frames, given the input threshold. Because the absolute threshold value is thus fixed for each, this eliminates another potential source of noise. As is also the case for SPR, the choice of algorithm used for determining the resonance wavelength is of substantial importance to the overall performance of the system [69], and ultimately affects the limit of detection.

Data output by `speImport` is structured as a 3D matrix with wavelength on the first dimension, spatial position on the second and time on the third dimension. As the whole wavelength dimension can be reduced to a single wavelength, namely the resonance wavelength, a data reduction of more than $10^3\times$ is achieved. This reduces the data to a 2D-matrix, which can be represented as a kymograph with time on the first axis. By extracting the resonance wavelength at certain spatial positions, or averaging a spatial interval, the spatial dimension is further collapsed, resulting in a one-dimensional data set, i.e., a time series, which is much more managable than a heavy 3D-matrix.

5.3 Instrumentation

The setup used in this project was originally designed and built in previous work [25], with modifications for optimization. For one, the angle of incidence θ on the sensor is an important parameter. When excitation light is perfectly collimated and aligned, the full illumination zone receives light at normal incidence. However, when collimation or alignment is imperfect, the angle of incidence becomes oblique at certain positions. In order to ensure collimation, a focusing lens is placed in the excitation light path, such that the light

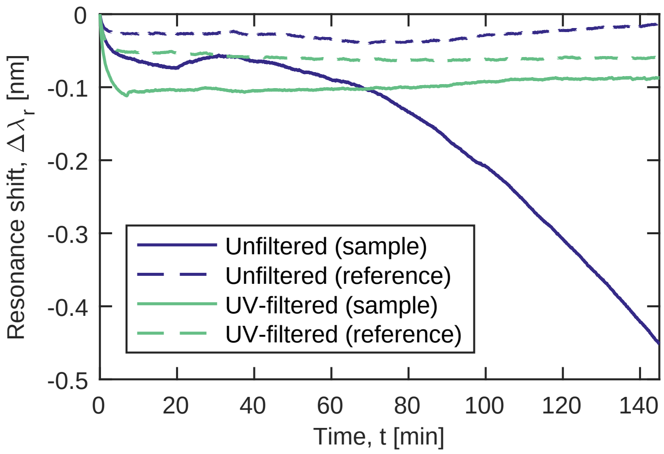

Figure 5.5. Titania-based sensor deteriorating upon UV-irradiation. After a variable amount of time, in this case ca. 60 min, the sensor starts to break down.

becomes focused on the back focal plane of the microscope objective. With proper focusing and matching focal lengths, light exiting the objective will be collimated. When this is not the case, a cone of angles will be incident on the sensor. Thus, the light received at the spectrometer slit represents an average of the irradiation cone of angles, causing a splitting of the resonance [19]. To investigate the influence of improper collimation, a simulation was set up, as shown in figure 5.6. According to these results, even an 8 mrad (<0.5°) angle can cause a splitting of ~50 nm. As these angles are being averaged, that effectively causes a peak broadening from less than 1 nm to more than 50 nm.

One of the many merits of titania is its self-cleaning property, which generates free radicals upon UV irradiation, killing bacteria. However, particularly under alkaline conditions, this reaction would also deteriorate the sensor chemically over time, as shown in figure 5.5. The significant amounts of UV-radiation generated by the laser-driven light source (LDLS). was still strong enough to deteriorate the surface even after passing through 2 mm of PMMA, which absorbs ~90% of UV light. Therefore, when using titania-based sensors, a longpass filter was inserted into the excitation light path.

The modified setup employed is rendering via computer-aided design (CAD) in figure 5.7. CAD-models were acquired from Thorlabs, Princeton Instruments, and Energetiq, and positioned in Blender 2.77 (Blender Foundation, Amsterdam, The Netherlands) to ensure an accurate and comprehensive bill of materials (BOM) prior to ordering components. This approach helped ensure that spatial restraints did not clash with component requirements such as focal lengths. Supporting structures are shown in white, and the setup is built on a breadboard to improve mobility. It was a main design consideration to keep the center of gravity as low as possible, while accomodating the necessary components, in order to minimize the center of mass and thus vibrations. The setup is placed on an optical table, which along with the clamped posts ensure stability. Two nested cage systems of 30 mm and 60 mm are employed to aid alignment, and components near the readout point are mounted on a dovetail optical rail.

Light sources are shown in yellow, and constitute an LDLS, shining through the left-most

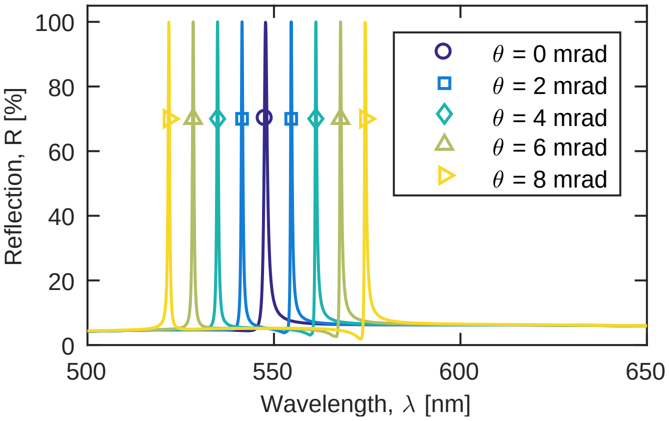

Figure 5.6. Simulated effect of uncollimated light, causing a splitting of the resonance.

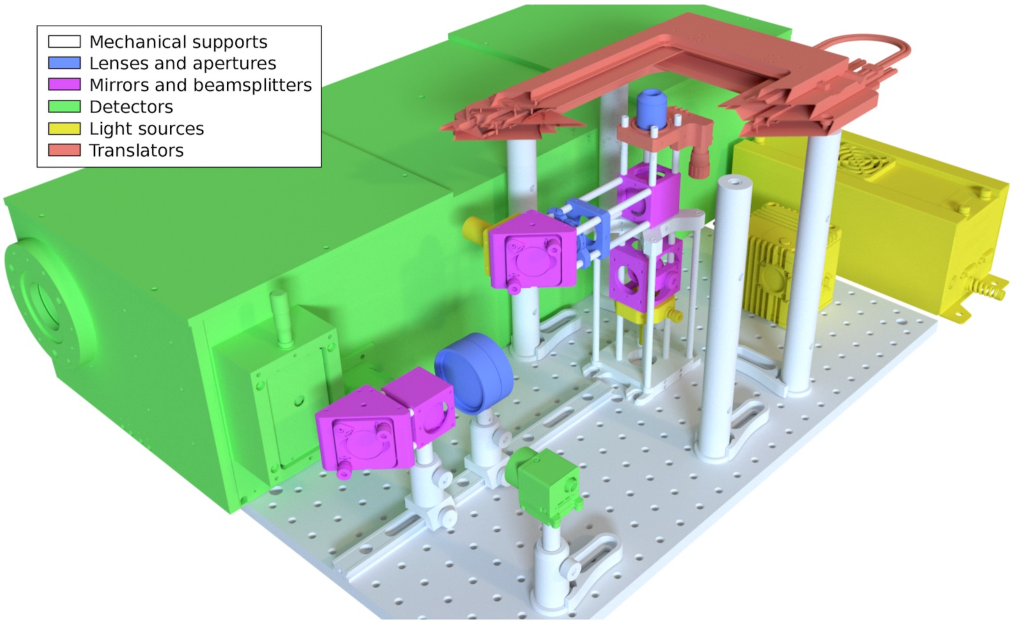

Figure 5.7. 3D-rendering of modified setup. An adjustable mirror and lens improves collimation, and the setup allows an NIR laser to shine through a hot mirror near the bottom of the setup.

fiber collimator. This light is bright and spectrally flat, and is generated from a white plasma contained within the square box on the right, being excited by the laser shown on the right. Another laser (not shown in the image) can be interfaced through the bottom-most fiber collimator. White light is reflected by an adjustable mirror (generally shown in purple) through a plano-convex lens and an aperture (generally shown in blue), before reaching a 50:50 beamsplitter and being reflected up through a microscope objective. The mirror and lens is adjusted so as to focus the light on the back focal plane of the objective, in order to ensure collimated excitation light exiting the objective. The objective is mounted on a manual z-translation mount (shown in red), and the sample wafer (not shown) is mounted on a motorized xy-stage, shown cut-through for clarity. Light reflected by the sample wafer is directed back through the objective and beamsplitter, reflected by a hot-mirror on the bottom towards a 180 mm tube lens. Detectors, namely an imaging spectrometer (Acton SP2750, Princeton Instruments, NJ, USA) and a color CCD, are shown in green. A polarizing beamsplitter ensures that resonant reflections are received by the imaging spectrometer, whereas the other polarization is directed to the color CCD and used for positioning. The polarizing beamsplitter has a higher polarization purity in the transmitted beam (1000:1 extinction ratio) compared to the reflected beam (down to 20:1), and so ideally, the imaging spectrometer slit should be in continuation of the dovetail rail. Due to space constraints, a 90° mirror was implemented instead. The imaging spectrometer slit and color CCD are positioned at the focal point of the tube lens.

The bottom-most fiber collimator allows interfacing of an NIR laser. The hot-mirror ensures full reflection of visible light, and full transmission of NIR light. The fiber collimator is installed in a translation mount for alignment. Assuming sufficient collimation from the fiber collimator, the laser is then focused on the sensor surface by the microscope objective, when the objective height is adjusted to provide a focused image. This setup provides sufficient degrees of freedom to ensure focusing, collimation and alignment of the two input light paths and two output light paths simultaneously. When complementary temperature measurements were needed, a pyrometer would be mounted on the motorized stage, at an angle to avoid shining light directly into the measuring window.

The discussion of collimation angle also applies to the alignment of the excitation illumination. Even when these rays are perfectly collimated, if they do not center on the microscope objective, they will exit at an angle, causing a peak splitting. For this reason, the adjustable mirror was added to the collimated fiber, allowing easy and precise adjustment of the angle of incidence.

5.4 Temperature

Changes in water temperature changes its refractive index by 1×10^{-5} RIU per 0.1 °C [70]. Therefore, thermal control and/or compensation is necessary for high-resolution refractometric measurements. One way to enable this is by depositing a droplet of polymer to cover part of the sensor area, effectively producing a reference region of known refractive index. As refractive index contrast to the waveguide core is required, the refractive index must be lower than that of the core. This is less of a limitation for titania-sensors (n_D ~2.61 RIU), but as the

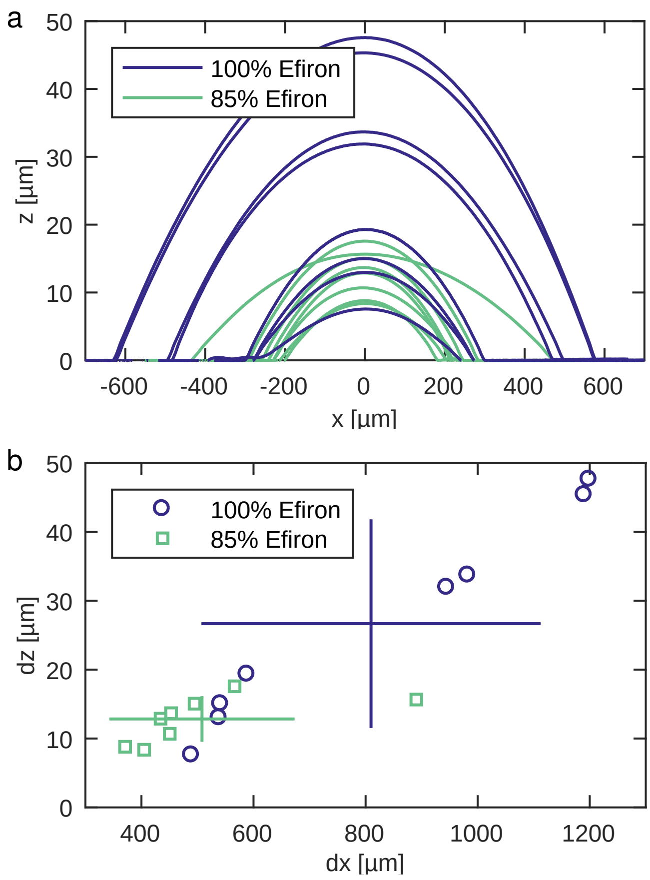

Figure 5.8. Characterization of thermal probes. a) All profilometer measurements overlaid, showing spatial extent (x) versus height (z). Note the unequal axis ranges. b) Height (dz) plotted against diameter (dz). Lines indicate the mean plus/minus one standard deviation. Diluting the polymer generally enables smaller droplets.

polymeric PCS sensors have a core refractive index of n_D =1.59 RIU, the thermal probe material is limited to a value below this. Furthermore, for readout without spatial resolution, i.e., using a point probe spectrometer rather than an imaging spectrometer, the refractive index must be different to that of the sample. Furthermore, it should be possible to fabricate the region as a thin layer that only occupies part of the sensor area. Thus, with the added bonus of simplifying fabrication and reducing chemical compatibility issues, the low-refractive index polymer used for the nanostructured substrate, Efiron PC409-AP (n_D ~1.40 RIU), was chosen for thermal probes. Assuming a 0.5 nm line width, this allows a dynamic range of Δn_D =0.03 RIU, corresponding to a sucrose concentration of >200 mg/mL. In order to deposit thermal probes, i.e., regions on the sensor with a known refractive index, a number of approaches were attempted.

The most straight-forward method is manual deposition, by dipping a pipette tip into a polymer solution, and then transferring tiny droplets onto part of each sensor. Like HI01XP, Efiron does not properly cure in the presence of oxygen. Droplets were therefore cured in a nitrogen atmosphere. By using Efiron diluted to 85%, smaller droplets could be deposited manually, with heights down to less than 10 µm, as shown in figure 5.8. This is still far above

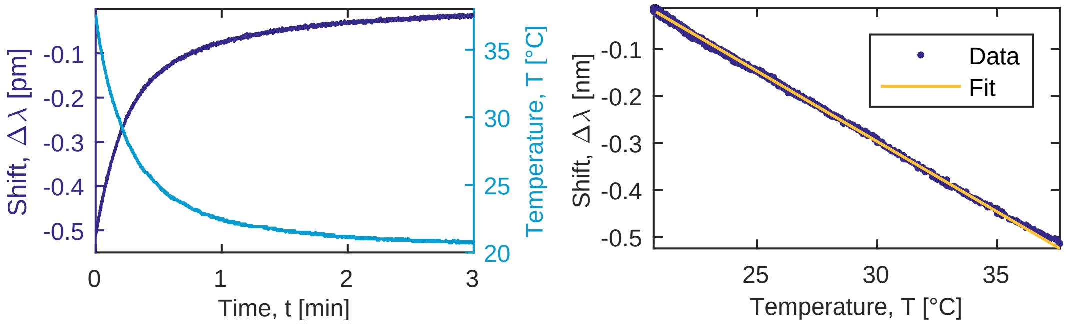

Figure 5.9. Thermo-optic coefficient investigated by a) deliberately inducing a temperature perturbation. b) Resonance wavelength shift is correlated with temperature as measured with a pyrometer. $d\lambda/dT$=-30.0 pm/°C, r^2=99.86%, N=1801. From ref. [66].

the penetration depth of $\hat{e}$ =138 nm, allowing such manual droplets to be embedded within a shallow and wide (e.g., 20 µm×2 mm) channel. However, as the size and position of manually deposited droplets are difficult to control, alternative methods were investigated.

One option is to use photo lithography to accurately define areas of photoresist, which could then be spincoated to the desired thickness. However, as all three polymers would have to be compatible with all physical (e.g. sonication) and chemical (e.g., development) aspects of the process flow, this proved challenging.

As accounted for in ref. [66] (appendix B), from which the following paragraph originates, the thermal probe resonance response is highly correlated with temperature, as ascertained by recording a deliberate thermal perturbation by the two complementary methods, i.e. pyrometer and photonic crystal readout.

The amplified temperature sensitivity due to thermally induced refractive index changes in the sensor stack was investigated by adding a droplet of heated water to a thermally equilibrated volume of water sitting on a titania-type sensor. The result is shown in figure 5.9. The temperature was measured using a pyrometer simultaneously with resonance shift monitoring. As the refractive index sensitivity of these sensors was $d\lambda/dn = 90$ nm/RIU, the effective thermo-optic coefficient of the sensor in water was determined to be $dn/dT = 3.3 \cdot 10^{-4}$ RIU/°C, an amplification of 3.3× compared to the thermo-optic coefficient of water itself [70], exacerbating the need for thermal referencing.

With effective temperature compensation, a flat baseline can be achieved even in the presence of drift and sample perturbations, as shown in figure 5.10. A steady baseline is disturbed by the addition of warm and cold water at $t = 1.1$ min and $t = 2.6$ min, respectively. The only difference here would be a slight temperature variation, which is effectively canceled by the thermal compensation method, maintaining a stable baseline. Then, at $t = 4.0$ min, buffer is added. This time, a perturbation is caused by both the mixing of buffer salts with the existing sample, as well as a slight temperature fluctuation. Due to the independence from thermal contributions afforded by the method, sample mixing time is decoupled from the thermal equilibration process, and full mixing is observed to take ~ 15 s.

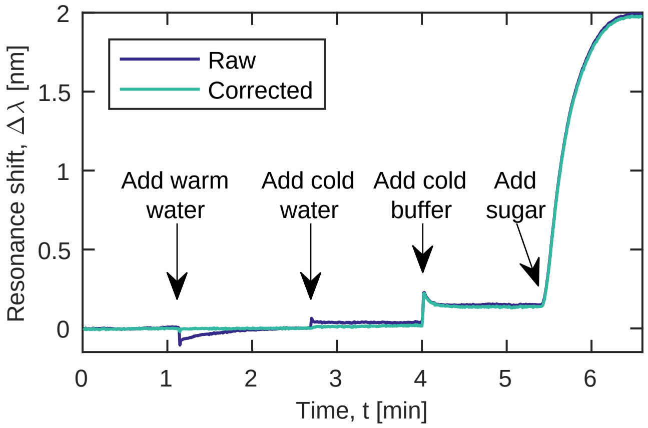

Figure 5.10. Demonstration of thermal compensation efficacy. Temperature perturbations are effectively cancelled by thermal compensation, ensuring a stable and drift-free baseline. With thermal effects accounted for, the time for full mixing of the buffer becomes clearly visible at t=4 min. From ref. [66]

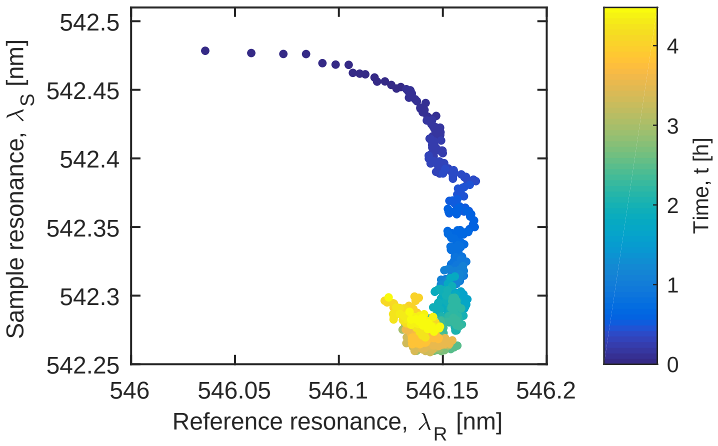

Figure 5.11. Non-correlated resonances during core swelling. Sample resonance is plotted for λ_S versus the resonance in the reference region (λ_R) over time. The blue-shifting of the sample resonance over the first ~ 1.5 h may be due to water absorption into the exposed waveguide core. The shielded reference region is relatively stable during the period.

5.5 Waveguide core swelling

For the case of polymeric sensors, an erratic behavior was observed under certain circumstances. As shown in figure 5.11, when measurement times are low, the reference probe can sufficiently account for fluctuations of polymeric PCS sensors, and will effectively cancel noise and drift. This is likewise the case after a sufficiently long equilibration time. However, on intermediate time scales, steady-state resonance shifts are not correlated with temperature, and the reference probe can no longer account for the shifts observed. It is hypothesized that this is caused by water absorption into the core-polymer. If water displaces air in an otherwise stationary polymer matrix, the layer thickness should remain constant while the effective refractive index should increase. If water causes a swelling of the polymer network, the thickness should increase and the refractive index decrease.

The latter explanation was supported by VASE as shown in figure 5.12a, indicating a slight increase in core thickness and a concomitant decrease in the core refractive index. It should

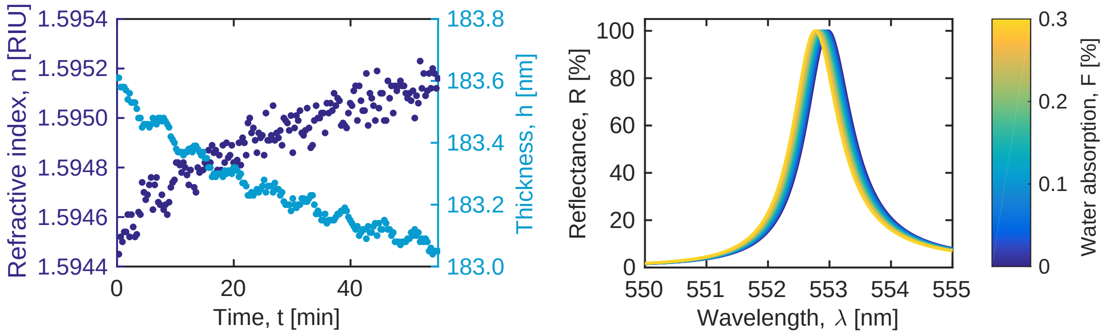

Figure 5.12. Water degassing investigated by a) ellipsometer, indicating concomitant core layer shrinking and refractive index increase, and by b) RCWA, indicating a 215 pm resonance shift in response to the changes measured by ellipsometry. The result is consistent with the direct sensor readout data.

be noted that the measured difference on the order of some Ångströms may be outside the accuracy of VASE, but it may be within its limit of precision.

The experimental observations from the PCS sensor and VASE were supported by RCWA. The effective core refractive index n_{eff} was modelled as

$$n_{\text{eff}} = n_1 F + n_2(1-F) \Leftrightarrow \tag{5.1}$$

$$F = \frac{n_{\text{eff}} - n_2}{n_1 - n_2} \tag{5.2}$$

where n_1 is the refractive index of water, F is the water fraction, and n_2 is the refractive index of the core polymer. It was found that a 0.55 nm core thickness increase and a 5×10^{-3} RIU core refractive index decrease should indeed correspond to a 210 pm blueshifting. Assuming the effective core refractive index to be described by a mass-fraction dependent combination of water and the high-refractive index polymer, this degree of swelling corresponds to a 0.3% water-uptake, not uncommon for polymers.

One method for quantifying the time until steady state is to look at the time derivative of the temperature-compensated graph. When stability has been reached, the reference and sample regions are proportional and temperature effects are effectively cancelled out, in which case the time derivative approaches zero (barring noise). To investigate when this occurs, a 1-hour rolling time derivative ($d\lambda/dt$) was calculated, and the first time when it reached zero was taken as the equilibration time. This generally occurs after approx. 1.5 hours.

Once the sensor has been primed by wetting, it should be ready to receive a sample. However, if water is able to penetrate the waveguide core, would other molecules be able to as well? As a pilot experiment, a sucrose solution was added after overnight equilibration, as shown in figure 5.13. The signal changes appreciably, but the thermally compensated signal stays rather constant after mixing, indicating that at least sucrose does not absorb into the polymer matrix.

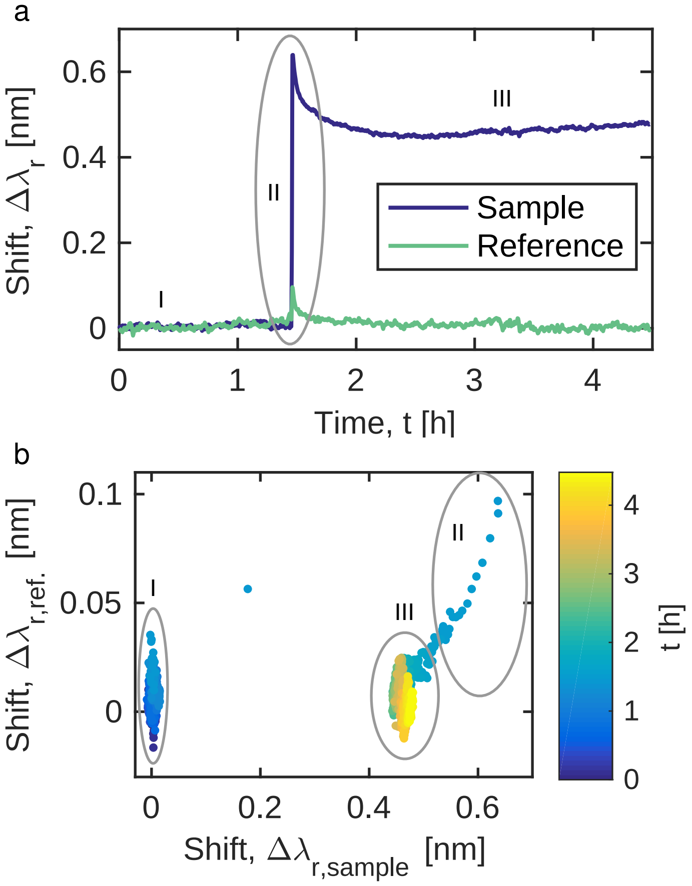

Figure 5.13. Sample equilibration investigation, with data displayed as a) time series and b) resonance correlation. The rapid re-equilibration indicates that sucrose does not access the waveguide core by absorption.

Summary

In this chapter, a number of approaches to determining resonance wavelength have been compared. The choice of algorithm is important as it directly affects the performance of the sensor. The “globally y-truncated centroid” algorithm was found to provide the best detection limit at a low computational cost.

With a proper choice of thermal probe material, readout without spatial resolution is possible. An amplified temperature sensitivity of 3× for titania PCS sensors was documented, emphasizing the need for temperature compensation. It was shown that with proper temperature compensation, a fluctuation- and drift-free signal baseline can be maintained, even in the presence of sample perturbation. This also allows investigations of transient effects, which might otherwise be obscured by delay from thermal control.

With isolation of thermal effects, waveguide core swelling was established, as supported by VASE and RCWA. This poses an important limitation to the polymeric class of sensors, as they must be wetted for several hours prior to use. This makes them unsuitable for use as free-standing sensors, but makes them suitable for microfluidics integration, where a chip may be wetted prior to packaging. In the next chapter, we will have a look at potential microfluidics applications.

Chapter 6

Microfluidics

WORK on microfluidics systems has largely been motivated by the promise of LOC devices for use at the POC. This is particularly relevant to developing countries, where educated personnel and necessary laboratory facilities may be scarce [1]. The basic promise of LOC devices is that they take an analysis, which might involve several processing steps on multiple instruments in a laboratory, and integrate them onto a single chip [51]. Microfluidic components allow, e.g., generation of droplets of an adjustable size, or sorting of molecules via diffusion. These two examples have been investigated in the context of PCS sensor integration, which is the topic of this chapter. We will first look at how the diffusion length can be estimated using an integrated PCS sensor, how the microfluidics dimensions influence the system, and discuss the feasibility of quantitative diffusion measurements using this method. Towards the end of the chapter, droplet microfluidics will briefly be described.

6.1 Monitoring diffusion length

A microfluidic H-filter is a classic microfluidic components, which enables passive sorting of particles and molecules by size. As illustrated in figure 6.1, two liquid streams meet at the horizontal bar of the "H", and co-flow laminarly, i.e., without any convective mixing. The only way for a particle or molecule to transport from one stream to the other is through diffusion, which according to equation. 2.41 is related to the size of a molecule. For label-free investigation of diffusion in a microfluidic H-filter, it was integrated with a PCS sensor, as will be explained in this section.

The simple microfluidic architecture of an H-filter, favoring wide channels, is suitable for rapid prototyping techniques such as adhesion bonding (see figure 6.2a). By laser-cutting into adhesive tape, channels are defined where the tape is ablated, and a tight seal can be formed with a flat plastic part. The height of the tape was measured by using the channel as a makeshift Fabry-Pérot etalon (figure 6.2a, and then analyzing the produced interference pattern (figure 6.2b). As discussed in section 2.1.5, the FSR of a Fabry-Pérot etalon then reveals the height of the cavity, i.e., the adhesion layer thickness. The figure also illustrates how a simple straight channel, with a single inlet and outlet, can be rapidly prototyped by laser cutting and adhesion bonding.

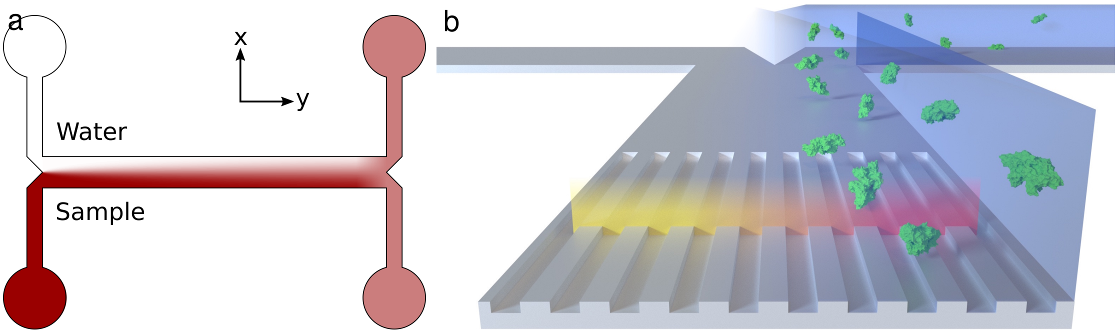

Figure 6.1. Principle of the microfluidic H-filter, shown a) schematically and b) conceptually. Two liquids co-flow and mix only by diffusion, allowing small molecules (blue) to transport across the channel, whereas larger molecules (such as the BSA molecule shown in green) remain in one liquid stream. An integrated PCS sensor measures the diffusion profile along a line, as the increased refractive index from solutes cause a redshifting of the resonance.

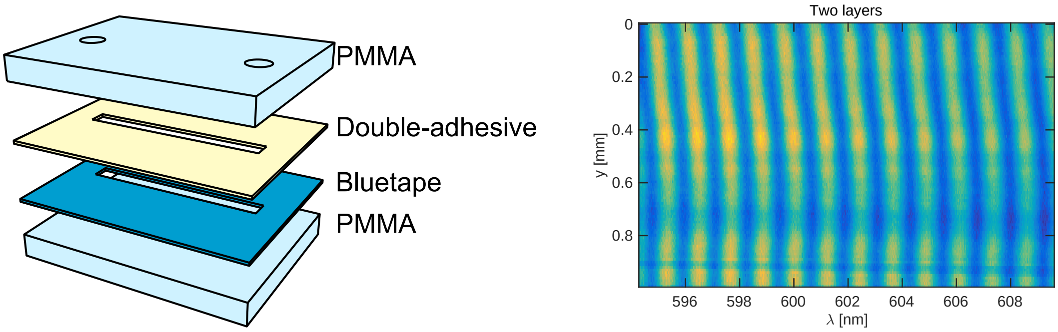

Figure 6.2. Makeshift Fabry-Pérot etalon for measuring layer thickness. a) Schematic illustration of the layer stack. b) Sample interference pattern, showing an FSR, which reveals the cavity height and thus layer thickness.

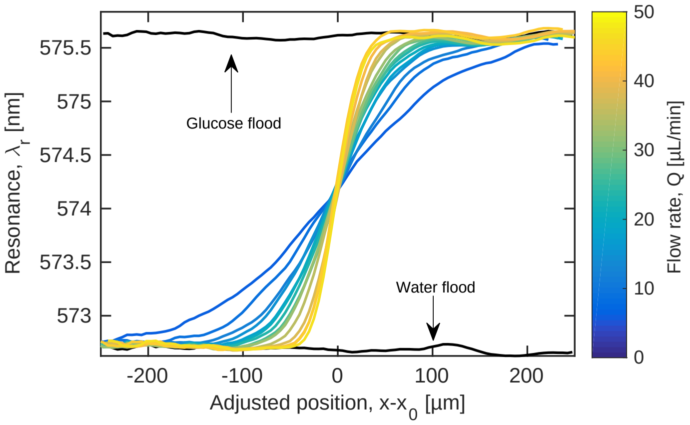

Figure 6.3. Concentration profiles in adhesion-bonded device. The diffusion profile becomes sharper at higher flow rates, which reduces time for diffusion.

This simple channel system performed quite well, and diffusion profiles could be obtained as shown in figure 6.3. Here, the diffusion length is measured at the sensor surface, i.e., at the bottom of the channel. Because of the parabolic flow profile, deep channels result in a concentration profile perpendicular to the bottom of the channel, which is undesirable. This effect can be neglected when the time for diffusion is much shorter than the average convection time, blurring the gradient

$$L = \sqrt{2Dt_{diff}} \Leftrightarrow \tag{6.1}$$

$$t_{diff} = \frac{L^2}{2D} = \frac{(0.5\cdot 10\cdot 10^{-6}\ m)^2}{2\cdot 5.9\cdot 10^{-11}\ m^2/s} = 0.2\ s \tag{6.2}$$

$$t_{conv} = \frac{\Delta x}{v_{avg}} \tag{6.3}$$

$$v_{avg} = \frac{Q}{wh} \Rightarrow \tag{6.4}$$

$$t_{conv} = \frac{\Delta x wh}{Q} = \frac{20\cdot 10^{-3}\ m\cdot 1\cdot 10^{-3}\ m\cdot 10\cdot 10^{-6}\ m}{2\cdot 10^{-11}\ m^3/s} = 10\ s \tag{6.5}$$

$$v_x(y,z) = \frac{4h^2\Delta p}{\pi^3\eta L}\sum_{\text{n,odd}}^{\infty}\frac{1}{n^3}\left[1-\frac{\cosh(n\pi\frac{y}{h})}{\cosh(n\pi\frac{w}{2h})}\right]\sin\left(n\pi\frac{z}{h}\right) \tag{6.6}$$

$$v_x(y,z) = \frac{\Delta p}{2\eta L}(h-z)z \tag{6.7}$$

Another consequence of the no-slip boundary condition is that the velocity profile has a parabolic shape, such that the flow velocity is higher at the center of the channel than near the walls. Equation 6.6 describes this for a rectangular channel [51], and is illustrated in figure 6.4, which also showns that for wide channels, edge-effects along the y-dimension are only influential in a very limited part of the channel. When measurements are not done near the wall,

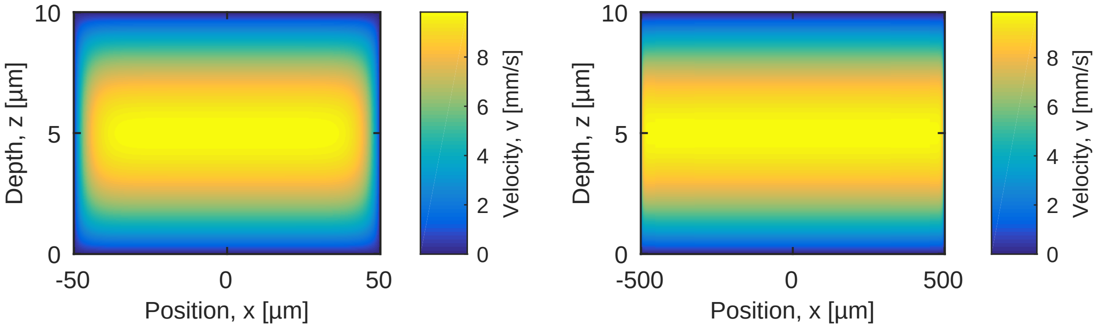

Figure 6.4. Parabolic flow profile typical of pressure-driven flow. a) In a narrow channel, velocity is reduced along much of the x-dimension, while it is almost constant along x for b) a wide channel.

which is the case in this work, the flow velocity profile is well-approximated by two parallel plates, equation 6.7, which in this case gives less than 5% error for 90% of the channel width. The consequence is that the convection time to arrive at a downstream position y is shorter in the center of the channel than near the wall. As diffusion length scales with this residence time, diffusion will have transported species further across the boundary (in the x-direction) near the wall than closer to the center, giving rise to a butterfly-shaped concentration profile. The PCS sensor has a penetration depth on the order of a few hundred nanometers, so this is an important effect. However, as diffusion also occurs in the z-direction, i.e., perpendicular to the channel floor (where the sensor is located), this residence time differential cancels when the diffusion length $\bar{x}$ is comparable to the channel depth. As $\bar{x}$ scales with the square root of time, the butterfly effect is much more prominent for deep channels such as those fabricated by rapid prototyping ($h \approx 100\,\mu\text{m}$), compared to those fabricated by PDMS casting ($h \approx 10\,\mu\text{m}$).

As the equations indicate, in a channel of 10 µm height, molecules can be transported from wall to interior with a anverage diffusion time of 0.2 s. By comparison, the average convection time is 10 s, ensuring that such secondary gradients vanish. However, with a channel height of 100 µm, the diffusion time exceeds the convection time. In these cases, after a given time, molecules closer to the wall will have diffused farther than those closer to the channel center. Due to the shape of the diffusion profile, this was termed “the butterfly effect” by Kamholz et al. [71]. The effect complicates matters substantially, and others have resorted to full, three-dimensional numerical solution of the diffusion-convection equation (6.1) in such cases [39]. As the devices employed here have a length on the centimeter-scale, which must be finely meshed, simulation convergence was difficult to obtain. Instead, a Monte Carlo simulation was written in MATLAB 2016b (The Mathworks, Natick, MA, USA), which “flips a coin” to determine whether z-axis diffusion moves the molecule towards or away from the channel center, then moves it a distance dz as determined by the time step dt. At the same time, the molecule is moved a distance dy as determined by the y-axis velocity $v_y(z)$ at that time step. This is illustrated in figure 6.5. Note that dy is much smaller when the molecule is closer to than wall than when it is closer to the channel center (compare points at $y \approx -140\,\mu\text{m}$

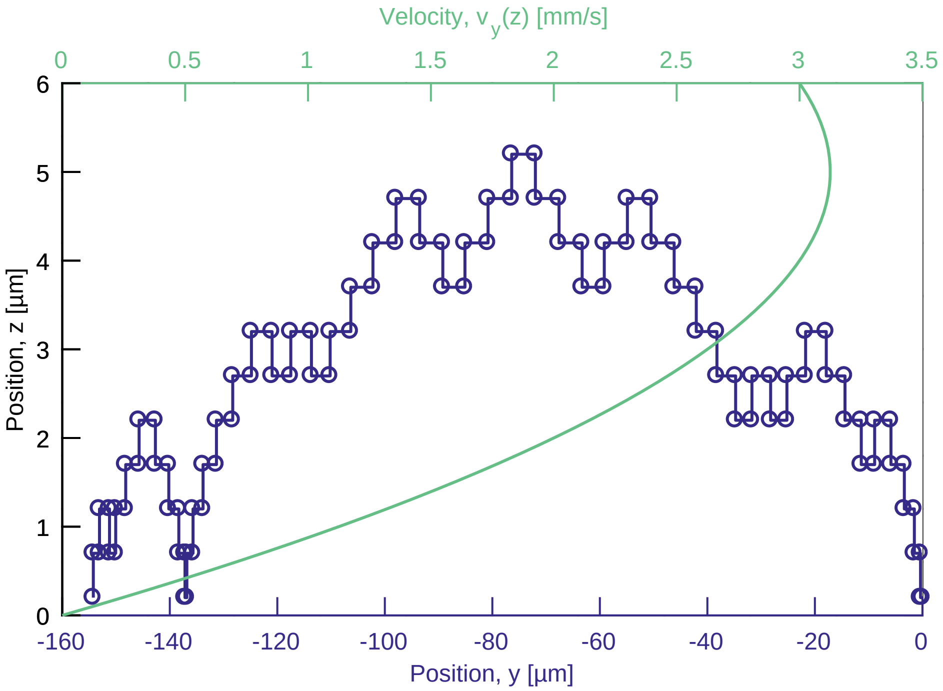

Figure 6.5. Sample from a Monte Carlo simulation of diffusion and convection in a 10 μm deep channel. When the molecule is closer to the wall ($z = 0$), the change in y-position is much smaller per time-step than closer to the channel center, due to the parabolic flow profile.

to points at $y \approx 80\,\mu$m). The measurement location is at $y = 0$, so the simulation is performed in reverse, to avoid the majority of possible trajectories, which would cause a molecule to end up outside the GMR mode interaction volume. When z-axis diffusion is sufficient, z-axis gradients will blur before the molecule is measured at $y = 0$, and the average flow velocity $\bar{v}_y$ is representative of the diffusion time. When measurements are taken close to the stagnation point, or if the molecule is large and slow-diffusing compared to the flow velocity, a z-axis diffusion time gradient will be present. Molecules that end up in the mode interaction volume are then more likely to have stayed near the wall longer, potentially increasing their diffusion time far beyond the average convection time.

As the channel depth is limited by the tape thickness, adhesion bonding cannot provide sufficiently shallow channels for the butterfly effect to be negligible. Instead, PDMS casting and UV photolithography was turned to.

6.1.1 Photolithography-defined devices

A custom chromium photomask was used with standard photolithography to define channels of width 500 µm to 2000 µm in SU-8. This resist is sufficiently hard and stable that it can be used as a casting mold directly, making etching unnecessary. In order to facilitate release, an FDTS coating was applied. A slab of PDMS was cast from the mold, inlet holes were de-

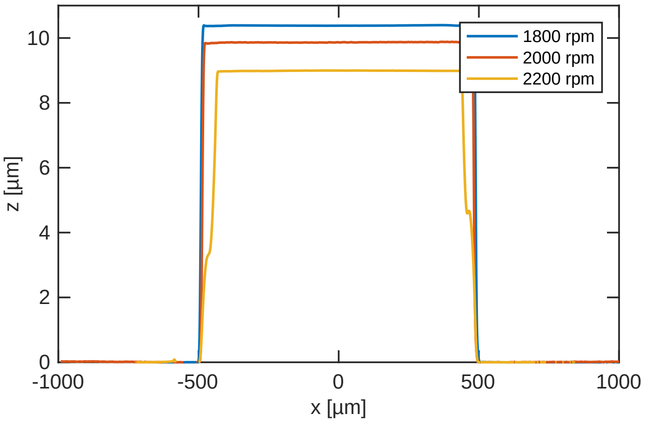

Figure 6.6. Profilometer characterization of H-filter stamp, after spincoating the polymer to a thickness of approx. 10 μm.

fined using a biopsy punch, and the system was integrated using plasma bonding.

The height of the silicon stamp for H-filter molding was measured by profilometry, as shown in figure 6.6. A spin speed of 2000 rpm leads to a device of dimensions very close to the specifications, namely 10 µm height and 1 mm width. Several designs were included on the same photomask, enabling channels of widths ranging from 0.5 mm to 2 mm. However, as PDMS is known to shrink upon curing, the bonded device was also characterized by mapping the interference pattern observed in the air-filled channel, as explained in section 6.1. This intereference is due to Fabry-Pérot interference. When the refractive index of the cavity medium (air) is known, the cavity length (channel height) is revealed by the wavelength-dependent interference period, known as the FSR.

6.1.2 Flow development

According to the no-slip boundary condition, the fluid velocity is zero at the wall. Where the two walls meet, the flow must therefore also be zero, and is referred to as the stagnation point [72]. Upon moving farther downstream, the flow develops until the parabolic flow profile has been established. The entrance length L_e describes the distance from the stagnation point, where the velocity has reached 99% of the fully developed velocity profile. For simplicity, measurements should be conducted downstream from L_e, which for a circular pipe (at least providing an order-of-magnitude estimate for a rectangular channel [71]) is expressed by

$$L_e = d(0.379\mathrm{e}^{-0.148Re} + 0.0550Re + 0.260) \tag{6.8}$$

where d is pipe diameter and Re is Reynold's number (equation 2.37). At 5 mbar, the Reynold's number is $Re = 0.0007$ (purely laminar), and using an equivalent pipe-diameter of $d = 2\sqrt{wh/\pi}$, the entry length is found to be merely $L_e = 46$µm, safely upstream from the measurement position at $y = 10$ mm.

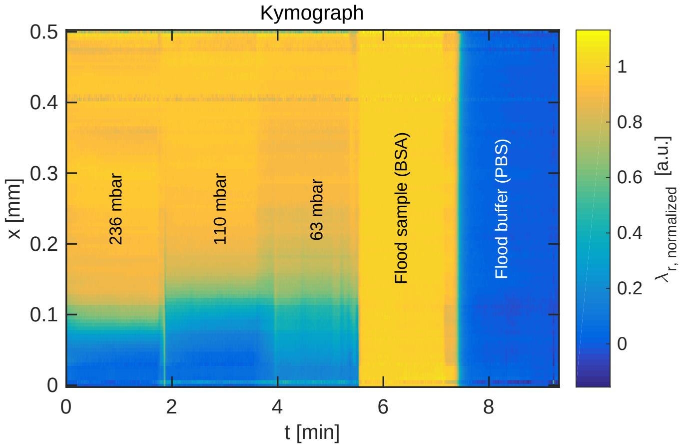

Figure 6.7. Kymograph of BSA diffusion experiment, obtained by end-to-end fusing the resonance wavelength distribution for each frame. The color corresponds to resonance wavelength shift normalized to the reference values in pure PBS buffer ($\lambda_r = 0$) and pure BSA ($\lambda_r = 1$). The sharpness of the transition increases with measured pressure.

6.1.3 Axial diffusion

Diffusion also occurs in the axial (y-axis) direction, often referred to as Taylor dispersion, which can influence the convection time. The extent of this effect has been the topic of some controversy [73, 74, 75], but when the axial diffusion length is much shorter than the total convection length, the effect can be neglected. Under proper conditions, only transverse diffusion in the x-direction thus becomes significant.

6.1.4 Diffusion length

The resonance wavelength distribution $\lambda_r(x)$ of each frame can be combined to form a kymograph displaying time on the first axis, as shown in Figure 6.7. It is evident that the RI boundary becomes sharper when the pressure difference increases, which decreases the time for diffusion and thus diffusion length. The figure also indicates the reference signals when the channel is entirely filled with sample or buffer, respectively. As the sharp boundaries on the temporal axis indicate, steady state is rapidly achieved. At the lowest flow rate shown here (Q =19.1 nL/s), the convection time is $t_{\text{conv}} = ywh/Q$ =9.15 s. Following a change in flow rate, a delay of $t > t_{\text{conv}}$ should thus be permitted to ensure steady state. By temporal averaging of the resonance wavelengths within each section, steady-state diffusion profiles are obtained for various flow rates, as shown for glucose and BSA in Figure 6.8. Theoretically, with these diffusion profiles, it should be possible to derive the diffusion coefficient of compounds diffusing in a sensor-embedded microfluidic H-filter.

6.2 Estimating diffusion coefficient

For determining D, a linear plot can be constructed (using a simplified hydraulic resistance R_{hyd}). When the flow rate Q is known (using syringe pumps), the convection time $t_{\text{conv,Q}}$ is

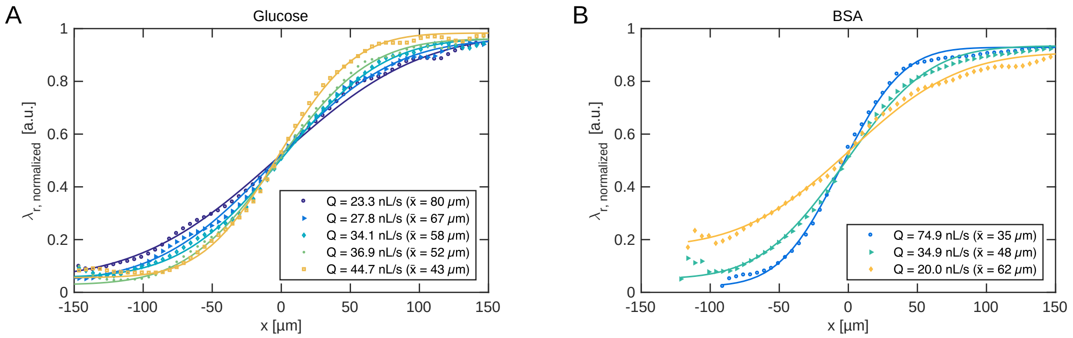

Figure 6.8. Experimental diffusion profiles for a) glucose and b) BSA. Higher flow rates (Q in the legends) lead to sharper transition (smaller $\bar{x}$) at a given downstream position. Solid lines indicate best fits to equation 2.51.

given by

$$t_{\text{conv}} = \frac{\Delta y}{v} \tag{6.9}$$

$$v = \frac{Q}{wh} \tag{6.10}$$

$$t_{\text{conv,Q}} = \frac{\Delta y w h}{Q} \tag{6.11}$$

$$\tag{6.12}$$

Alternatively, when Δp is known (using an electronic MFCS), the convection time $t_{\text{conv,p}}$ is estimated as

$$Q = \Delta p R_{\text{hyd}} \tag{6.13}$$

$$R_{\text{hyd}} = \frac{12\eta L}{h^3 w} \Rightarrow \tag{6.14}$$

$$t_{\text{conv,p}} = \frac{\Delta y w h}{\Delta p R_{\text{hyd}}} = \frac{\Delta y w h 12\eta L}{\Delta p h^3 w} = \frac{\Delta y}{\Delta p}\frac{L}{h^2}12\eta \tag{6.15}$$

The expression of hydraulic resistance is quite complicated, but can be simplified with a minimum loss of precision. For the channel geometry in question, i.e., $h = 9.15$ μm, $w = 1$ mm, $L = 20$ mm, the parallel-plate approximation gives an error of 0.58%, whereas shallow-channel approximation gives an error of 2 ppm. Then, the diffusion time is

$$\bar{x} = \sqrt{2Dt_{\text{diff}}} \tag{6.16}$$

$$D = \frac{k_B T}{6\pi\eta r} \tag{6.17}$$

$$t_{\text{diff}} = \frac{\bar{x}^2}{2D} = \frac{3\pi}{k_B T}\bar{x}^2\eta r \tag{6.18}$$

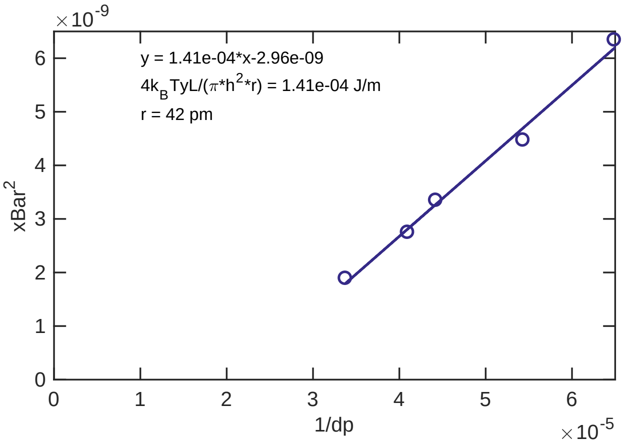

Figure 6.9. Diffusion fitting. Fitted slope when using equation 6.15 to describe diffusion time. Agrees reasonably well with linear interpolation, but does not intersect at zero.

Combining equations 6.15 and 6.18 yields a viscosity-independent expression:

$$t_{\mathrm{conv}} = t_{\mathrm{diff}} \tag{6.19}$$

$$\frac{\Delta y}{\Delta p}\frac{L}{h^2}12\eta = \frac{3\pi}{k_B T}\bar{x}^2\eta r \tag{6.20}$$

$$\bar{x}^2 = \frac{4k_B T}{\pi}\frac{\Delta y L}{h^2 r_{\mathrm{hyd}}}\frac{1}{\Delta p} \tag{6.21}$$

Thus, plotting the measured diffusion length $\bar{x}$ against the inverse pressure gradient $1/\Delta p$ yields a slope which depends on the geometric parameters of the channel, which are known, and the unknown hydrodynamic radius r_{hyd}. Alternatively, 6.21 can be plotted as $\bar{x}$ against everything on the right-hand side except $1/r$, which will then be the slope. However, as figure 6.9 shows, the data appears reasonably linear for the pressure interval investigated, however, equation 6.21 predicts as linear fit *with zero intersection*, which is clearly not the case here. Assuming the model to be correct, the only way for the data to end on a line with zero-intersection, is for a constant offset to be present in either Δp or $\bar{x}$. Changing any of the geometric factors, such as height, only affects the slope. The diffusion length is a result of fitting, and it is difficult to imagine why a constant offset would be present there. If the spatial coordinates were off, or if the hydraulic resistance approximation was poor, this would all lead to a multiplication factor rather than a constant offset. One possibility is that a pressure leak is present, e.g., due to parasitic flow, such that a constant pressure error is affecting all readings. Diffusion time is more than sufficient to blur out any z-axis gradients, so it is unclear why the model should be erroneous.

Looking instead at a situation where the pressure is unknown, but the flow rate Q is mea-

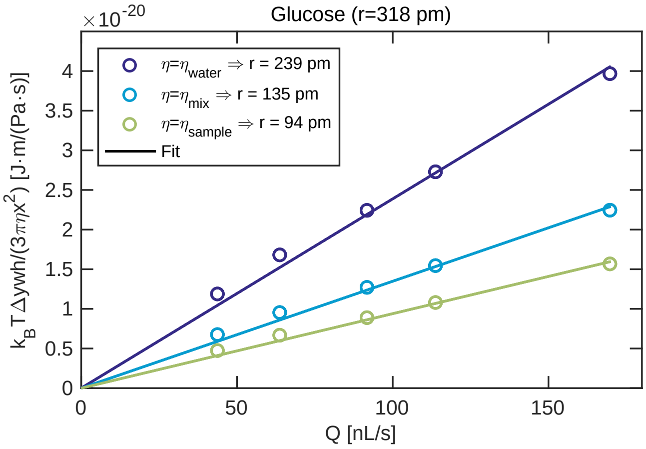

Figure 6.10. Diffusion fitting to measured flow rate. Fitting instead to measured flow rate via equation 6.24 reveals fits with zero intersection, although neither option for viscosity yields a sufficient hydrodynamic radius.

sured directly, allows for a combination of equations 6.23 and 6.18 to yield

$$t_{\text{conv,Q}} = t_{\text{diff}} \tag{6.22}$$

$$\frac{\Delta y w h}{Q} = \frac{3\pi}{k_B T}\bar{x}^2 \eta r_{\text{hyd}} \tag{6.23}$$

$$r_{\text{hyd}} \cdot Q = \frac{k_B T \Delta y w h}{3\pi\eta\bar{x}^2} \tag{6.24}$$

One disadvantage is that η is uncertain. Plotting Q against the right-hand side of equation 6.24, directly reveals hydrodynamic radius r as the slope. Using the extreme values of pure water $\eta = \eta_{\text{water}}$, glucose solution $\eta = \eta_{\text{glucose}}$, or an average between the two, $\eta = \eta_{\text{mix}}$, yields widely different results. At high concentration, the viscosity is expected to depend on spatial coordinate, $\eta = \eta(x)$, which the model may not take into account.

This representation fits reasonably well with a zero-intersection linear curve. However, even for the lowest viscosity (η_{water}), the hydrodynamic radius is underestimated by 25%. This might be explained by the geometrical parameters (Δy, w, h) being overestimated. It is unlikely that either of these are off by 25%, and the height was verified by two complementary methods, but if two of the parameters width/height/y-coordinate are both underestimated, they need only be underestimated by 5% each. The y-coordinate was measured using the stage controller, which has micrometer precision. As $\Delta y = 19.1$ mm, even a modest 5% variation would still mean that the controller was off by 1 mm, which is unlikely. The width of the channel stamp was measured by profilometry, but a 5% shrinking after casting cannot be ruled out [76]. However, a 25% variation seems unlikely. Alternatively, the flow rate could be systematically overestimated by 25%. In practice, flow rates were adjusted such that the interdiffusion zone was approximately in the center of the channel, and the measured flow rates were not identical. This is to be expected for two liquids with different viscosity. However, it was uncertain that the flow rate of the high-viscosity sample was reliable, as the heat capacity of the 2 molal glucose solution is 15% lower than that of water [77], which the flowmeters were calibrated to. The concrete influence on the measured flow rate depends on the physical model employed internally by Fluigent, which is unknown. Thus, the total flow rate was assumed to be twice that of the water flow rate, and it is in principle possible that this could provide a 25% reduction in total flow rate. An alternative explanation is that it may relate to the coupling between the optical and fluidic aspects of the device.

6.3 Optofluidic coupling

Possible consequences of the sensor sensitivity decaying exponentially from the surface should be considered. The evanescent decay length describes the distance from the surface, at which sensitivity has reduced to $1/e$, is given by

$$\hat{e} = 1/\sqrt{\beta^2 - n_1^2 \cdot k_0^2} \tag{6.25}$$

where β is the mode propagation constant, n_1 is the superstrate refractive index and k_0 is the vacuum wavenumber. Thus, with a grating period of $\Lambda = 368$ nm and resonance wavelength of $\lambda_r = 550$ nm, the evanescent decay length is $\hat{e} = 130$ nm, At a distance z from the surface, the sensitivity s is thus simply

$$s = e^{-z/\hat{e}} \tag{6.26}$$

i.e., the 95% of the sensitivity will be within the first 388 nm from the surface.

Due to the parabolic flow profile characteristic of pressure-driven flow, for an inifinite parallel-plate channel (justified by the low aspect ratio of the channel of $h/w = 10/400$), the axial flow velocity $v_y(z)$ is given by[51]

$$v_y(z) = \frac{\Delta p}{2\eta L}(h-z)z \tag{6.27}$$

$$\tag{6.28}$$

Thus, the velocity goes towards zero at the wall, in accordance with the no-slip boundary condition. However, this potentially complicates matters, as liquid closer to the wall moves slower, allowing its contents more time to diffuse. Furthermore, as only the fluid lamellae closest to the sensor are measured, molecular diffusion might erroneously be overestimated. To account for this, a sensitivity-weighted velocity ζ might be employed, calculated as the product of the evanescent decay length (equation 6.26 (p. 67)) and the parabolic flow profile (equation 6.27 (p. 67)), which for small z is well-approximated by a linear polynomial $v_y(z) = az$:

$$\zeta = e^{-z/\hat{e}} \cdot az \tag{6.29}$$

$$\frac{d\zeta}{dz} = \frac{ae^{-z/\hat{e}}(\hat{e}-z)}{\hat{e}} = 0 \Leftrightarrow \tag{6.30}$$

$$ae^{-z/\hat{e}}z = \frac{a}{\hat{e}}e^{-z/\hat{e}} \Leftrightarrow \tag{6.31}$$

$$z = \frac{1}{\hat{e}} \tag{6.32}$$

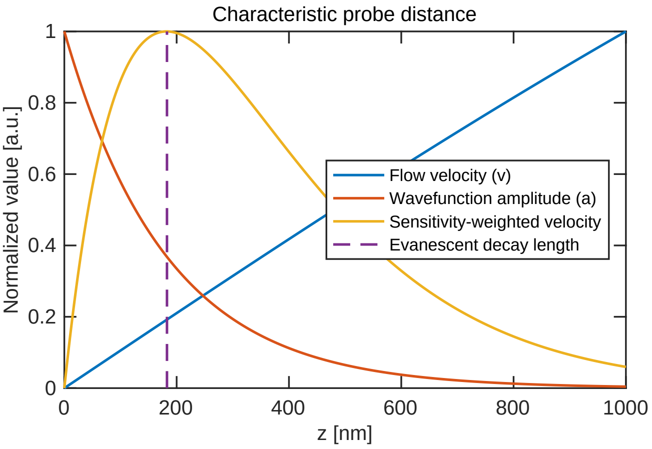

Figure 6.11. The electrical field amplitude of the sensor decays exponentially from the surface, probing a volume of liquid which consists of lamellae of varying concentration, due to the parabolic flow profile (which appears linear near the wall). The product of the field amplitude and the velocity has a maximum at the evanescent decay length, regardless of the absolute value of the flow velocity. This is considered the characteristic probe distance, as contributions from the higher-concentration region closer to the sensor are counterbalanced by contributions from the lower-concentration region further from the sensor.

Thus, as show in figure 6.11, the maximum of the sensitivity-weighted velocity will always be at $z = 1/\hat{e}$ regardless of the flow parameters.

Close to the wall ($z < 1/\hat{e}$) where the sensitivity is highest, flow velocity is small and convection time is large. Further from the wall ($z > 1/\hat{e}$), convection time reduces yet so does the sensitivity. Thus, in cases where a velocity-dependent concentration gradient exists in the z-direction, the characteristic position $\hat{z} = 1/\hat{e}$ will describe the concentration in the fluid lamella at that position. In practical terms, the convection time should be calculated for that lamella and used in further analysis.

However, a more practical solution is to simply operate the H-filter at a sufficiently small flow rate relative to the rate of diffusion, as described by the Péclet number:

$$Pe = \frac{\bar{v}h}{D} = \frac{Q}{wD} \tag{6.33}$$

Molecules are equilibrated across the height of the channel when $z/h \gg Pe \gg 1$,[78] erasing any gradients that would otherwise arise from the parabolic flow profile. It should be noted, however, that as the Péclet number becomes small, diffusive transport starts to influence the average axial velocity v_y. At the optimum parameters stated above (Q = 1.33 nL/s, w = 400 μm, D = 5.7·10^{-10} m^2/s), y_0/h = 1000, Pe = 5.8, so under these conditions, near-field effects are decoupled from the microfluidic flow conditions.

6.3.1 Viscosity estimation

Kamholz et al. argue [71] that the channel fractions χ taken up by water and sample, are equal to the ratio between the viscosities η, i.e., $\frac{\chi_1}{\chi_2} = \frac{\eta_1}{\eta_2}$. Assuming the channel fractions taken up by each liquid is proportional to the flow rates of each stream:

$$\frac{Q_1}{Q_2} = \frac{\eta_1}{\eta_2} \tag{6.34}$$

$$Q = Q_1 + Q_2 \tag{6.35}$$

$$Q_{\text{simplified}} = 2Q_1 \tag{6.36}$$

$$Q_{\text{actual}} = Q_1\left(1 + \frac{\eta_2}{\eta_1}\right) \tag{6.37}$$

$$\frac{Q_{\text{actual}}}{Q_{\text{simplified}}} = \frac{\eta_2}{2\eta_1} + \frac{1}{2} \tag{6.38}$$

With the viscosity of 2 molal glucose $\eta_2 = 2.54\eta_1$, that corresponds to an underestimation of flow rate by 56%.

6.4 Optimal performance

Optimal experimental design for determination of diffusivity was carried out by Häusler *et al.* in 2012,[39] and it was found that for highest performance, experiments should be carried out at contact times several orders of magnitude larger than those commonly employed in literature. In order to make universal recommendations, the Fourier modulus F_0 is used to represent dimensionless time:

$$F_0 \equiv \frac{tD}{(w/2)^2} \tag{6.39}$$

where t is time, D is diffusion coefficient and w is the channel width.

They found that the optimum performance is achieved at $F_{0,\text{opt}}$

$$F_{0,\text{opt}} = 0.299\left(\frac{h}{w}\right)^{-0.0983} \tag{6.40}$$

Thus, for the geometric parameters employed here (width w = w =1000 µm, height h =10 µm, equation 6.40 yields $F_{0,\text{opt}} = 0.47$. According to equation 6.39, for a relatively small molecule such as glucose of diffusivity D = $6.62{\cdot}10^{-10}$ m^2/s, the optimal contact time is $t_{\text{opt}} = 30.2$ s. Häusler et al. rightfully note that the optimal parameters depend on the unknown parameter being measured, namely diffusivity, but for as an initial estimate, theoretical models (such as the Wilke-Chang equation [79]) are available. When measurements are performed at $y_0 = 10$ mm downstream from the stagnation point, the optimum average flow velocity is $\bar{v}_{\text{opt}} = y_0/t_{\text{opt}} = 332$ μm/s, achieved with a volumetric flow rate of $Q_{\text{opt}} = v_{\text{opt}}wh = 1.33$ nL/s. The pressure necessary to drive a flow rate Q through a rectangular channel of length L is

$$\Delta p = Q\frac{12\eta L}{(1-0.63(h/w))(h^3w)} \tag{6.41}$$

For a channel of length L = 13 mm, the optimum pressure difference becomes Δp_{opt} = 5.26 mbar. This is realistic using the equipment available, but for much larger compounds such as the protein BSA, the optimum pressure gradient is less than 1 mbar, which will be unstable in practice. In such cases, a longer or narrower channel would be necessary to measure with optimum parameters.

Whereas H-filter flow conditions are traditionally chosen such that the diffusion front never interacts with the side walls, the optimum design exploits the observation that Fisher information increases significantly at the walls. However, this complicates analysis as the simple solution (equation 2.51) describing the diffusion front is no longer appropriate, as it assumes no wall interactions. Instead, data must be compared to full, three-dimensional numerical simulations and the parameters (chiefly diffusivity) of the most fitting simulation is taken as a result.

6.4.1 Steric hindrance

It is known that diffusion is hindered near the walls of a channel due to hydrodynamic drag[80]. The effect is more pronounced for larger colloidal particles, but as accounted for in section 6.3 the analyte concentration is only probed very close to the wall. Hindered diffusion within this probe volume would lead to an erroneously low diffusion coefficient.

The diffusion coefficient orthogonal to a wall $D_\perp$ relative to the bulk diffusion coefficient D_∞ is given by

$$\frac{D_\perp}{D_\infty} = \frac{6h^2 + 2rh}{6h^2 + 9rh + 2r^2} \tag{6.42}$$

where r is radius and h is the spacing between the wall and particle surface. The hydrodynamic radius r of a compound with mass diffusivity D is given by the Stokes-Einstein relation (equation 2.41). As an example, the hydrodynamic radius of the protein BSA ($D = 5.9 \cdot 10^{-11}$ m^2/s) is $r = 3.6$ nm. The effect of diffusion hindrance orthogonal to the wall is illustrated in figure 6.12. The diffusion coefficient is reduced to less than 80% of the bulk diffusivity within the first 20 nm from the surface. However, as the sensor sensitivity is also maximal in this region, its influence might be non-negligible. The impact of wall-hindrance on measured diffusivity can be estimated as the weighted average of the product of sensitivity and diffusivity ratio $\chi = sD_\perp/D_\infty$. This characteristic distance describes the diffusivity ratio as effectively measured by the sensor. For BSA, this leads to a 2.9% underestimation of diffusivity due to hydrodynamic drag, which is reduced to 0.3% for glucose, but especially for large biomolecules, this effect should not be casually neglected.

6.5 Droplet microfluidics

In order to monitor droplets in flow, a droplet generator was integrated with a PCS substrate. As figure 6.13 shows, the resonance wavelength periodically increases, representing the passing of a droplet containing 1 M glucose. The device is operated at a flow rate of $Q = 0.6$ µL/min. Despite the signal strength of the moving droplets being strong enough to tell when a droplet is present, it is insufficient to tell droplets apart based on their contents.

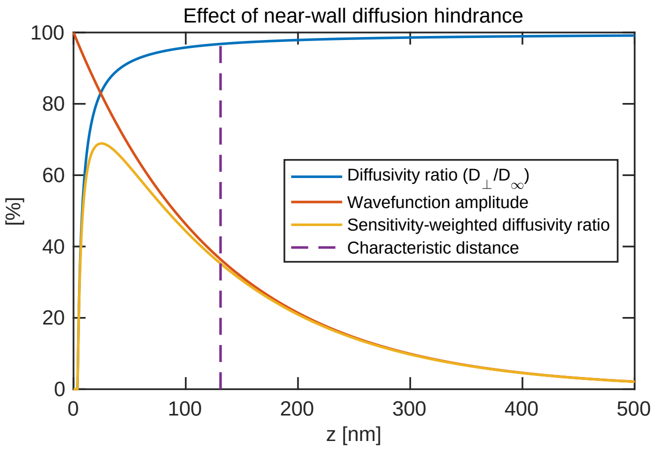

Figure 6.12. Diffusion hindrance near walls. Sensor sensitivity decays exponentially from the surface and thus has its maximum near the wall, which is where diffusion is most hindered due to hydrodynamic drag. The product of these two curves is the sensitivity-weighted diffusivity ratio, and the weighted average of this describes an effective diffusivity ratio as measured by the sensor. For BSA, the near-wall effect leads to an underestimation of diffusivity by 2.9%.

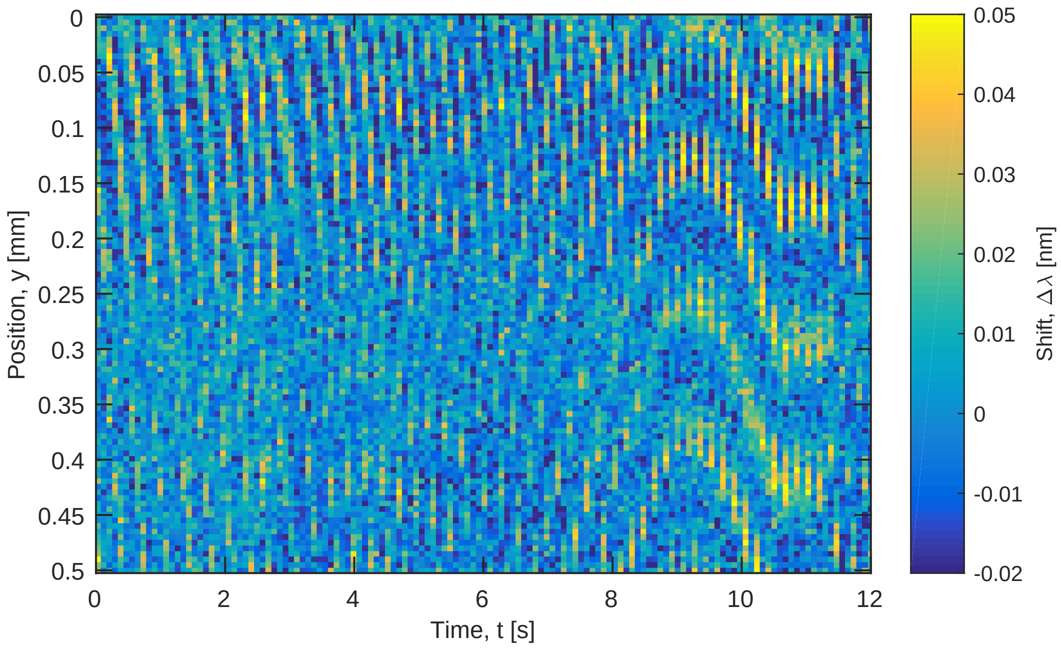

Figure 6.13. Droplets in microfluidic flow, as monitored by a PCS sensor.

Summary

In summary, H-filter devices have been demonstrated produced using rapid prototyping and adhesive bonding, and via photolithography and plasma bonding. Both types of sensor-integrated devices are capable of monitoring diffusion phenomena in a microfluidic channel, but due to adhesion bonded channels being rather deep, secondary concentration gradients arise, complicating data interpretation. Even with shallow, plasma-bonded channels, determination of diffusion constants proved challenging. A number of possible reasons for this were discussed, including the possibility of steric hindrance, optofluidic coupling, and viscosity-based non-linearity. It was found that the latter might explain the observed discrepancies.

Sensor-integration of a droplet generator was furthermore demonstrated. Although droplets in flow could clearly be observed, the signal-to-noise ratio (SNR) was found to be insufficient to distinguish the content of the droplets.

Chapter 7

Biological applications

BIOSENSING is a primary driver for PCS sensors, and they hold great promise for upgrading conventional biochemical methods into label-free counterparts. Biosensors based on GMR have been demonstrated in a plethora of embodiments, typically using antibodies, aptamers or molecularly imprinted polymers as biorecognition components. However, the ability to manipulate and confine light at the nanometer scale also has applications to imaging. Nazirizadeh et al. [18] demonstrated 3D-imaging of cells by monitoring the signal GMR intensity, and much work has been done in enhancing fluorescent microscopy by using a transparent PCS.

In this chapter, a couple of biologically relevant applications will be presented. First, protein quantification in whole-blood is demonstrated. Then, plant cells are imaged refractometrically. Finally, monitoring of release from drug-delivery carriers is discussed.

7.1 Protein quantification

Blood-gas analysis is crucial to healthcare. When red blood-cells rupture, a condition known as hemolysis, blood-gas analysis can be influenced. This makes robust detection of hemolysis desirable, in order to avoid administering unsuitable countermeasures. To investigate the ability of PCS sensors to measure in blood, a pilot study was conducted. Here, plasma, whole-blood, hemolyzed whole-blood and whole-blood spiked with sucrose or bovine serum albumin (BSA) were tested, as the time series in figure 7.1 shows.

7.2 Cell imaging

A topic of current research is the restructuring of the cytoskeleton within plant cells, and transport of vesicles along cytoskeletal filaments. It was hypothesized that a PCS sensor could monitor these phenomena when they occurred near the cell wall. With a platform for monitoring individual cells in a microfluidic channel, the cell environment could furthermore be modified and the cellular response monitored in real-time.

As these phenomena occur in any plant cell, a cell type was chosen which was harmless and easy to handle, namely cells from onions. Apart from these advantages, onion cells make for good model cells as they are representative of plants cells in general. They are also rela-

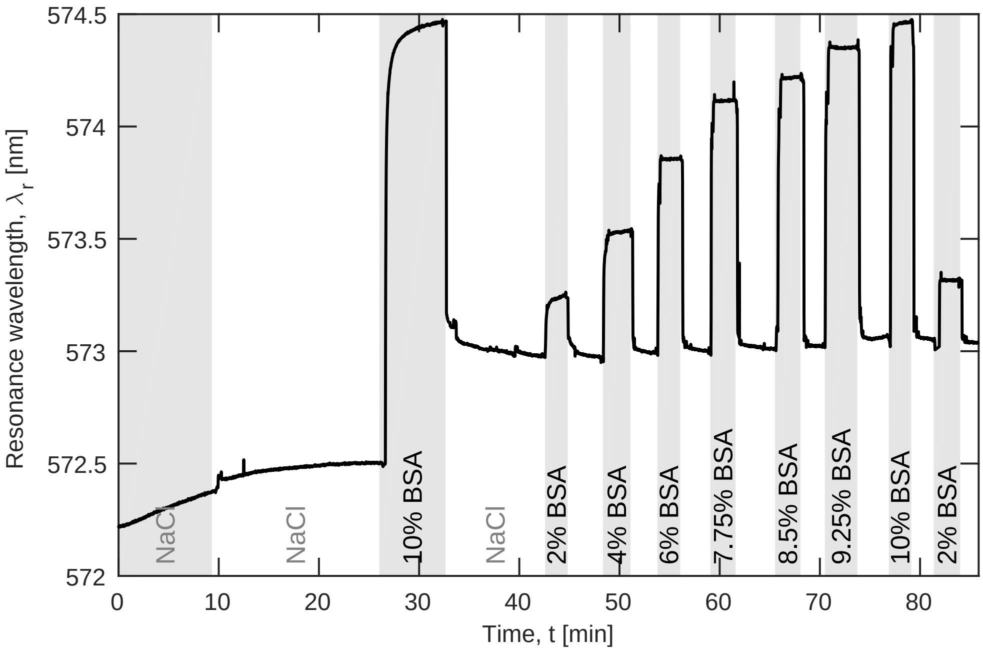

Figure 7.1. Sensorgram of measurements in protein-spiked whole-blood. Unlabelled periods represent NaCl-flushing.

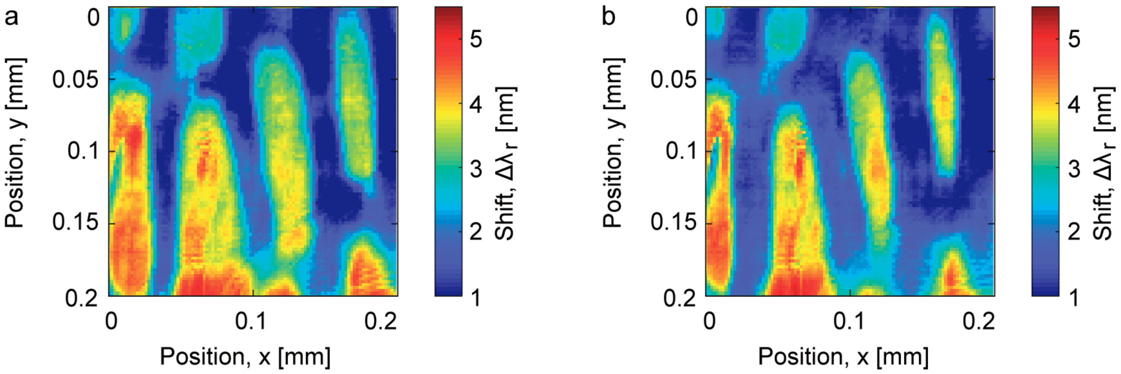

Figure 7.2. Refractometric image of onion cells in a microfluidic channel, a) before and b) after addition of sucrose. The cells appear to shrink, as expected from osmosis.

tively large, The thin membrane between onion layers consists of a single layer of cells, which is carefully extracted.

To keep the cells alive upon insertion into the microfluidic channel, neither ultrasonic, thermal nor plasma bonding were viable options. Instead, adhesion bonding was used, despite its limitation on channel height (≈100 µm). Possibly due to a water film between cells and the sensor surface, the cells are only visible when pressed down firmly against the surface. The sheet of cells must thus be cut to a dimension that allowed perfusion medium to still flow through the channel (having blocked the channel in the z-direction), and additional tape layers must be stacked to get a thickness exceeding the channel height, so that the cells are pressed down by the bonding process.

The sensors used in this project were titania-type, representing a nontrival cost in materials and time. Therefore, during the prototyping stage, the 16 sensors per wafer were lasercut into 9×9 mm^2 pieces. A square hole were then lasercut into blank slabs of PMMA, into which an isolated sensor would fit. Channels were defined by lasercutting a double-adhesive tape, and an injection molded COC-part was used to confine liquid and provide inlets.

As this study was conducted before writing the MATLAB mapping routines, an AutoHotKey script was written to move the motorized stage in small increments and acquire a spectrum at each position. Despite the crudity of the approach, it worked quite robustly.

As shown in figure 7.2, cells respond to changes in their environment, here by adding sucrose. As the cell wall is quite thick, it may be exceeding the sensor penetration depth of $\hat{e} = 138$ nm, in which case the observed structure arise from variations on the cell surface or within the wall, but probably not within the cell interior. By maintaining cells inside a microfluidic channel, it was possible to monitor changes arising from thanging environmental conditions such as osmotic pressure. It could also be used as a platform for investigating the effects of drugs on single cells, although that was outside the scope of the current project.

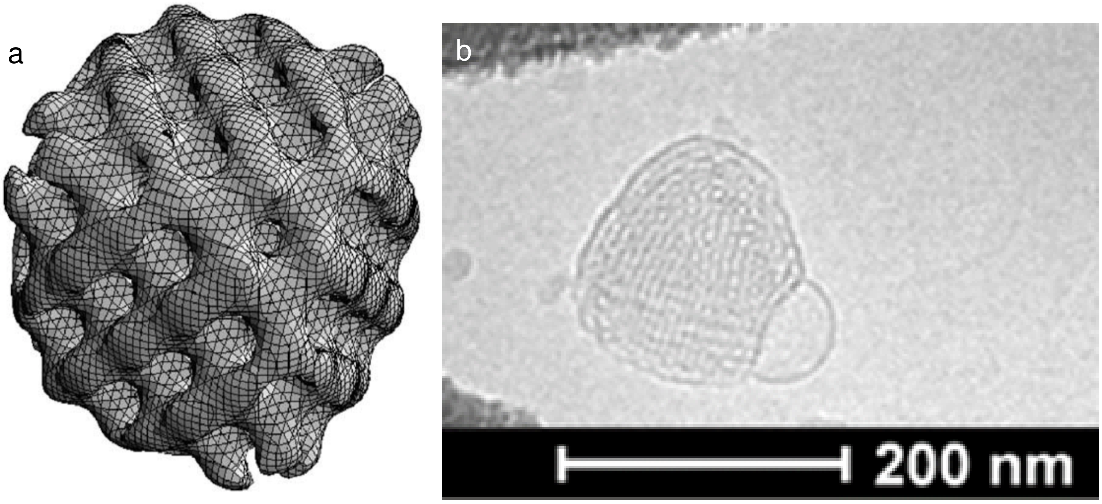

Figure 7.3. Cubosome structure a) shown schematically and b) imaged by TEM. From ref. [81] and ref. [82], respectively.

7.3 Drug delivery

Vaccines still remain a challenge in developing countries, however, due to the need for specific storage conditions and trained personnel to administer the intravenous inoculation. A possible solution to these issues is the development of oral vaccines The components necessary for vaccination can relatively easily be contained within a tablet, but as the gastrointestinal tract is highly specialized at decomposing such foreign entities, they would be destroyed before having an effect. Encapsulation of medicinal compounds for drug delivery is therefore an active research topic in general.

Drug delivery carriers range from stealth liposomes to cubosomes. These nanoparticles are dispersed pieces of cubosomal lipid structure, illustrated schematically in figure 7.3. They can be produced by spray drying of a cubosome precursor mixture, and upon hydration, the cubosomes will be loaded with the components of the precursor mixture. At the Center for Intelligent Drug Delivery and Sensing Using Microcontainers and Nanomechanics (IDUN) at the the Technical University of Denmark (DTU), cubosomes are furthermore packaged into microcontainers designed to releasing its cargo directly into the small intestine [3].

Modern vaccines work by presenting to the immune system harmless antigens, such as subunits from a pathogen protein. However, because these antigens are harmless, they elicit a limited immoresponse, making them ineffective on their own. So-called adjuvants play a pivotal role in this regard, as they fortify the immunoresponse. Recently, Quil A, a purified mixture of 21 different saponins has been discovered as a promising adjuvant. Antigens and adjuvants should be released together for optimal effect, and achieving optimally timed and synchronized release rates is currently an active topic of research. However, these endeavors are made challenging by Quil A's complex composition and spectral inactivity, making it

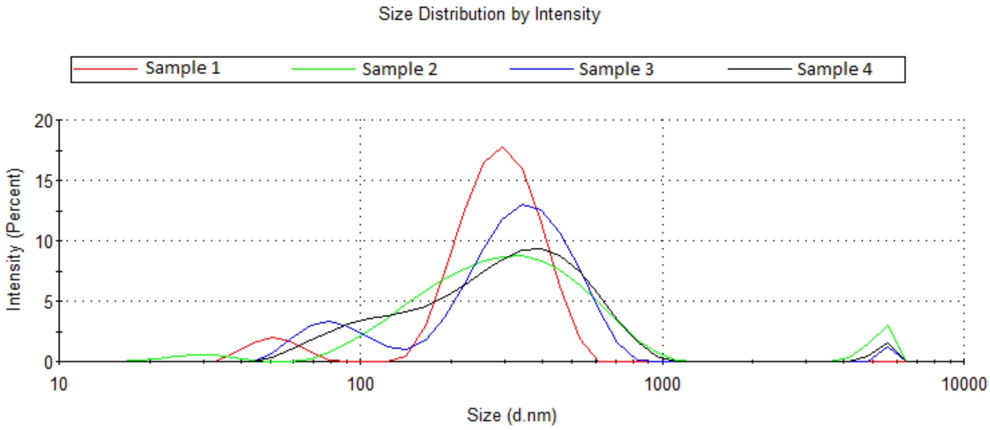

Figure 7.4. Size distribution of drug delivery carriers. On average, cubsomes were approx. 200 nm in diameter, safely exceeding the membrane pore size of 30 nm, excluding them from the sensor reservoir.

difficult to monitor release. Therefore, the possibility of using PCS sensors to this end was investigated.

7.3.1 Carrier isolation

A central problem in any release study is the isolation of released compounds from those still contained within the carriers. As the carriers are smaller than the system spatial resolution (as defined by the optics of the setup and the lateral mode confinement of the GMR), resonant wavelength shifts will depend on the average refractive index within the probe volume. Therefore, at the outset, it is impossible to distinguish between compounds that are encapsulated and those that are released. In order to distinguish, size exclusion can be employed. As a simple form of this, nanoporous filters were used to separate released compounds from the cubosomes. With an average pore diameter of 30 nm and an average cubosome diameter of 200 nm, as indicated by the dynamic light scattering (DLS) data in figure 7.4, this ensures that cubosomes remain in the upper compartment, whereas released compounds are able to diffuse through the membrane filter and reach the sensor probe volume.

7.3.2 Sensor calibration

In order to relate resonance wavelength shift with Quil A concentration, a calibration curve is required, as shown in figure 7.5. With the calibration curve in place, it is possible to calculate the Quil A concentration over time. However, for determining release kinetics, it is necessary to know how much was encapsulated within the cubosomes in the first place, i.e., determining the endpoint concentration corresponding to 100% release.

The time series shown in figure 7.6. Because the membrane filter cannot be in contact with the sensor, lest the sensor will merely be measuring the presence of the filter, the mem-

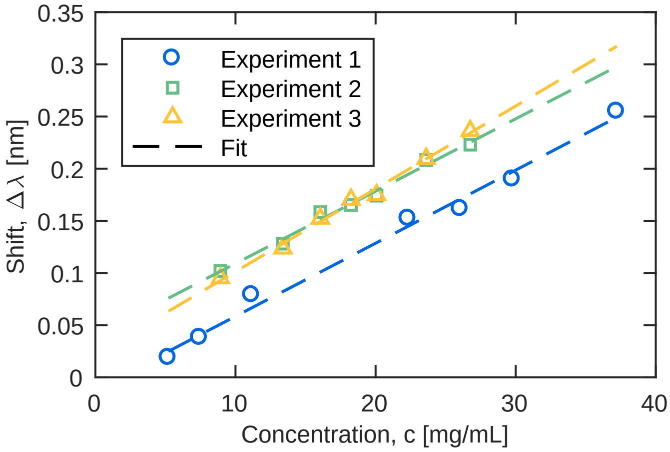

Figure 7.5. Calibration curve for Quil A adjuvant in the presence of dextran, enabling conversion from resonance wavelength shift to concentration. The mean slope is dλ/dc=(7.3±0.3) pm/(mg/mL).

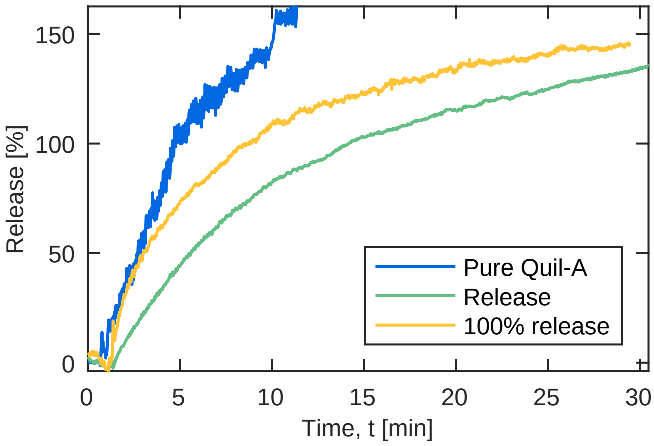

Figure 7.6. Quil A release curves.

brane separation increases the distance necessary for released compounds to diffuse. This causes a delay, and the measured time series will thus be a superposition of release and diffusion time.

Summary

In this chapter, three quite different biologically inspired applications were investigated. First, the ability to quantify bulk protein concentration in whole-blood was demonstrated. Then, a solution for isolating plant cells in a microfluidic channel was shown. This allows refractometric monitoring of cell response to compounds in the perfusion liquid. Finally, release of the complex adjuvant Quil-A from nanoparticle carriers was documented. As monitoring the release of spectrally inactive compounds from drug delivery systems is currently quite challenging, such a solution could be highly beneficial. In general, it is believed that easier quantification of non-absorbing and non-fluorescing species could have a broad market appeal, as is the topic of the following chapter.

Chapter 8

Commercialization

ALTHOUGH refractive index measurements have many advantages, they are rarely done in general chemical and biochemical laboratories. Because sugars are such an integral part of many consumer products, on the other hand, they are rather widespread in the food and beverage industries producing them. The prospect of label-free BIA and HTS are desirable to high-end research targets, such as drug discovery and microbiology, but the typical price tag often represents an insurmountable entry barrier outside the wealthiest fields.

This chapter reviews the current state-of-the-art commercial options for PCS sensing, and presents a novel solution that might bring PCS sensing to the masses.

8.1 Instruments

8.1.1 Refractometers

Refractometers come in many classes, from cheap, handheld, low-precision versions available at approx. 500 EUR, to multi-wavelength state-of-the-art refractometers, such as the Anton Paar Abbemat MW refractometer with a list price of almost 20 000 EUR[1]. These are all prism-based, i.e., the critical angle is translated into a refractive index, or, as the plurality of the market is interested in measuring sugar content, in units of degrees Brix.

Applications include[2], for example, quality control of icing inhibitor for jet fuel, additives for diesel fuel (AdBlue), sugar content in wine, dry solids in urine, milk, fruits, and honey, fatty acid concentrations in nuts and chocolate, and heavy water concentration control for nuclear power plants. This diversity is a testament to the universal nature of refractive index measurements, even for bulk measurements, without surface functionalization for specificity. Despite the universality of refractive index measurements, which could likely benefit most laboratories as a fundamental tool on par with a thermometer or an analytical balance, refractometers are mostly found in specialized laboratories. The limited adoption of the technique may in part be due to the fact that all samples are in contact with the same prism, risking cross-contamination. Regular cleaning and calibration is furthermore necessary. This takes time, and the costs of cleaning solution and high-precision calibration fluids add to the mainte-

---

[1] J. Petersen, Anton Paar (personal communication, November 9, 2015).

[2] according to Anton Paar application reports.

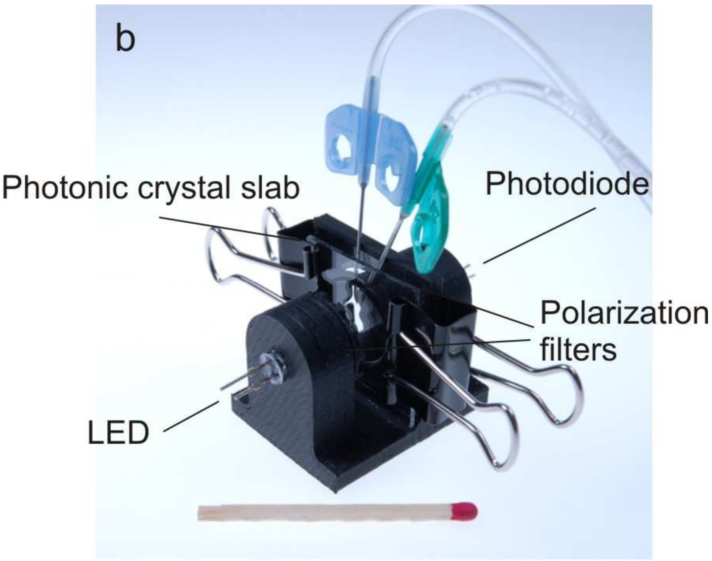

Figure 8.1. Highly compact PCS readout device. A photodiode measures the amount of light passing through a PCS sensor sandwiched between crossed polarizers, upon illumination from an LED. From ref. [83].

nance cost. This limitation could be alleviated by exchanging the transducer, from a prism to a PCS.

8.1.2 Photonic crystal readers

In order to read out the PCS sensor, specialized equipment is typically needed. Ultra-compact and cheap readout instruments based on diodes have been demonstrated in the literature, as shown in figure 8.1, and readout using a smartphone camera has also been demonstrated [84]. However, to the author's knowledge, such ultra-cheap readout solutions are not commercially available. A system that comes close in terms of compactness, and which is commercially available, is the elegant Lyte96 by Byosens GmbH (Hamburg, Germany). This compact microwell platereader has the same footprint as a microwell plate, and is designed to be able to go with the plate into an incubator, in order to monitor cell proliferation. The regular price is 20 000 EUR[3].

Another prominent option for reading of PCS sensors is the Epic® System by Corning® (Tewksbury, MA, USA), which can read a full microwell plate in 15 seconds. The readout system takes up approx. $1 \times 1 \times 2\ \mathrm{m}^3$ [85], and has a list price of approx. 100 000 EUR [4], putting it beyond reach for all but the most specialized and well-funded laboratories.

8.1.3 Designing a compact setup

The setup used in this work has a material cost of approx. 56 000 EUR, of which the imaging spectrometer makes up ≈80%. It has a footprint of approx. $1\ \mathrm{m}^2$. In an attempt to lower

---

[3] Y. Nazirizadeh, Byosens GmbH (personal communication, August 29, 2016.

[4] U. Vespermann, Corning (personal communication, February 24, 2017).

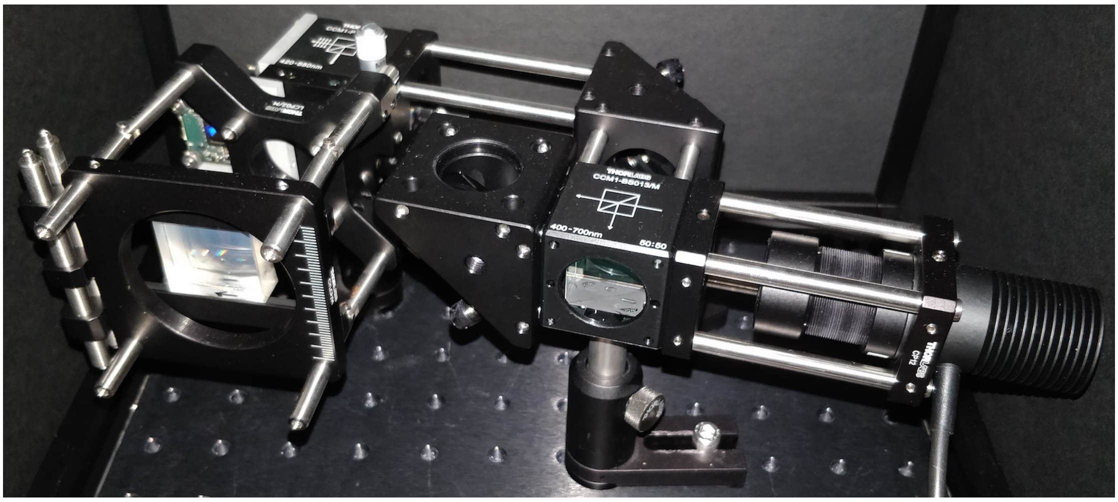

Figure 8.2. Photograph of compact setup, employing an LED light source and two CMOS cameras acting as a microscope and spectrometer, respectively. Microscope objective not shown.

the material cost and reduce the footprint, an integrated system was designed in collaboration with Per Jørgensen. The setup, photographed in figure 8.2 features many of the same optical components as the original setup, but replaces the costly imaging spectrometer by a concave grating and a complementary metal-oxide semiconductor (CMOS). This reduces the footprint to approx. 25×30 cm^2, and reduces the cost by replacing the imaging spectrometer by a cheap grating and a camera.

As a simple proof-of-concept, the resonance shift was measured upon addition of glucose to a droplet of water, as shown in figure 8.3.

8.2 Sensor

Corning also produces microwell plates with sensors embedded, marketed as Corning Epic Microplates. Multiple surface functionalization options are available, at a commercial list price ranging from ≈1200 EUR (non-functionalized, 96 wells), to ≈3100 EUR (streptavidin coated, 384 wells)[5]. Half of the area of each well is non-functionalized to allow self-referencing.

With the price-tags of equipment and consumables, most PCS platforms currently target high-end applications such as drug discovery, where the expenses can be justified. However, given the versatility of refractive index measurements, the technique could see much broader applications. Refractometers are common in the food and beverage industries, with many applications revolving around measuring carbohydrates. In many of these applications, a high cost of consumables is a deal-breaker, and the necessity of purchasing additional instruments may represent an insurmountable entry-barrier. However, given the versatility and widespread adoption of spectrophotometers, many locations already have one. A

---

[5] U. Vespermann, Corning (personal communication, July 28, 2016).

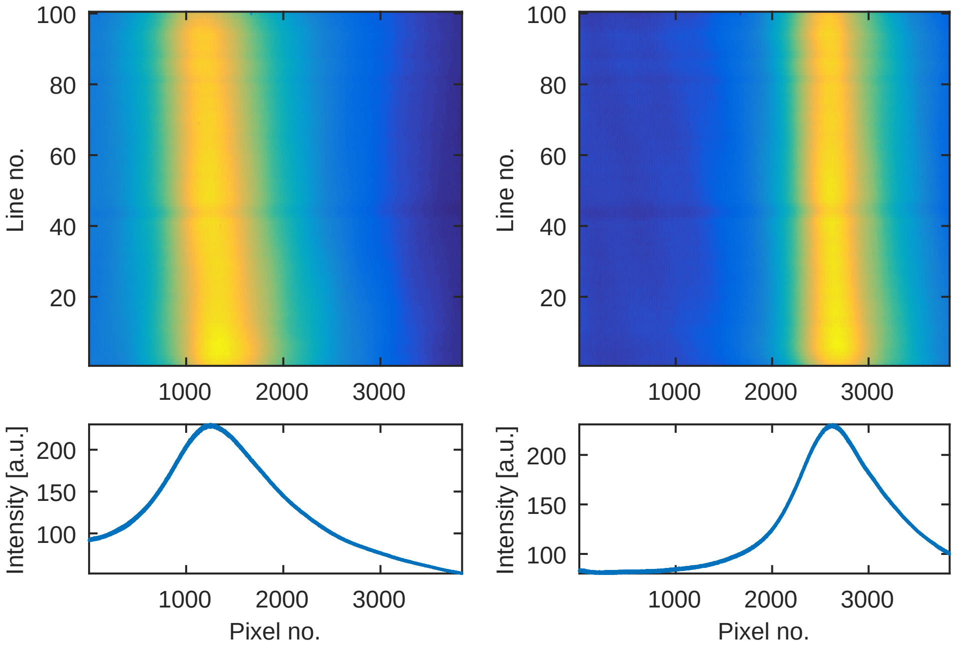

Figure 8.3. Calibration of compact setup. Addition of glucose causes a resonant shift. With a known concentration, units of pixels can thereby be calibrated to a meaningful concentration.

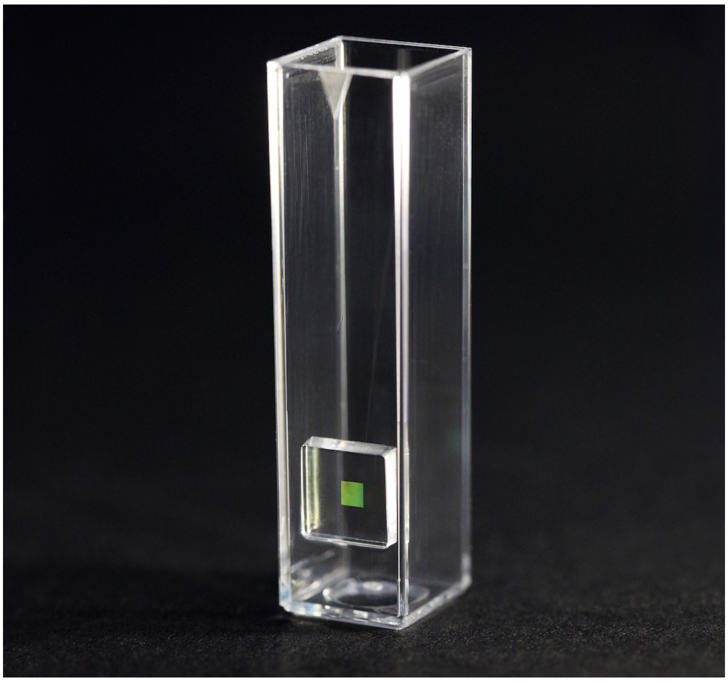

Figure 8.4. Photograph of early sensor-embedded cuvette. The presence of a PCS sensor allows a standard spectrophotometer to measure unperturbed absorbance in one orientation, and refractive index in the other orientation.

spectrophotometer accepts cuvettes, liquid containers of a standard size, and measures the absorbance A of an absorbing fluid. When the extinction coefficient α of the compound is known, the concentration c can trivially be found using the Lambert-Beer law:

$$c = \alpha l A \tag{8.1}$$

where l is the path length, standardized to 1.00 cm. However, when the compound of interest is non-absorbing, it cannot traditionally be quantified using a spectrophotometer. The user might then have to either purchase additional equipment, or send a sample to an off-site laboratory. This usually entails a 200 EUR cost and several days of delay. In the worst case, the answer might come back “the product was ready when you took the sample”, which might no longer be the case. Therefore, the ability to measure concentration of non-absorbing fluids using an existing spectrophotometer was proposed and patenteted in appendix D.

The spectrophotometer works by measuring to absorbance at various wavelengths. With the Lambert-Beer law, concentration is then related to the absorbance on the second-axis. By installing a PCS sensor in the light path of a spectrophotometer cuvette, concentration is now related to the resonance wavelength, i.e., on the first axis. As this is uncommon to laboratory technicians, and as the conversaion may not always be straight-forward, the second half of the product is the software, which automates the conversion via database lookups in a user-friendly manner, and is included for free. For common compounds, this database-lookup can make it unnecessary for the user to create calibration curves.

The first prototype PCS-embedded spectrophotometer cuvette was produced by laser-

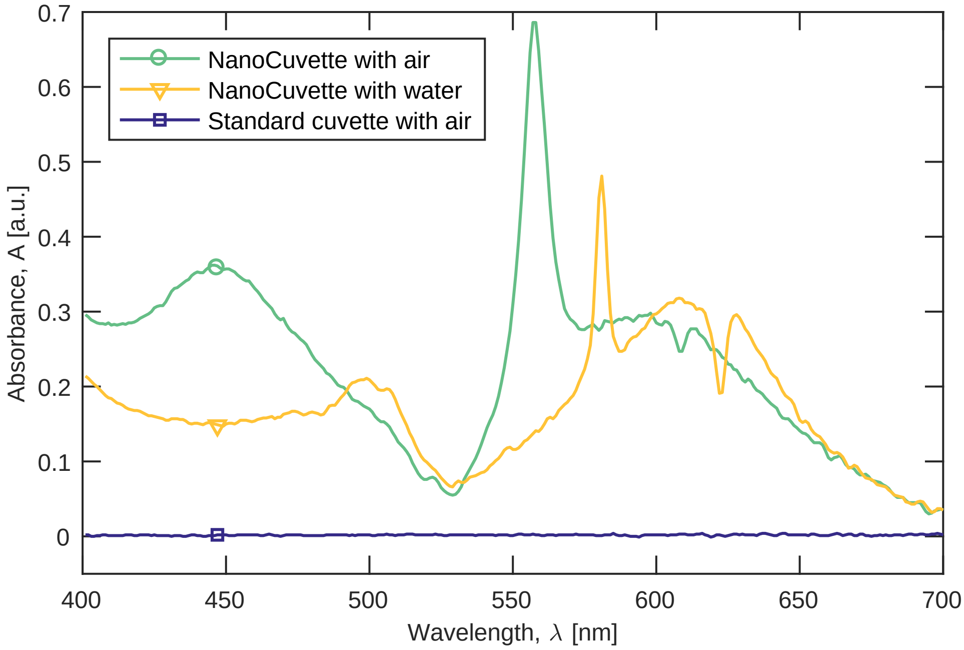

Figure 8.5. NanoCuvetteproof-of-concept. Adding water shifts the resonance wavelength when the cuvette contains a sensor.

cutting a titania-type PCS sensor and installing into a polystyrene cuvette using a pair of tweezers and adhesives. A resulting sensor-embedded cuvette is shown in figure 8.4. As a proof-of-concept, the resonance wavelength was read out using a Shimadzu UV-1800 spectrophotometer, as shown in figure 8.5. The resonance red-shifting is evident upon increasing the superstrate refractive index by adding water. As a comparison, the addition of water does not produce any peaks when using the same type of cuvette without a PCS sensor. Because the NanoCuvettedoes not contain a polarization filter, and no modifications are made to the spectrophotometer, both TE- and TM-polarizations will be present, as the multi-feature spectrum indicates. A polarization filter could be integrated in order to reduce resonance linewidth and increase SNR [20], but with an increased cost price.

Cuvettes with four optical sides enable orthogonal measurements, where in one orientation, the light does not interact with the sensor. Thus, absorbance in this orientation provides information about the imaginary part k of the complex refractive index $\tilde{n} = n + ik$. The resonance wavelength, obtained in the other cuvette orientation, then provides information about the real part, n. The ability of obtaining both of these aspects on the same sample, using standard equipment, is a unique feature of the NanoCuvette.

Especially when sensors can be made entirely out of polymers, they can be produced very cheaply. However, due to the waveguide core swelling issues outlined in section 5.5, the user would need to keep the cuvette submerged in liquid, lest the measurement delay could be on the order of hours. This also makes sample exchange problematic. However, when the sensor density is high enough, the cost for titania coating can be offset, and the retail price can remain on the order of 5 EUR. Initial market research indicated that this would be a reasonable price point. For samples that can easily be washed out, the cuvettes can be reused multiple times, further reducing the cost per measurement. For “sticky” samples, such as protein solutions, surface regeneration can be challenging. However, because a reference measurement can be made prior to adding the sample, a control can be made after washing to ensure sufficient cleanliness. When the cuvette is contaminated, the software can alert the user and recommend using a fresh cuvette.

For comparison, high-quality polymer cuvettes can be purchased for less than 1 EUR. These are useful for aqeuous solutions absorbing light in the visible spectrum. For organic solvents, that might dissolve the polymer, glass cuvettes can be used. For compounds absorbing light in the UV-region, such as proteins and nucleic acids, quartz cuvettes are commonly used. Although they are more costly (up to 1000 EUR), they can be reused many times, in practice until they are damaged mechanically. However, the cleaning protocol, involving boiling in acid, makes these measurements expensive in terms of work time. An example of this is bulk quantification of proteins, which is routinely done by measuring absorbance at 280 nm. As documented in section 7.1, the resonance wavelength shift reveals protein content. In some instances, the NanoCuvetteis expected to be a viable replacement, effectively shifting the signal into the visible spectrum, where polymers can be used. Then, after use, it can be discarded in order to avoid cross-contamination and cleaning. Because the extinction coefficient α depends on the amino acid composition, it varies widely from protein to protein. This makes it necessary to make a standard curve for the protein, and this can consume quite some time and sample, which may be costly. However, because the refractive index increment is relatively similar for all amino acids at dn/dc=0.190 mL/g±0.003 mL/g [86], refractive index is excellent for determining concentration regardless of amino acid composition. Furthermore, for shorter peptides, which might be devoid of spectrally active amino acids, quantification by absorption is not possible with a standard spectrophotometer. Custom peptides may be costly, but given the very small penetration depth of the sensor, submicroliter sample volumes could be supported.

Summary

To summarize, commercially available readout instruments were compared for cost and performance, and a compact imaging spectrometer setup tailored for PCS sensors was presented. Furthermore, the concept of embedding PCS sensors in standard spectrophotometer cuvettes was discussed, thereby alleviating an inherent limitation of spectrophotometers, namely their need of compounds to be absorbing. With the NanoCuvette, it is expected that users can get more value out of their existing laboratory infrastructure.

Chapter 9

Conclusion & outlook

In conclusion, PCS sensors have been investigated for a range of applications, with an emphasis on microfluidics integration. They can be fabricated entirely out of polymers, without cleanroom conditions and equipment, for a low-cost price per sensor. However, when submerged in water, waveguide core swelling was observed for this class of sensors. This makes them less suitable as free-standing sensors, but as the water exchange seems to stabilize after a few hours, they remain candidates for sensor-integrated microfluidics systems, which could be primed prior to packaging.

Simulations of the complicated interactions between light and nanostructures are often necessary for sensor design and readout interpretation. As resonant reflections are typically very narrow, simulations must have a high resolution to properly resolve them. For optimization of optical resonances in the visible spectrum, simulations must cover a wide wavelength interval. These "needle-in-a-haystack" type of simulations can benefit significantly by the simple scheme for adaptive resolution presented in this work.

Sensor-embedded microfluidics systems were used to investigate droplet generation, to image plant cells in microfluidic chambers, and to monitor diffusion of molecules in a microfluidic H-filter. Droplet microfluidics holds great promise for HTS, and by embedding a PCS sensor, the reactions in droplets could be detected without a change in absorbance or fluorescence. This could be highly beneficial to drug discovery, directed evolution and bioassays in general. Refractometric imaging of the DMR of cells also holds great potential, and is already the focus of much research and several commercialization efforts. Especially for meaningful imaging of plant cells, which have thick cell walls, reverse symmetry sensors are advantageous given their long penetration depth. Finally, diffusion monitoring has been demonstrated in sensor-embedded microfluidics systems. The diffusion length can be accurately obtained near the sensor surface by fitting the diffusion profile. However, the method was found to be less suitable for estimating diffusion coefficients, as the estimated diffusion time at the wall may be difficult to assess accurately. Furthermore, viscosity effects at high concentrations make interpretation of diffusion coefficient non-trivial. However, the ability to monitor diffusion length at any given point in a microfluidic network could still be beneficial in many cases.

Many applications of PCS sensors have been attempted during this project, and as is often the case in science, many alleys turn out to be blind, or at least much longer than anticipated. However, many of these attempts outline potential future directions, which could be pursued

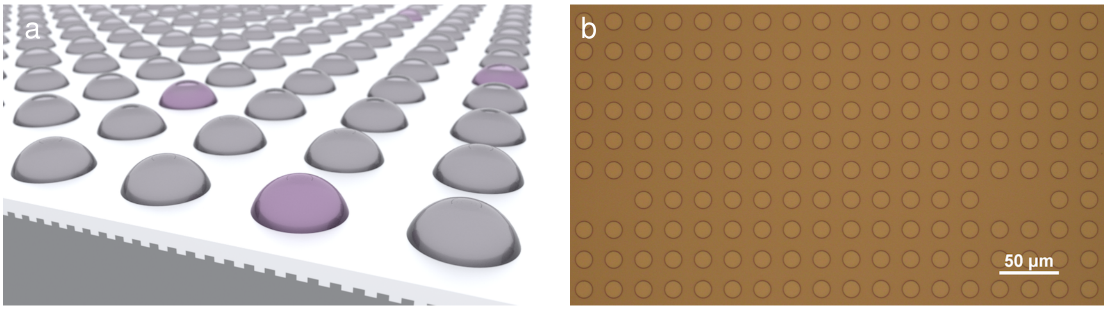

Figure 9.1. Droplet array for label-free investigation of single enzymes. a) Conceptual rendering, with purple droplets indicating the presence of a single enzyme. b) Micrograph of droplet array defined by photolithography, prior to development.

if more time was available. The perspectives of some of these pilot projects will be discussed here.

The materials constituting the sensors are of paramount importance to performance and possible applications. As an example, titania-based sensors have exceptional performance, except in alkaline solution or with significant UV-irradiation, which cause them to decompose over time. Given their need for vacuum-based deposition, they are also more expensive to produce than the wholly polymeric sensors investigated here. These, however, come with limitations in terms of waveguide core swelling, the unpredictable nature of which has likewise obstructed many projects in this work. PCS sensors are already being produced in a plethora of material compositions, as described in section 1.1. However, optimization of fabrication could still have a large potential. If sensors featuring polymeric waveguide cores could be coated to avoid water absorption, their application field could widen significantly. Other cheap, high-index polymers, such as polystyrene which has likewise been used in the literature, could also be investigated for core swelling in this regard. With precise thermal compensation, absorption of molecules other than water into the waveguide core could be investigated. Depending on the material, ions and molecules of a given charge might absorb more readily, perhaps aided by surfactants. As these compounds would access the waveguide core directly, where the field intensity is highest, this might enable extreme sensitivity for particular compound classes, and could perhaps be exploited for novel applications.

More resilient sensors, potentially suitable for long-term in-line operation for industrial production monitoring, could be developed, by etching the necessary nanostructures into a stable material such as glass and deposition of, e.g., chalcogenide glass. For subsequent microfabrication on a polymeric sensor substrate, e.g., in order to impart hydrophobic patterning for droplet arrays (fig 9.1a), an extensive compatibility study might be necessary in order to determine a material stack that is robust to the chemicals commonly contained in photoresists and their developers. With such a protocol, it might be possible to produce arrays of hydrophilic spots on an otherwise hydrophobic substrate (figure 9.1b). By flushing a plug of aqueous solution over the surface contained within a microfluidic channel, an array of microdroplets could self-assemble. Careful control of stoichiometry could ensure that micro-

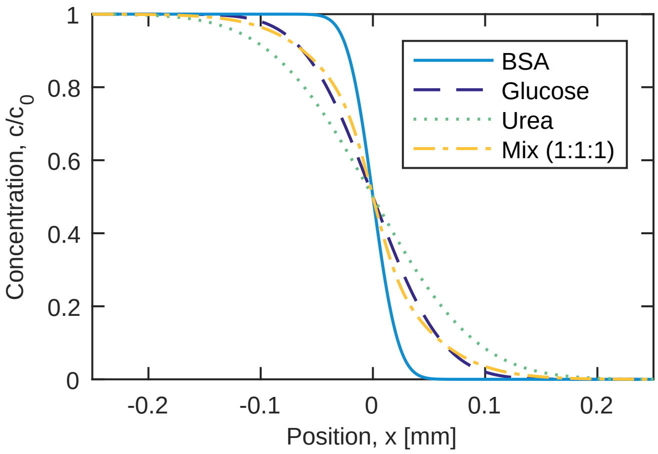

Figure 9.2. Calculated diffusion profile for a mixture of three compounds, and their individual pure profiles. The profile of the mixture appears to exhibit a unique shape.

droplets would contain at most one enzyme of interest, conceptually illustrated as the purple droplets in figure 9.1a. In this way, if an area corresponding to a well microplate was structured with a droplet diameter of 2 µm, it could contain approx. 1 billion individual droplets, each plate then corresponding to almost 500.000 large-capacity well microplates. With sufficient sensitivity, it might be possible to monitor single-enzyme kinetics with high throughput, with potential for directed evolution of improved enzymes.

The implementation of reference regions on the sensor as demonstrated also hold additional potential besides thermal compensation. State-of-the-art PCS sensors achieve detection limits on the order of 5×10^{-6} RIU. Even without the amplification of thermal influences documented section 5.4, this corresponds to a thermal detection limit of 0.05 °C. While such a solution could maybe not compete with the precision afforded by the isothermal titration calorimetry (ITC) and differential scanning calorimetry (DSC) techniques, it could still be useful in monitoring endothermic and exothermic chemical reactions on-chip.

A label-free investigation of release from drug deliveryarriers has been presented, using a nanoporous membrane to separate carrier from released contents. As such release studies could be relevant to a range of other systems, including nanogels and electrospun fibers, future work could focus on an improved separation mechanism. Early pilot experiments were performed with cast imprinting of a secondary, orhogonal grating on top of the PCS. It was verified by AFM that the secondary grating was thicker than the GMR penetration depth, with the purpose of shielding the probe volume from micrometer-sized carriers. Simulations revealed that the sensitivity should not be impeded from the secondary grating, and this was verified experimentally. However, possibly due to the secondary grating displacing the mode further into the superstrate, carriers were still detected. It is possible that the approach can be feasible, perhaps for larger carriers permitting larger periods on the secondary grating, and this could be investigated further. As an alternative, chemical modification of the sensor surface could be attempted. Similar to the extracellular matrix of cells, a polyethylene glycol (PEG) coating could form a matrix which is impermable to larger particles, but accessible to smaller molecules.

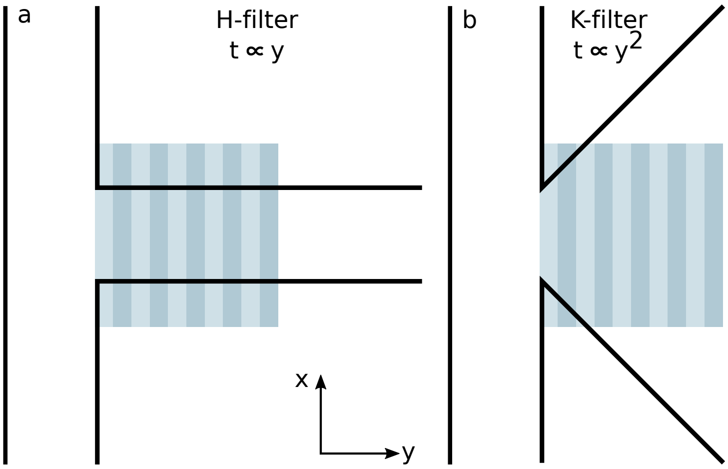

Figure 9.3. Proposed K-filter for simultaneous monitoring of multiple diffusion profiles. The striped square represents a multi-periodic grating placed partially within the channel. The profile at each period can be read out individually. a) In a traditional H-filter, diffusion time t is proportional to convection distance y. b) In the proposed K-filter, diffusion time scales with y^2, allowing downstream periods to sample much longer diffusion times.

In this work, sensor-integrated microfluidics H-filters have been extensively investigated. It was found that diffusion lengths could be monitored directly, by analyzing the diffusion profile as revealed by the spatially resolved resonance wavelength. Here, the focus has been on binary aqueous mixtures, but what would the diffusion profile look like for more complex mixtures? To this end, an analytical calculation was done by assuming a mixture to behave as a weighted sum of the individual diffusion profiles, i.e.,

$$c_{\text{mix}}(x,t) = \sum_{i}^{N} w_i c_i \tag{9.1}$$

$$c_i(x,t,D_i) = c_{0,i}\,\text{erfc}\left(\frac{x}{2\sqrt{D_i t}}\right) \tag{9.2}$$

where $c_i(x,t,D_i)$ is the concentration of the i'th component with diffusivity D_i at position x and time t, $c_{0,i}$ is the initial concentration of the i'th component, $c_{\text{mix}}(x,t)$ is the concentration of the mixture, N is the number of components in the mixture, and $w_i = m_i/m_{\text{total}}$ is the mass fractions of each component, constituting a mass m_i of the total mass m_{total}. The calculated mixed diffusion profile is shown in figure 9.2, and is seen to have a unique “diffusion fingerprint”. It may be difficult to assess individual concentrations from this, given that there are $2N$ unknowns, i.e., concentrations and diffusivities of the N components, and N itself might be unknown. If the system being monitored produces a change in the size of compounds in flow (e.g., nanoparticle/polymer synthesis/decomposition, anabolic/catabolic biochemical reactions), the shape might reveal the change qualitatively. Furthermore, if the course of the reaction is similar from cycle to cycle during production, calibration could reveal the stage of the process. In order to provide sufficient data for determining the $2N$ unknowns, a K-filter is proposed (named from its shape), as shown schematically in figure 9.3. By reading out a multi-periodic PCS sensor on an imaging spectrometer, with a cylindrical lens to capture multiple periods, each resonance wavelength corresponds to a given (x,y)-coordinate. In the schematic, the photonic crystal is shown with ten different grating periods, giving rise to ten diffusion profiles, at ten y-coordinates. In the case of a traditional H-filter, convection time (and therefore diffusion time) t is proportional to the y-coordinate. The diffusion profile sample at downstream grating periods will therefore be softer, revealing larger molecules, whereas upstream periods emphasize smaller molecules. However, as the permitted diffusion time scales linearly with space, this separation of diffusion lengths is limited in an H-filter. In the proposed K-filter, diffusion time scales quadratically with space, allowing much larger separation of diffusion profiles on a smaller area. With such an architecture, a unique diffusion fingerprint of complex mixtures could perhaps be obtained.

`asasim`: Adaptive Sampling for Electromagnetic Simulations

Kristian Tølbøl Sørensen[a,*]

[a] *DTU Nanotech, Technical University of Denmark, Ørsteds Plads building 345C, 2800 Kgs. Lyngby, Denmark.*

Abstract

For simulations of electromagnetic resonance spectra, where the locations of spectral features are unknown, and for wide-band simulations in general, a substantial number of wavelengths must be simulated for acceptable resolution, increasing computation time. This is exacerbated for spectra containing narrow-band features, as a high spectral resolution is required to even detect them. To address this challenge, a heuristic algorithm is presented for electromagnetic simulations, which adaptively refines the local resolution of spectral features during a simulation. The method supports parallel processing and plugs in with existing simulation systems, such as rigorous coupled-wave analysis (RCWA). It can routinely reduce the computational load by two orders of magnitude.

Keywords: lorentzian; cauchy; adaptive; resolution; multiscale; rcwa; dynamic

---

PROGRAM SUMMARY

Program Title: `asasim`
Licensing provisions: CC By 4.0
Programming language: MATLAB
Nature of problem: Simulations are challenging when information is needed both on a long scale (broad interval) and on a short scale (high local resolution), such as wide-band electromagnetic spectra containing narrow-band features. When resolution is insufficient, narrow-band features may be downright absent from the spectrum, if neighboring points fall on either side of a narrow peak. When local resolution is sufficient, it will necessarily be excessive in flat regions, wastefully increasing computation time.
Solution method: The presented method enables adaptive resolution, which ensures that all peaks of a given minimum width are always detected and maximally resolved, while

---

[*] Corresponding author.
E-mail address: kriss@nanotech.dtu.dk

Preprint submitted to Computer Physics Communications *2017-12-04*

feature-less regions remain minimally resolved. An optimum point spacing is derived for lorentzian peaks (descriptive of optical resonances) and is applied to optimize computation time.

Additional comments including Restrictions and Unusual features: None.

1. Introduction

The ability to accurately simulate light-matter interactions in nanostructures has enabled breakthroughs in areas as diverse as optical biosensors [1], pigment-free coloration [2], and solar cells [3]. Rigorous coupled-wave analysis (RCWA) is a popular semi-analytical method for electromagnetic simulations originally described by Moharam and Gaylord in 1981 [4]. However, the method is computationally demanding, and this can be a limitation for high-resolution, wide-band simulations. This can be particularly problematic for optimization methods, such as particle swarm optimization [5] or genetic algorithms [6], where an extensive number of simulations in a many-dimensional parameter space should be tested. Such endeavors would benefit from increased simulation efficiency.

The challenges of multiscale simulations have similarly been encountered in other fields, where more intricate schemes have been demonstrated, e.g., for elastodynamic shock propagation[7] or particle–particle interactions[8].

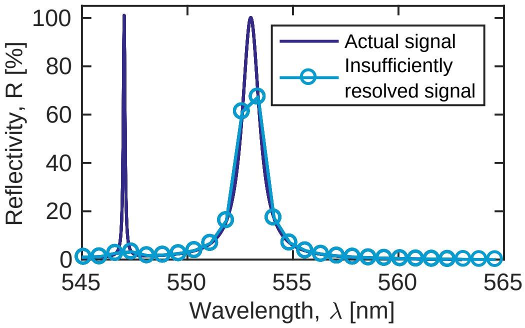

Figure 1: Illustration of detection problem. At insufficient resolution, the peak at 547 nm is not registered at all, as two neighboring points may randomly fall on either side of it. The much wider peak at 553 nm is certain to be detected at this resolution, but it is still poorly resolved.

Simulation time can be reduced by simply reducing the spectral resolution. However, when simulation resolution becomes too low, narrow peaks may not even be detected, as illustrated in figure 1. Depending on whether a data point happens to fall on the narrow peak, it may or may not register as a bump, but there will be a risk that the peak is completely absent from the simulation, which can be quite misleading.

As also illustrated in figure 1, peaks of sufficient width will surely be detected, as at least one point will always fall on the peak. However, resolution may still be too low to properly resolve its lineshape, which is commonly a simulation goal. An obvious solution is to increase the spectral resolution of the simulation, proportionally increasing simulation time, but this would result in an unnecessarily high resolution in the flat parts of the spectrum. Figure 2A illustrates this central issue, i.e., spectrally flat regions are over-emphasized, whereas regions with features are under-emphasized. Ideally, an initial simulation should only be fine-grained enough that the presence of a peak would always be detected, and peak regions should then be further resolved to the desired resolution.

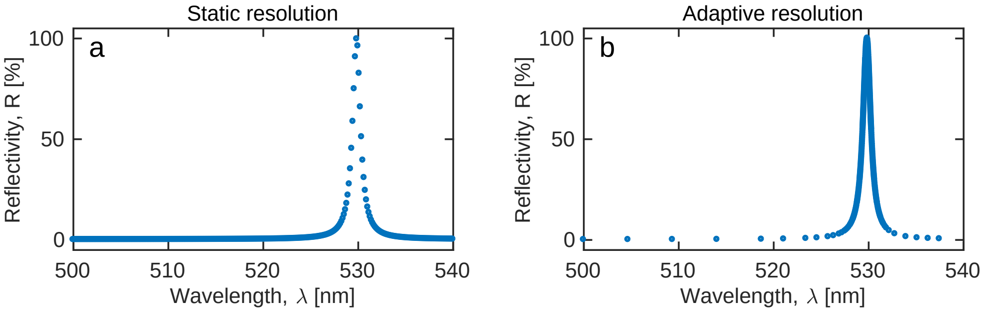

Figure 2: The same peak simulated with 309 points using a) static resolution, and b) adaptive resolution. The static method yields a high information density off-peak, whereas the adaptive method emphasizes the peak region.

Here, a heuristic MATLAB-algorithm is demonstrated for achieving adaptive resolution in electromagnetic simulations. This effectively reverses the information emphasis to lay on the spectral features rather than the background, as illustrated in figure 2B. Furthermore, optimal parameters are derived, and the speed of the method is evaluated.

2. Installation and examples

At its core, the `asasim` algorithm simply replaces the per-wavelength `for`-loop of a typical electromagnetic simulation system. Thus, instead of statically looping over all wavelengths in an interval with identical spacing, as is the common approach, `asasim` evaluates which regions to refine during runtime, i.e., regions where features

Listing 1: Original code

```
dx = 1;
x = 400:dx:700;
for ix = 1:numel(x)
y(ix) = simulateR(x(ix),input1,input2,input3);
end
plot(x,y);
```

Listing 2: asasim-implementation, illustrating how a wrapper-function may be defined.

```
minHalfWidth = 0.1;
dy = 0.01;
dx = optimalLorentzianSpacing(minHalfWidth,dy);
xInitial = 400:dx:700;
wrapFunction = @(x,S) simulateR(x,S.in1,S.in2,S.in3);
SimInput = struct('in1',input1,'in2',input2,'in3',input3);
[x,y] = asasim(xInitial,dy,wrapFunction,SimInput);
plot(x,y);
```

are present. Therefore, in principle, any script that calls a simulation function from a `for`-loop can be integrated with `asasim`. The system performs best for “needle-in-a-haystack”-type simulations, where narrow-band features are found in a broad interval. As this is common for electromagnetic resonance spectra, these are the focus of this paper, although the system will likely be applicable to many other topics of simulation as well. This section explains how `asasim` is integrated with existing simulation systems in MATLAB 2016b, running on a MacBook Pro (2.4 GHz Intel Core i5, 8 GB 1600 MHz DDR3 RAM).

The contents of `asasim.zip` should be decompressed to a folder on the MATLAB search path, such as `MATLAB/Toolboxes/asasim`. With the MATLAB-folder as the working directory, scripts should always contain the command `addpath(genpath(pwd))` in order to add all files in all subfolders to the search path. This line is included in all example files.

The main system for adaptive resolution is now installed, and is ready to be interfaced with an existing simulation system. In general, conversion of a simulation script (listing 1) into a version utilizing adaptive resolution (listing 2), is a three-step operation:

1. Define wrapper. Copy the contents of the per-wavelength `for`-loop into a wrapper function.
2. Determine initial point spacing. For peaks described as lorentzians ranging from 0 to 100% intensity, the optimal point spacing can be calculated auto-

matically using the `optimalLorentzianSpacing` function.

3. Replace the per-wavelength `for`-loop by a call to `asasim`.

Each of these steps will be elaborated next in the context of concrete application examples.

The purpose of the wrapper function is to bridge the simulation system with `asasim`, and must take two inputs, namely the simulation coordinate `x` (e.g., wavelength) and a struct of additional parameters. The wrapper function passes these parameters on to the simulation function(s), using the specific syntax of that simulation system. In general, the content of a per-wavelength `for`-loop can often just be excised and placed in a wrapper function, and the `for`-loop itself is then replaced by a call to `asasim`. This is first exemplified in a simple case here, where only a single hypothetical function `simulateR` is called from within the `for`-loop. Subsequent examples will handle more involved cases.

For simulations where the peak-shape resembles a lorentzian with a maximum intensity of 100%, the optimum initial point spacing `dx` can be calculated by calling `optimalLorentzianSpacing`, where `minHalfWidth` is the minimum lorentzian half-width to be detected, and `yRes` is the desired y-axis resolution. Using this point spacing, a vector of points to be calculated initially is then defined as `xInitial = x1:dx:x2`, where `x1` and `x2` represent the extremes of the interval to simulate. Alternatively, if the spectrum does not contain lorentzian peaks at 100% maximum, arbitrary values for `dy` and `xInitial` can be defined manually, using a custom point spacing `dx`.

2.1. A simple test

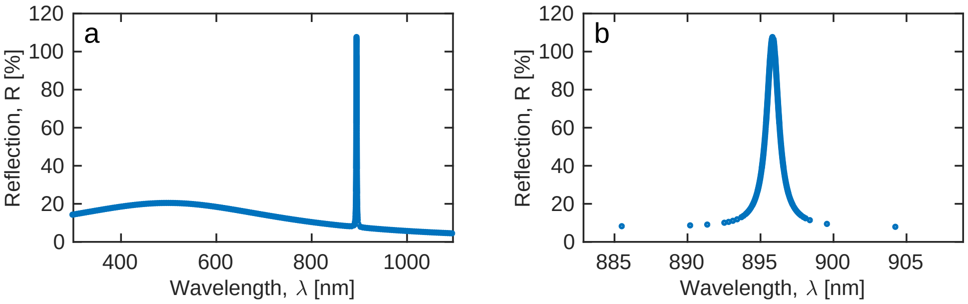

Figure 3: Output of example script, which imitates an electromagnetic simulation at a random position a) within a wide interval, with b) narrow line width. The resolution varies from 4.6 pm on the peak, to 4.6 nm in the flat parts of the spectrum. Achieving the same resolution with static spacing would require 370× as many points.

As actual electromagnetic simulations can be complex to set up and time-consuming to run, a test-function was written that imitates an actual simulation function, but returns values from an analytical evaluation. The script `asasim_Example_1_Imitator.m` exemplifies how the `asasim` method may be integrated with an arbitrary simulation function. A lorentzian of narrow line width (0.5 nm) is simulated at a random location within the broad interval 300–1100 nm, on a slightly sloped background. The time to run is ∼1 second, and figure 3 shows the results.

2.2. Photonic crystal slab sensor at varying angles of incidence

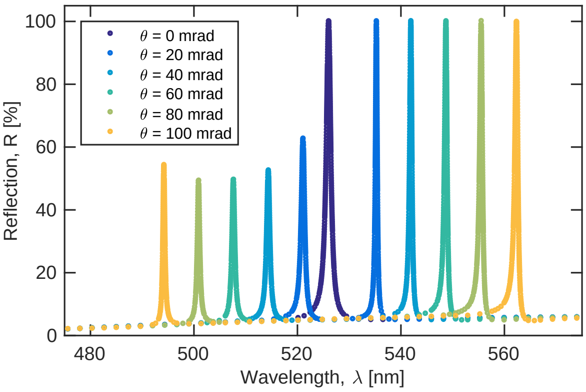

Figure 4: Example simulation of PCS sensor at varying angles of incidence. Each simulation has a variable resolution between 2 pm and 2342 pm depending on the local region.

GD-Calc is a MATLAB-package for RCWA, which can be downloaded from `http://kjinnovation.com/GD-Calc.html` and installed as per the instructions given. The workhorse of the GD-Calc package is the function `gdc.m`, which takes three inputs: a `Grating`-struct with the relevant grating parameters and geometric layout, an `IncField`-struct with information about the incoming field, and an `order`-matrix, specifying the diffraction orders to be used in the calculations. The function `gdcWrapper` has been written to interface `asasim` with GD-Calc. It defines the necessary three inputs and calls gdc.m to get a reflectivity value `R` at the given input wavelength `w`. An additional `FullOutput` struct contains all diffraction efficiencies. `asasim` uses this reflectivity value `R` to evaluate whether points neighboring `w` should be further resolved. The `asasim` system was recently used with RCWA to substantiate experimental observations of waveguide core swelling [9] in a PCS sensor. Here, the simulation parameters describe a linear grating of period 368 nm, duty cycle

50% and grating height 100 nm, illuminated at an angle θ. The model incorporates refractive index dispersion data for all three materials constituting the sensor, namely a cladding layer of Efiron PC409AP (Luvantix, Korea), a nano-structured core layer of HI01XP (micro resist technologies, Germany) and water as superstrate. In the example given here, simulations are performed in a broad wavelength interval of 450–850 nm, with angles of incidence in steps of 0.02 rad between 0 and 0.1 rad. The full example code is given in `asasim_Example_2_GDC.m`, and the result is shown in figure 4. It should be noted that `asasim` is incapable of displaying a progress bar during runtime due to parallel processing working asynchronously, and because the wavelengths to simulate are being refined adaptively, and are thus not known *a priori*. Instead, the total number of points calculated is displayed for each round to indicate progress. On the computer used here, the total run time for all 6 angles is ∼10 min.

2.3. Scattering cross section of plasmonic nanoparticles

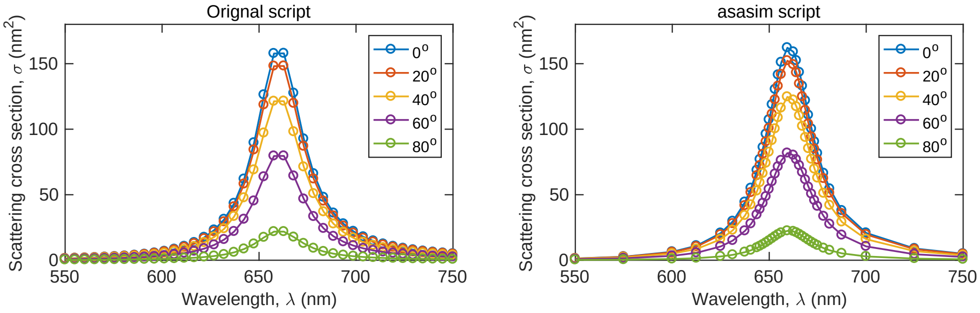

Figure 5: Simulation performed using the `mnpbem`-package. a) Using the default static spacing places 200 points, many of them off-peak. b) With adaptive resolution, the peaks are better resolved using only 165 points.

To demonstrate the versatility of `asasim`, it was also integrated with the excellent class `mnpbem`[10], available at `http://cpc.cs.qub.ac.uk/summaries/AEKJ_v3_0.html`, which is used for calculating scattering cross sections of plasmonic nanoparticles near surfaces. An example script, based the demonstration `demospecstat1.m` of that toolbox, is given in `asasim_Example_3_MNP.m`. Here, the per-wavelength `for`-loop is quite simply replaced by a call to `asasim` using `mnpWrapper`, which is functionally three lines long. As mentioned in section 2, the wrapper must take two inputs and return two outputs, and it serves as an example of how a wrapper function can be written. The resulting graph is shown in figure 5, and although there is perhaps limited gain from using `asasim` for simulating such wide peaks in a limited interval, the example illustrates how additional systems can be interfaced using a wrapper function. The code has a typical runtime of ∼3 seconds.

3. Background

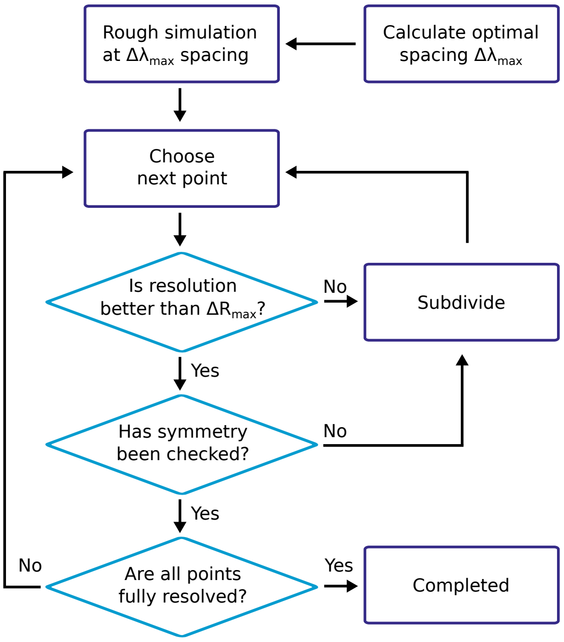

Figure 6: Working principle behind the algorithm. An initial rough simulation is performed in order to detect all relevant features. Then, each peak is further resolved by adaptive subdivisioning until the desired resolution is achieved. At this point, a symmetry-check is performed in order to ensure that two points with similar values are not just placed symmetrically around a peak.

A simplified illustration of the working principle is presented in figure 6, with the goal of producing a (λ, R)-spectrum using ΔR_{max} (goal resolution) and γ_{min} (minimum peak half-width) as input parameters. First, a rough simulation is performed, with the purpose of detecting all spectral features of interest. An optimum initial point spacing $\Delta\lambda_{\text{max}}$ is automatically calculated, such that any peak of a given minimum half-width γ_{min} is certain to cause a perturbation exceeding the threshold ΔR_{max} within the interval, flagging the region for further refinement.

After each round of simulations, the difference ΔR between neighboring points is evaluated, to identify regions that exceed ΔR_{max}. These will be further refined by subdivisioning. New points inherit the ΔR-value of its parent in that round, such that subdivisioning does not continue indefinitely.

When a point no longer exceeds $\Delta R_{\max}$, it is subdivided one last time as a symmetry-check. It is entirely possible for two points to be placed symmetrically around a peak, in which case their difference ΔR could be zero, without the upper part of the peak having been resolved. The symmetry-check safe-guards against this. If the difference still does not exceed $\Delta R_{\max}$, the region is considered fully resolved. Thus, once a peak is detected, i.e., at least one point satisfies the criterion $\Delta R > \Delta R_{\max}$, the entire peak always becomes fully resolved.

For the sake of argument, consider a lorentzian at an arbitrary location, i.e., $\lambda_0 = 0$, normalized so that $R(\lambda_0) = 100\%$:

$$R(\lambda) = \frac{1}{1 + \frac{\lambda^2}{\gamma^2}} \tag{1}$$

$$\lambda = \sqrt{\gamma^2 \left(\frac{1}{R} - 1 \right)} \tag{2}$$

Because of the subdivisioning-scheme employed, whenever a peak is detected, it is certain to come out fully resolved. Detection in this context entails that the perturbation from a peak causes two neighboring points, spaced apart by $\Delta\lambda$ on the first axis, to have a sufficient difference on the second axis, $\Delta R > \Delta R_{\max}$. The narrowest peak of half-width γ that is certain to be detected is then a peak that is so narrow, that its perturbation only just causes ΔR between any two neighboring points to exceed $\Delta R_{\max}$, even when the peak is placed right between those two neighboring points, such as points a and b in figure 7. In this case, ΔR is zero between them, so for detection, the difference to the *next* neighbor (point c) must instead satisfy $\Delta R > \Delta R_{\max}$. If the distance from the peak center to the first symmetrically placed neighbor (point b) is $\lambda_1 = \Delta\lambda/2$, then the distance to its next neighbor (point c) must be $3\lambda_1$. Thus,

$$\begin{aligned} \Delta R &= R_1 - R_2 \qquad (3) \\ &= \frac{1}{1 + \frac{\lambda_1^2}{\gamma^2}} - \frac{1}{1 + \frac{(3\lambda_1)^2}{\gamma^2}} \qquad (4) \end{aligned}$$

This does not have a simple solution for the optimal point spacing $\Delta\lambda = 2\lambda_1$, but it can be isolated as

$$\Delta\lambda = \left(\frac{2}{3} \sqrt{\frac{\gamma^2(4 - 5\Delta R) + 2\sqrt{2}\sqrt{\gamma^4(2\Delta R^2 - 5\Delta R + 2)}}{\Delta R}} \right) \tag{5}$$

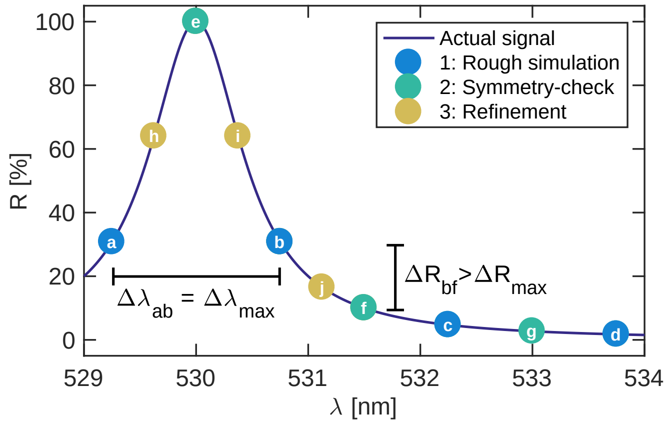

Figure 7: Illustration of points placed in the first three rounds of simulations. a-d) An initial rough-simulation is performed in order to detect all relevant features. e-g) A symmetry-check is performed in order to ensure that two points with similar values are not just placed symmetrically around the peak. h-j) Peak refinement continues until a desired resolution is achieved. Note that the spectrum beyond $\lambda > 531.3$ nm is not refined after round two.

4. Discussion

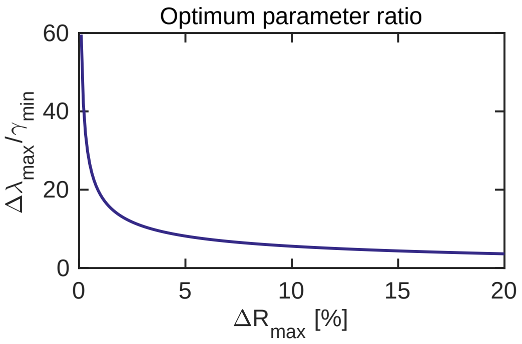

Figure 8: Optimum ratio of simulation parameters.

The optimum ratio between the parameters $\Delta\lambda_{\text{max}}$ and ΔR_{max} for a given γ_{min} is given by equation 5, and shown in figure 8. Parameter-sets below the curve are sub-optimal in the sense that they cause more simulation points to be calculated than necessary, wastefully increasing computation time. Sets above the curve will only serendipitously resolve peaks of a given half-width γ_{min}. As an example, if a simulation is to be performed with a 5% resolution on the y-axis, and the expected minimum half-width $\gamma_{\min}$ is 1 nm, the optimum spacing on the `x`-axis is 8.2 nm. At a resolution of 0.5%, the spacing can be 26.6 nm, while still detecting the perturbation from the narrow peak.

Decreasing $\Delta R_{\max}$ causes more points to be calculated on the R-axis, but this also increases $\Delta\lambda_{\max}$, reducing the number of points to be calculated initially on the λ-axis. In the simplest possible model, consider a spectrum only containing a single lorentzian peak with a half-width of γ. The number of points simulated on the fully resolved peak is $N_R = 2/\Delta R$, and the number of points to be simulated statically across the spectrum is $N_\lambda = (\lambda_{\max} - \lambda_{\min})/\Delta\lambda$. The total number of points to be simulated adaptively is

$$N = \frac{2}{\Delta R_{\max}} + \frac{\lambda_{\max} - \lambda_{\min}}{\Delta\lambda_{\max}} \tag{6}$$

Using this equation for estimating the number of simulation points, the two methods were compared for speed as shown in figure 9. It is clear that the adaptive method is generally a couple of orders of magnitude faster than the static method. The figure also illustrates the computational optimum for the ΔR and thus $\Delta\lambda$ parameters, which depend on the minimum necessary peak half-width $\gamma_{\min}$. Time-optimal parameters could be determined by combination of equations 5 and 6 and solving $\frac{dN}{d\Delta R_{\max}} = 0$, but this becomes rather unwieldy. As figure 9 indicates, the total number of simulated points does not vary steeply for similar values of ΔR, and so the choice of resolution is perhaps more a question of preference.

For comparison, in order to achieve the same R-axis resolution with static sampling as with adaptive sampling, the static first-axis point spacing must equal the smallest distance between two points separated by $\Delta R_{\max}$ on the second axis. For example, to resolve a peak of half-width $\gamma = 0.5$ nm at $\Delta R = 1\%$ resolution on the steepest part in an 800 nm interval, the adaptive resolution varies between 0.0046 nm and 4.6 nm, depending on the local spectral features. To achieve a static resolution of 0.0046 nm, more than 170,000 points would be required. With adaptive resolution, the same is achieved with 468 points, making the simulation 374× faster.

Apart from reducing computation time, a main advantage of `asasim` is the decreased amount of *a priori* information needed. As spectrally flat regions are computed very fast, the precise spectral positions of features need not be known beforehand in order to simulate the narrow region of relevance. Furthermore, whereas one might have to iteratively adjust first-axis resolution in order to achieve the desired second-axis resolution, with this method, resolution is decided for the second-axis directly.

While the amount of necessary *a priori* information is reduced, a rough estimate of the smallest realistic half-width is still required. The consequences of choosing a

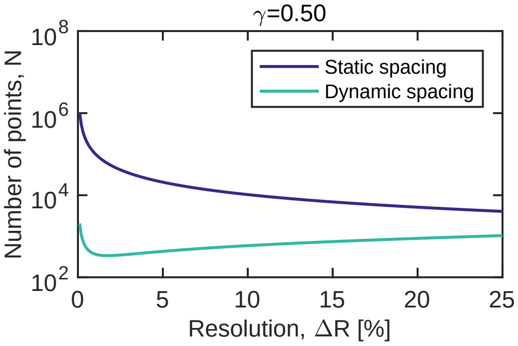

Figure 9: Number of points simulated as function of R-axis resolution.

poor value for this parameter was discussed in section 4. For very dense spectra, e.g., containing many closely spaced peaks such as interference patterns, the same amount of points may end up being simulated as using static spacing. Furthermore, when the background is strongly sloped, e.g., the resonance peak of interest resembles a bump on a larger and much broader peak, the background also becomes highly resolved. This is partially the case in figure 5.

Because the x-axis resolution varies across all spectra, direct comparison between spectra or presentation of data as an image will require interpolation. This is quite simply achieved using the built-in MATLAB-function `interp1`, as exemplified below.

Listing 3: Interpolation

```
dx = 0.01; % desired x-axis resolution
interpolatedX = min([Sim.xs]):dx:max([Sim.xs]);
interpolatedY = zeros(numel(Sim),numel(
   interpolatedX));
for iSim = 1:numel(Sim)
interpolatedY(iSim,:) = ...
interp1(Sim(iSim).xs,Sim(iSim).ys,...
interpolatedX,'linear');
end
imagesc(interpolatedX,1:numel(Sim),interpolatedY);
```

5. Summary

In summary, the presented method allows high-speed, high-resolution simulation of narrow-band spectral features in a broad range, with no *a priori* information about the location of spectral features. In one example, the number of points necessary to simulate was reduced from >170,000 to 468, with an accompanying reduction in computation time from ∼20 hours to ∼3 minutes. The solution is tailored to simulations of electromagnetic spectra containing lorentzian features, but can trivially be adapted to other simulation functions and other lineshapes. The solution easily plugs into existing simulation systems, and interfacing to three different simulation systems was demonstrated by examples.

Acknowledgements

The author gratefully acknowledges funding from the Danish Council for Strategic Research, DSF, under Grant Agreement No. 10-092322 (PolyNano).

References

[1] K. Byun, S. Kim, D. Kim, Design study of highly sensitive nanowire-enhanced surface plasmon resonance biosensors using rigorous coupled wave analysis., Optics express 13 (10) (2005) 3737–3742. `doi:10.1364/OPEX.13.003737`.

[2] E. Højlund-Nielsen, J. Clausen, T. Mäkela, L. H. Thamdrup, M. Zalkovskij, T. Nielsen, N. Li Pira, J. Ahopelto, N. A. Mortensen, A. Kristensen, Plasmonic Colors: Toward Mass Production of Metasurfaces, Advanced Materials Technologies 1 (7) (2016) 1600054. `doi:10.1002/admt.201600054`.
URL `http://doi.wiley.com/10.1002/admt.201600054`

[3] S. A. Boden, D. M. Bagnall, Optimization of moth-eye antireflection schemes for silicon solar cells, Progress in Photovoltaics: Research and Applications 18 (3) (2010) 195–203. `doi:10.1002/pip.951`.

[4] M. G. Moharam, T. K. Gaylord, Rigorous coupled-wave analysis of planar-grating diffraction, Journal of the Optical Society of America 71 (7) (1981) 811. `doi:10.1364/JOSA.71.000811`.
URL `https://www.osapublishing.org/abstract.cfm?URI=josa-71-7-811`

[5] M. Shokooh-saremi, R. Magnusson, Particle swarm optimization and its application to the Design of Diffraction Grating Filters, Optics Letters 32 (8) (2007) 894–896.

[6] C. Wang, S. Yu, W. Chen, C. Sun, Highly Efficient Light-Trapping Structure Design Inspired By Natural Evolution, Scientific Reports 3 (1) (2013) 1025. `doi:10.1038/srep01025`.
URL `http://www.nature.com/articles/srep01025`

[7] B. Rouet-Leduc, K. Barros, E. Cieren, V. Elango, C. Junghans, T. Lookman, J. Mohd-Yusof, R. S. Pavel, A. Y. Rivera, D. Roehm, A. L. McPherson, T. C. Germann, Spatial adaptive sampling in multiscale simulation, Computer Physics Communications 185 (7) (2014) 1857–1864. `doi:10.1016/j.cpc.2014.03.011`.
URL `http://dx.doi.org/10.1016/j.cpc.2014.03.011`

[8] O. Awile, F. Büyükkeçeci, S. Reboux, I. F. Sbalzarini, Fast neighbor lists for adaptive-resolution particle simulations, Computer Physics Communications 183 (5) (2012) 1073–1081. `doi:10.1016/j.cpc.2012.01.003`.
URL `http://dx.doi.org/10.1016/j.cpc.2012.01.003`

[9] K. T. Sørensen, C. B. Ingvorsen, L. H. Nielsen, A. Kristensen, On the practical achievement of high performance using a polymeric photonic crystal slab sensor, (unpublished).

[10] J. Waxenegger, A. Trügler, U. Hohenester, Plasmonics simulations with the MNPBEM toolbox: Consideration of substrates and layer structures, Computer Physics Communications 193 (2015) 138–150. `arXiv:1412.5467`, `doi:10.1016/j.cpc.2015.03.023`.
URL `http://dx.doi.org/10.1016/j.cpc.2015.03.023`

On the practical achievement of high performance using a polymeric photonic crystal slab sensor

KRISTIAN TØLBØL SØRENSEN,[1] CHARLOTTE BONDE INGVORSEN,[1]
LINE HAGNER NIELSEN[1] AND ANDERS KRISTENSEN[1,*]

[1]*DTU Nanotech, Technical University of Denmark, Ørsteds Plads building 345C, 2800 Kgs. Lyngby, Denmark.*

[*]*anders.kristensen@nanotech.dtu.dk*

Abstract: A photonic crystal slab (PCS) sensor is a universal refractive index sensor with possibilities and performance very similar to surface plasmon resonance (SPR), which represents the gold standard of biosensing. Both technologies detect refractive index variation within a few hundred nanometers of the sensor surface, but SPR requires gold deposition and prismatic coupling of light. Instead, cheap PCS sensors can be made vacuum-free entirely out of polymers and can be read out in free-space using white light. Although advantageous in those aspects, polymeric PCS sensors come with additional challenges, besides those relating to temperature-variations, which must be considered in any refractive index based method: as the polymer matrix can absorb a certain amount of fluid from the sample of interest, sensor equilibration must be controlled. We present a conceptually simple approach for real-time monitoring of sample exchange equilibration, as well as precise compensation for temperature fluctuations. This enables drift-free, high-performance operation of a polymeric PCS sensor.

OCIS codes: (050.0050) Diffraction and gratings; (160.0160) Materials; (240.0240) Optics at surfaces; (280.0280) Remote sensing and sensors; (310.0310) Thin films.

References

1. Garet G Nenninger, Marek Piliarik, and Jiří Homola. Data analysis for optical sensors based on spectroscopy of surface plasmons. *Measurement Science and Technology*, 13(12):2038–2046, dec 2002.
2. Ian D. Block, Leo L. Chan, and Brian T. Cunningham. Large-area submicron replica molding of porous low-k dielectric films and application to photonic crystal biosensor fabrication. *Microelectronic Engineering*, 84(4):603–608, 2007.
3. Marek Piliarik and Jiří Homola. Surface plasmon resonance (SPR) sensors: approaching their limits? *Optics Express*, 17(19):16505, 2009.
4. Robert Magnusson and S. S. Wang. New principle for optical filters. *Applied Physics Letters*, 61(9):1022–1024, aug 1992.
5. Brian T. Cunningham. Label-Free Assays on the BIND System. *Journal of Biomolecular Screening*, 9(6):481–490, 2004.
6. Robert Magnusson and Mehrdad Shokooh-Saremi. Physical basis for wideband resonant reflectors. *Optics express*, 16(5):3456–3462, 2008.
7. Kristelle Bougot-Robin, Shunbo Li, Yinghua Zhang, I-Ming Hsing, Henri Benisty, and Weijia Wen. “Peak tracking chip” for label-free optical detection of bio-molecular interaction and bulk sensing. *The Analyst*, 137(20):4785–4794, 2012.
8. Pétur G. Hermannsson, Kristian T Sørensen, Christoph Vannahme, Cameron L.C. Smith, Jan J Klein, Maria-Melanie Russew, Gabi Grützner, and Anders Kristensen. All-polymer photonic crystal slab sensor. *Optics Express*, 23(13):16529–16539, jun 2015.
9. Yousef Nazirizadeh, Volker Behrends, Aurél Prósz, Norbert Orgovan, Robert Horvath, Ann M. Ferrie, Ye Fang, Christine Selhuber-Unkel, and Martina Gerken. Intensity interrogation near cutoff resonance for label-free cellular profiling. *Scientific Reports*, 6(1):24685, jul 2016.

10. Yu Chung Lin, Wen Hsin Hsieh, Lai Kwan Chau, and Guo En Chang. Intensity-detection-based guided-mode-resonance optofluidic biosensing system for rapid, low-cost, label-free detection. *Sensors and Actuators, B: Chemical*, 250:659–666, 2017.
11. Dustin Gallegos, Kenneth D. Long, Hojeong Yu, Peter P. Clark, Yixiao Lin, Sherine George, Pabitra Nath, and Brian T. Cunningham. Label-free biodetection using a smartphone. *Lab on a Chip*, 13(11):2124, 2013.
12. Brian Cunningham, Bo Lin, Jean Qiu, Peter Li, Jane Pepper, and Brenda Hugh. A plastic colorimetric resonant optical biosensor for multiparallel detection of label-free biochemical interactions. *Sensors and Actuators, B: Chemical*, 85(3):219–226, 2002.
13. Daniela Threm, Yousef Nazirizadeh, and Martina Gerken. Photonic crystal biosensors towards on-chip integration. *Journal of Biophotonics*, 5(8-9):601–616, aug 2012.
14. Masahiko Daimon and Akira Masumura. Measurement of the refractive index of distilled water from the near-infrared region to the ultraviolet region. *Applied Optics*, 46(18):3811, 2007.
15. Maria Fernanda Pineda, Leo Li-Ying Chan, Theresa Kuhlenschmidt, Charles J. Choi, Mark Kuhlenschmidt, and Brian T. Cunningham. Rapid Specific and Label-Free Detection of Porcine Rotavirus Using Photonic Crystal Biosensors. *IEEE Sensors Journal*, 9(4):470–477, 2009.
16. Robert Magnusson, Debra Wawro, Shelby Zimmerman, and Yiwu Ding. Resonant photonic biosensors with polarization-based multiparametric discrimination in each channel. *Sensors*, 11(2):1476–1488, 2011.
17. Pétur G. Hermannsson, Christoph Vannahme, Cameron L C Smith, Kristian T. Sørensen, and Anders Kristensen. Refractive index dispersion sensing using an array of photonic crystal resonant reflectors. *Applied Physics Letters*, 107(6), 2015.
18. Kristian Tølbøl Sørensen. asasim: Adaptive Sampling for Electromagnetic Simulations. *submitted to Computer Physics Communications*.

1. Introduction

Surface plasmon resonance (SPR) has become a gold standard [1, 2] for label-free biomolecular investigations with excellent detection limits on the order of 10^{-6} RIU [3]. However, the technique places high demands on both chips and readout instrumentation, making the technology expensive to both acquire and employ. An alternative class of optical sensor exists, known as a guided mode resonance filter [4, 5], leaky-mode reflector [6], resonant waveguide grating [7], or, as it will referred to here, a photonic crystal slab (PCS) sensor [8]. Compared to SPR, this sensor can be read out using much simpler instrumentation, such as an LED and a photodiode [9, 10] or even a smartphone [11]. Roll-to-roll high-throughput fabrication was demonstrated at an early stage [12], and well-plates with PCS sensors on the bottom are commercially available [5]. However, the price-tag may pose a barrier to many potential applications.

For the lowest possible cost price of consumables, it is desirable to have the sensors made entirely out of polymers. The feasibility of this has already been documented [8], yet for the cheap polymeric optical sensors to be competitive with those produced using expensive vacuum-based methods, the device operation must be highly optimimzed. In this work, we outline best practices for achieving high performance using a polymeric PCS sensor.

Refractive index sensors are universal in the sense that almost any change to a fluid will change its refractive index, making the sensor capable of monitoring practically any change in the fluid. This versatility comes at the cost of increased demands for variable control, as refractive index itself is sensitive to, e.g., thermal fluctuations. PCS sensors tend to amplify such fluctuations, as the permittivities of the materials constituting the sensor are also affected by temperature. Obviously, the issue may be alleviated by thermal control [1, 13], however, a 0.1 °C increase in temperature still reduces the refractive index of water by $\Delta n_D = 1 \cdot 10^{-5}$ RIU [14], which may additionally be amplified several times by the PCS. Furthermore, in order to monitor transient effects, thermal compensation is desirable.

In order to cancel out thermal contributions, a common approach is to have neighboring sensors serve as references [5, 15]. Alternatively, transverse electric (TE)- and transverse magnetic (TM)-mode resonances can be monitored simultaneously [16], uniquely enabling referencing at the exact same physical location. As the mode confinement differs between the resonances of the two light polarizations, one resonance predominantly responds to events at the surface, whereas the other is more sensitive to the bulk. In this work, we produce a reference region on a part of the sensor surface, such that both sample and reference regions may be read out simultaneously and in close proximity, as illustrated in figure 1.

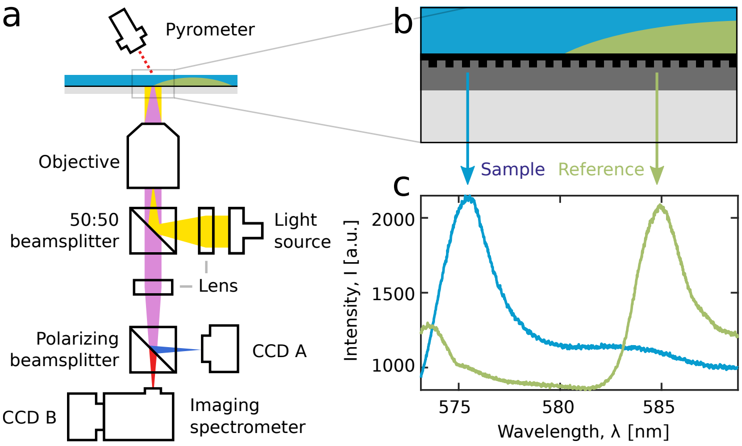

Figure 1. Experimental setup and operating principle of the PCS sensor, using a) an optical setup which ensures collimated, normal incidence illumination of the b) sensor, illustrated here in cross-section. A reference material partially covers the sensor, increasing the c) resonance wavelength relative to the sample.

2. Method

A polymeric PCS sensor was fabricated based on previous work [8]. A 2 mm thick slab of poly(methyl methacrylate) (PMMA) was laser-cut to a diameter of 100 mm and plasma-treated (Pico Plasma Asher, Diener Electronic, Germany) for hydrophilicity. A droplet of low-refractive index polymer Efiron AC409-AP (Luvantix, Korea), diluted to 85% w/w in 2-butanone (Sigma-Aldrich, MO, USA), was then sandwiched between the PMMA substrate and a silicon stamp. The stamp had been defined by electron-beam lithography to contain 4 × 4 areas of 2 mm × 2 mm, each containing a linear grating of period $\Lambda = 368$ nm and depth $d = 100$ nm. After curing by a 1000 W UV flood exposure (Oriel Flood Exposure Source, Newport Corp., CA, USA), the substrate was separated from the stamp and baked at 90 °C for 3 min. The high-refractive index dielectric waveguide core was produced either using ion beam sputter deposition (Ionfab 300, Oxford Instruments, GB) of 80 nm titania (TiO_2), or by polymer spincoating (Süss MicroTec, Germany) for a genuinely polymeric sensor. In that case, a high-refractive index polymer HI01XP (micro resist technologies GmbH, Germany), diluted to 15% w/w in ma-T 1050 (micro resist technologies) was spincoated at 3,000 rpm for 1 min. The layer was then UV flood exposed in oxygen-free atmosphere for 5 min.

The thus finished PCS sensor subsequently had small droplets of Efiron manually deposited, such that they covered a part of each sensor. Following oxygen-free UV curing, the resulting reference regions typically had a diameter 400–1000 μm and a height of 10–50 μm as ascertained by profilometry (Dektak 8, Veeco Instruments, NY, USA, data not shown). This part of the fabrication process is suitable for patterning, e.g., via photolithography, but the full process would need to be compatible with the chemical and physical stability of all polymers involved. For characterizing the evolution of thin-film thickness and refractive index over time, variable angle spectroscopic ellipsometry (J.A. Woollam, NE, USA) was used.

The laboratory setup is described in ref. [17], and illustrated in figure 1. Where nothing else is stated, components were purchased from Thorlabs (NJ, USA). Briefly, white light from a bright and spectrally flat light source (EQ-99X LDLS, Energetiq, MA, USA) was output through a fiber collimator onto an adjustable mirror, shining through a focusing lens onto a 50-50 beamsplitter, through a 4× objective, ensuring collimated input light interacting with the sensor at nominally normal incidence. The sensor wafer was mounted on a motorized stage. Reflected light was transmitted through the objective and beamsplitter, encountering a mirror and tube lens before reaching a polarizing beamsplitter. TM-polarized light was collected by the imaging CCD A, whereas TE-polarized light was received by CCD B of an imaging spectrometer (Acton SP2750, Princeton Instruments, NJ, USA). A pyrometer (CSlaser LT hs CF1, Optris GmbH, Germany) was mounted on the stage and focused on the water droplet in cases where complementary temperature monitoring was used. To avoid evaporation during long time series, an air-tight lid was placed on top of the wetted sensor.

The imaging spectrometer was operated at an effective integration time of 0.1–30 s, depending on the desired temporal resolution. Each spectral image was recorded using LightField 6.2 (Princeton Instruments) and contained 100 spectra, providing a one-dimensional spatial resolution of 5 μm. Each spectrum was resolved into 1340 pixels with a spectral resolution of 12 pm. Time series of up to 1000 frames were imported into MATLAB 2016b (The MathWorks Inc., MA, USA) using a custom function and organized into a 3D matrix, thus containing up to $1.34 \cdot 10^8$ intensity values of 32 bit depth. The matrix dimensionality was first reduced to 2D by calculating the centroid resonance wavelength of each spectrum after a 50% thresholding, and then to 1D by binning the sample- and reference regions.

Rigorous coupled-wave analysis (RCWA) simulations were carried out using the Grating Diffraction Calculator (KJ Innovation, CA, USA) package implemented in MATLAB. The model was set up with the refractive index dispersion of Efiron and HI01XP as substrate and waveguide core layers, respectively. The grating had a period of 368 nm and a depth of 100 nm. The core thickness was 183 nm, in accordance with ellipsometer measurements, and the angle of incidence was 0°. The `asasim` algorithm[1] for adaptive resolution refinement was used to locate and adequately resolve all spectral features, making the computation 241× faster than a simulation of identical resolution without `asasim`.

3. Results and discussion

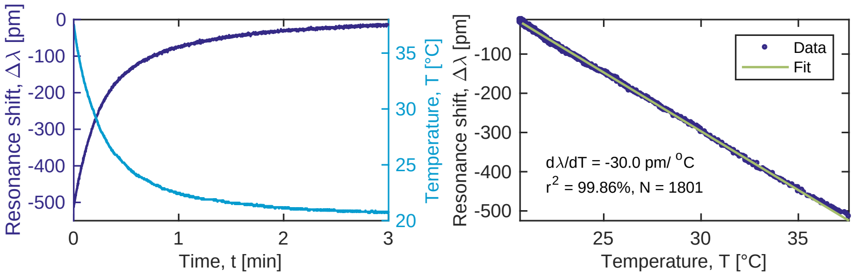

Figure 2. a) A deliberate temperature perturbation reveals b) the thermo-optic coefficient of the sensor in water, by correlating the resonance wavelength shift with temperature as measured by a pyrometer.

The amplified temperature sensitivity due to thermally induced refractive index changes in the

---

[1] open-source code available in ref. [18].

sensor stack, was investigated by adding a droplet of heated water to a thermally equilibrated volume of water sitting on a titania-type sensor. The result is shown in figure 2. The temperature was measured using a pyrometer simultaneously with resonance shift monitoring. As the refractive index sensitivity of these sensors was $d\lambda/dn = 90$ nm/RIU, the effective thermo-optic coefficient of the sensor in water was determined to be $dn/dT = 3.3 \cdot 10^{-4}$ RIU/°C, an amplification of 3.3× compared to the thermo-optic coefficient of water itself [14], potentially making temperature control insufficient and exacerbating the need for thermal referencing.

For a PCS sensor, the resonance shift measured in a sample S can be considered $\Delta\lambda_S = \sum_i \Delta\lambda_i$, where $\Delta\lambda_i$ are the individual contributions making up the resonance shift. Assuming the sensor itself to be stable over time, and that the analyte does not adhere to the sensor surface, the observed resonance shift is expected to have only two contributions, namely changes in analyte concentration Δc and temperature ΔT. Thus, $\Delta\lambda_S = \Delta\lambda_{\Delta c} + \Delta\lambda_{\Delta T}$. Although the $\Delta\lambda_{\Delta T}$ term is straightforwardly determined using a pyrometer as described, this would be unsuitable for the many promising applications involving microfluidics [13], while increasing cost and complexity of the necessary instrumentation. Alternatively, the temperature-contribution may be isolated by making a sensor region insensitive to the liquid composition, while retaining its sensitivity to temperature fluctuations. In practice, this was achieved by shielding the reference region R with a polymer layer of thickness greater than the mode overlap. For example, the polymeric sensors used here had an evanescent decay length of $\hat{e} = 138$ nm in water, meaning that 99.999% of the sensor sensitivity is found within the first 1.3 μm from the surface. Ensuring that the reference polymer is thicker than this, but still very thin in order to minimize lag, thermal fluctuations will transfer to the sensor through the polymer, enabling drift compensation. Changes in analyte concentration will then not affect the reference region.

The part of a resonance shift originating from the temperature contribution is expressed as $\Delta\lambda_{\Delta T} = \Delta\lambda_R \cdot C$, where $\Delta\lambda_R$ is the resonance shift measured in the reference region, and C is an empirical constant, that takes into account the thermo-optic coefficients dn/dT of the sample, reference polymer, and each component of the sensor stack. Then, assuming that the bulk concentration change is $\Delta c = 0$, the resonance shift measured in the sample correlates with the resonance shift in the reference region as $\Delta\lambda_S = 0 + \Delta\lambda_R \cdot C$. Once C has been determined, the resonance shift owing solely to concentration changes is

$$\Delta\lambda_{\Delta c} = \Delta\lambda_S - C \cdot \Delta\lambda_R \tag{1}$$

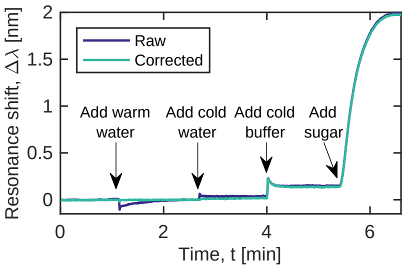

Figure 3. Temperature perturbations are effectively cancelled by thermal compensation, ensuring a stable and drift-free baseline. With thermal effects accounted for, the time for full mixing of the buffer becomes clearly visible at $t = 4$ min.

With effective temperature compensation, a flat baseline can be achieved even in the presence of drift and sample perturbations, as shown in figure 3. A steady baseline is disturbed by the addition of warm and cold water at $t = 1.1$ min and $t = 2.6$ min, respectively. The only difference here would be a slight temperature variation, which is effectively canceled by the thermal compensation method, maintaining a stable baseline. Then, at $t = 4.0$ min, buffer is added. This time, a perturbation is caused by both the mixing of buffer salts with the existing sample, as well as a slight temperature fluctuation. Due to the independence from thermal contributions afforded by the method, sample mixing time is decoupled from the thermal equilibration process, and full mixing is observed to take ~ 15 s.

So far, we have only discussed the situation where the only two contributions to the measured resonance shift is assumed to be concentration and temperature changes. However, additional contributions can be relevant to certain applications, e.g., for biosensors, a contribution from biorecognition events would be the main parameter of interest. When additional contributions are present, $\Delta\lambda_{\Delta c=0} = \Delta\lambda_S - F \cdot \Delta\lambda_R \neq 0$, and hence the model can also be used to check for additional, perhaps unexpected contributions.

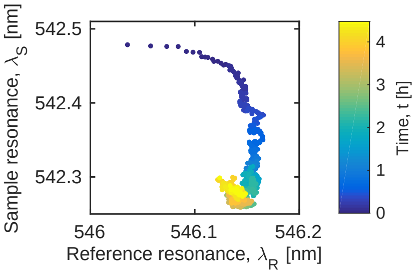

Figure 4. Resonance wavelength of the sample region (λ_S) versus the reference region (λ_R) over time. The blue-shifting of the sample resonance over the first ~ 1.5 h may be due to water absorption into the exposed waveguide core. The shielded reference region is relatively stable during the period.

Figure 4 illustrates such a situation, where at $t = 0$, the dry sensor is exposed to water and enclosed under a lid. Initially, both resonance regions shift together, but soon, only the sample resonane has an appreciable shift. As the water sample is unperturbed, this can neither be due to evaporation, other changes in bulk concentration, non-specific analyte binding, nor temperature drift. Rather, it is hypothesized that water slowly absorbs into the polymeric waveguide core layer. A some-hours long equilibration time is consistently observed when wetting polymeric PCS sensors, however, the magnitude and duration varies, possibly due to varying environmental conditions such as air humidity prior to wetting. In case water uptake happens by displacement or dissolution of microscopic air pockets, the waveguide core refractive index should increase. If it happens through swelling of the polymer, the refractive index should decrease.

The observed blue-shifting of the sample resonance wavelength by hundreds of picometers is consistent with a reduction of the waveguide core refractive index, i.e., swelling of the polymer matrix. In order to investigate this, an ellipsometer was used to monitor the outgassing of a sensor wafer which had been submerged in water overnight. The results are shown in figure 5a, and indicate an increase in waveguide core refractive index and a concomitant decrease in thickness, in agreement with the hypothesized swelling from water absorption. When F is the fraction of the core volume comprised of water, the core refractive index n_{core} is assumed to be described by

$$n_{\text{core}} = n_w F + n_p(1 - F) \tag{2}$$

where n_w and n_p are the refractive indices of water and core-polymer, respectively. Thus, the measured change in refractive index corresponds to a water content of $F = 0.3\%$. It is noted that the change in thickness over this period is also $\sim 0.3\%$.

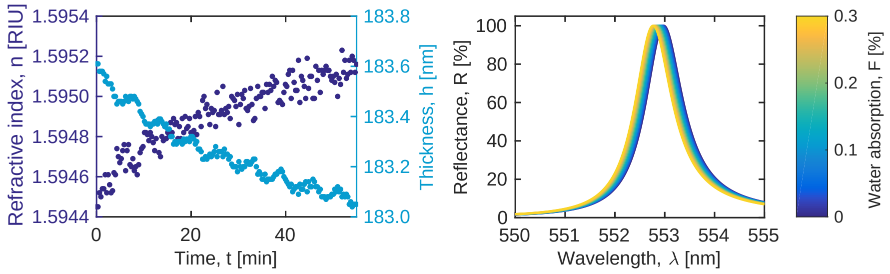

Figure 5. Water degassing investigated by a) ellipsometer, indicating concomitant core layer shrinking and refractive index increase, and by b) RCWA, indicating a 215 pm resonance shift in response to the changes measured by ellipsometry. The result is consistent with the direct sensor readout data.

The effect of water absorption into the waveguide core layer was furthermore investigated by RCWA, as shown in figure 5b. A shift of 215 pm is observed when the waveguide core thickness increases by up to 0.3%, and its refractive index decreases similarly. This shift is in agreement with the experimental observations. Thus, for high-performance operation of a polymeric PCS sensor, in practice, it must be primed for hours prior to use, and thermal contributions must be accurately isolated.

4. Conclusion and outlook

In summary, we have shown that by fabricating a reference region of known refractive index, thermal drift can be fully compensated, in practice improving the performance of polymeric PCS sensors. By reliable decoupling of thermal effects from the sensor readout, it was established by three complementary techniques that the polymeric PCS sensors absorb ~ 0.3% water over several hours, after which they remaining stable. Thus, devices should always be primed before use. Polymeric PCS sensors can be produced at a much lower price than conventional PCS sensors, although the requirement for constant wetting makes them more suitable for microfluidic integration than as free-standing sensors.

Acknowledgements

The authors gratefully acknowledge funding from the Danish Council for Strategic Research, (DSF, Grant No. 10-092322), the Danish National Research Foundation (DNRF122) and Villum Fonden (Grant No. 9301) for Intelligent Drug Delivery and Sensing Using Microcontainers and Nanomechanics (IDUN). Line Hagner Nielsen would like to acknowledge the Danish Research Council for Technology and Production (FTP), Project DFF 4004-00120B for financial support.

micromachines

Article

Label-Free Monitoring of Diffusion in Microfluidics

Kristian Tølbøl Sørensen and Anders Kristensen *

Department of Micro- and Nanotechnology, Technical University of Denmark, Kongens Lyngby, 2800, Denmark; kriss@nanotech.dtu.dk
* Correspondence: Anders.Kristensen@nanotech.dtu.dk; Tel.: +45-4525-6331

Received: 4 October 2017; Accepted: 6 November 2017; Published: date

Abstract: Label-free, real-time detection of concentration gradients is demonstrated in a microfluidic H-filter, using an integrated photonic crystal slab sensor to monitor sample refractive index with spatial resolution. The recorded diffusion profiles reveal root-mean-square diffusion lengths for non-fluorescing and non-absorbing molecules, both small (glucose, 180 Da) and large (bovine serum albumin, 67 kDa).

Keywords: optofluidics; microfluidics; diffusion; convection; mixing; refractive index; label-free

---

1. Introduction

Microfluidics have become a standard solution to challenges involving accurate fluid control and small sample volume [2], as the laminar flow conditions often employed in microfluidics ensure mixing of compounds only by molecular diffusion. Such processes can be monitored easily when liquids are visible, but may leave the experimenter blind when using non-absorbing and non-fluorescing compounds. In these cases, the effects of flow adjustments may perhaps only be recognized after off-line analysis.

Depending on its application, the microfluidic structure employed in this paper is referred to as an H-filter [3,4], typically when its purpose is to filter smaller molecules from larger particles, or a T-sensor, when its purpose is to monitor the diffusion and interaction of analytes [2,5]. Such devices have been used to investigate, e.g., protein binding [6], chemical extraction [7,8], blood dialysis [9], and for membrane-less fuel cells [10]. Devices for flow injection analysis [11], general flow focusing [12], and spiral microfluidics [13] are also closely related, and the ability to monitor the extent of diffusion is also highly relevant to those applications. In general, molecular diffusivity is a central physical property, governing chemical reaction kinetics and mass transfer phenomena, which are often at the core of microfluidic architectures.

A photonic crystal slab sensor (PCSS) [14], also referred to as a guided mode resonance filter [15], leaky-mode resonant reflector [16], or resonant waveguide grating [17] is an optical sensor, which responds to changes in refractive index (RI) within the first few hundred nanometers from its surface. Such RI sensors are universal, in the sense that they neither require compounds to be conducting, absorbing nor fluorescing. The fact that this class of sensors operate label-free is of convenience in many applications, as the process of labelling may not always be trivial, and for diffusion monitoring this is of critical importance, as the label itself would affect the very property under investigation. PCSSs have been demonstrated for, e.g., protein binding affinity [18] and kinetics [19], and cell culture monitoring [20]. They are generally realized by deposition of a high-RI dielectric material such as titanium dioxide [21] or a suitable polymer [14] onto a sub-wavelength grating, which may be produced by nanoimprint-lithography into a polymer [22].

Here, we report an optofluidics system for universal detection of concentration gradients and monitoring of diffusion. As a proof-of-concept, we demonstrate a PCSS-embedded microfluidic H-filter, comprised entirely of polymers, illustrated conceptually in Figure 1. The H-filter is a common and versatile microfluidic component which separates compounds by size. We show that this optofluidic device allows label-free, real-time resolution of concentration gradients, both for small molecules and large proteins. To our knowledge, this is the first demonstration of real-time diffusion monitoring of non-absorbing, non-fluorescing species flowing in a microfluidic H-filter.

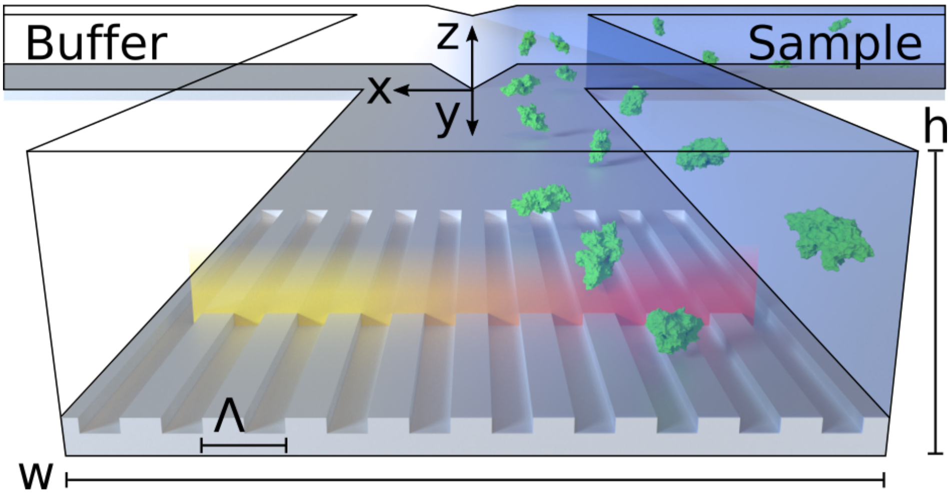

Figure 1. Schematic illustration of the sensor-embedded microfluidic H-filter operating principle. Two liquid streams meet and co-flow laminarly in a channel of height h and width w. The embedded sensor has a grating period of Λ and measures along a line. The color of light reflected by the sensor redshifts as molecules diffuse along x. Small molecules, shown in blue, will diffuse further and thus have a softer transition profile than larger molecules, exemplified by bovine serum albumin (BSA) in green (crystal structure 4F5S) [1]. The embedded label-free sensor monitors the extent of diffusive mixing in real-time.

2. Theory

To avoid convective mixing through turbulence, it is a critical requirement that the H-filter be operated under laminar flow conditions, e.g., at a low Reynolds-number, $Re = \rho \bar{v} h / \eta$, where ρ is the fluid density, $\bar{v}$ is the average flow velocity and η is viscosity. For the channel dimensions and flow rates employed in this paper, the channel height h is the characteristic length, and the Reynold's number in water becomes $Re < 0.1$, ensuring strictly laminar flow. Under these conditions, the only way for a molecule to transverse the channel is by diffusion.

Einstein showed that the root-mean-square displacement of a molecule undergoing Brownian motion, in the following referred to as diffusion length $\bar{x}$ (see Figure 1 for coordinate system), is given by $\bar{x} = \sqrt{2Dt}$, where D is the mass diffusivity and t is the diffusion timescale.

Fick's second law relates the change in concentration (ϕ) over time to change in concentration over space (x) for a diffusing analyte: $\delta\phi/\delta t = D\delta^2\phi/\delta x^2$, which in one dimension has the solution:

$$\phi(x) = \phi_0 \mathrm{erfc}\left(\frac{x}{2\sqrt{Dt}}\right) = \phi_0 \mathrm{erfc}\left(\frac{x}{\sqrt{2}\bar{x}}\right) \tag{1}$$

where ϕ_0 is the concentration originally in the sample stream. Fitting this equation to an observed diffusion profile directly reveals the diffusion length $\bar{x}$.

Due to the parabolic flow profile causing molecules near the walls to move at a lower velocity, molecules near the walls are able to diffuse further across the channel than molecules found closer to the center of the channel, where the flow velocity is highest. This effect was named the butterfly effect by Kamholz et al. [6] due to its shape, and it allows an increased diffusion length for molecules advecting near a wall. However, this gradient evens out when the advective transport rate is low compared to the diffusive transport rate, a relationship described by the Péclet-number $Pe = \bar{v}h/D = Q/(wD)$, where Q is the volumetric flow rate and w is the channel width. Diffusion length $\bar{x}$ is independent of z when $y/h \gg Pe \gg 1$ [23]. This is important for the measured diffusion length to be representative for the whole channel, as the PCSS measures the concentration gradient within the first few hundred nanometers from the sensor wall.

For pressure-driven flow, the relationship between pressure gradient Δp, flow rate Q and hydraulic resistance R_{hyd} is given by the Hagen-Poiseuille law [24] $\Delta p = QR_{\text{hyd}} = 12\eta LQ/(h^3 w)$, where L is the length of the wide and shallow channel ($h \ll w$).

3. Method

Figure 2A shows the optical system used to read out the optofluidic device, as previously described [14]. Briefly, the setup features a bright and spectrally flat, white light source (EQ-99X LDLS, Energetiq Technology, Inc., Woburn, MA, USA), directed through a lens, beamsplitter and microscope objective to ensure illumination of the sensor wafer at normal incidence. Reflected light was guided back through the microscope objective and beamsplitter, and directed into an imaging spectrometer (Acton SP2750, Princeton Instruments, Trenton, NJ, USA) by a mirror, a tube lens and a polarizing beamsplitter. This setup ensured that only resonantly reflected light of transverse electric (TE) polarization reached the spectrometer, while the transverse magnetic (TM) light component was received by a camera CCD (Thorlabs, Newton, NJ, USA) and used for navigation. The resonance wavelength relates to the fluid refractive index [21], which is proportional to concentration (in *w*/*v*% [25]).

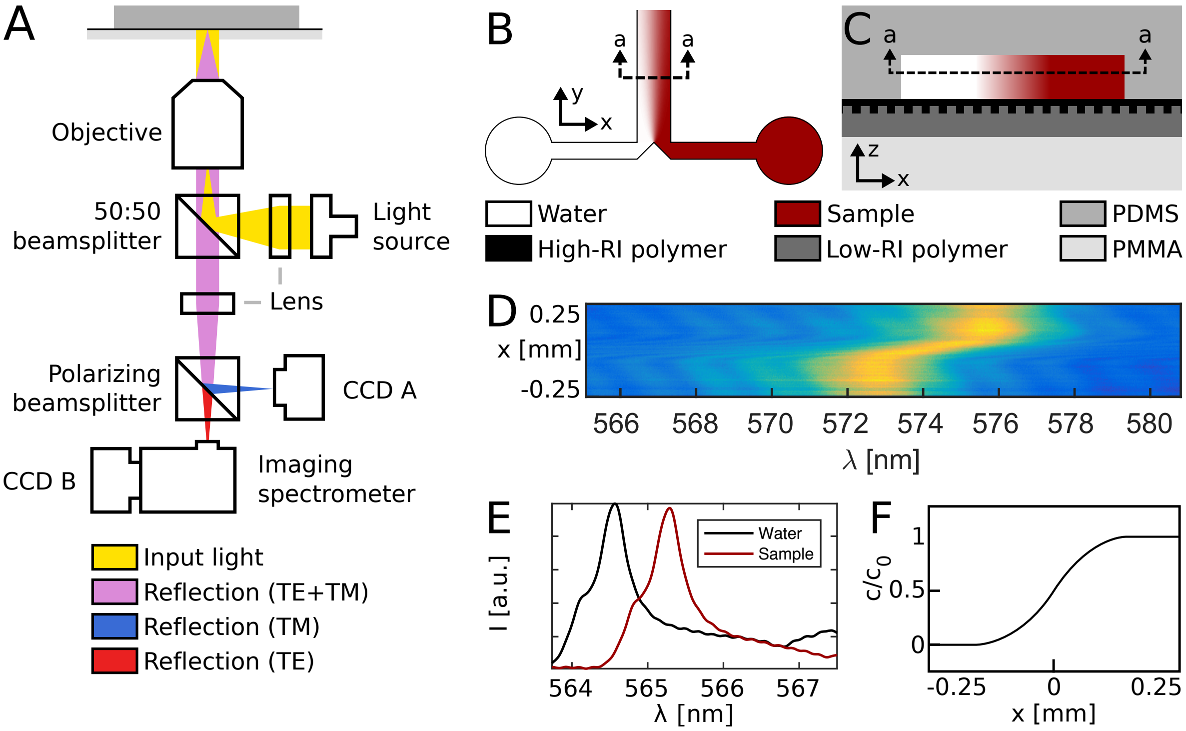

Figure 2. Setup and device operation. (**A**) Schematic overview of optical components. Light reflected by the sensor is received by an imaging spectrometer and used to monitor refractive index changes. (**B**) Top view of the microfluidic system. Two liquid streams co-flow and mix only by diffusion. (**C**) Side view of the sensor-embedded microfluidic H-filter, comprised by four different polymers. (**D**) Sample spectral image showing the concentration gradient. (**E**) Resonance peaks at two positions. The presence of analyte red-shifts the resonance wavelength. (**F**) Diffusion profile as revealed by the embedded sensor.

Microfluidic devices, illustrated in Figure 2B, were produced by casting of polydimethylsiloxane (PDMS, Sylgard 184, Dow Corning, Midland, MI, USA) on a silicon stamp to a thickness of approx. 10 mm, followed by a 2-h curing at 80 °C. The stamp was produced by standard UV photolithography into a 9 µm thick AZ-4562 resist film, using a custom photomask (Delta Mask, Enschede, The Netherlands). The mask defined channels of $w = 1$ mm width and $L = 20$ mm length, with a channel height $h = 9$ µm as defined by the resist thickness. This height was verified by profilometry and Fabry-Pérot interference analysis. Before using the silicon stamp for PDMS casting, a perfluorodecyltrichlorosilane coating was applied by molecular vapor deposition. Inlet holes were punched using a 0.5 mm diameter biopsy punch (World Precision Instruments Ltd., Sarasota, FL, USA), and the microfluidic device formed a strong and irreversible bond upon contact with the sensor wafer, after the two parts had been exposed to 60 s of oxygen plasma at 150 W.

The all-polymer sensor wafer was fabricated as described by Hermannsson et al. [14]. Briefly, a low-RI polymer, Efiron PC-409AP (Luvantix ADM, Daejeon, Korea), was diluted to 85% in 2-propanone (Sigma Aldrich, St. Louis, MI, USA), and UV nanoimprinted on a 2 mm thick poly(methyl methacrylate) (PMMA) substrate, using a silicon stamp defined by electron beam lithography. The stamp featured 4 × 4 fields, each of 2 mm × 2 mm, spaced 9 mm apart, with a grating period of $\Lambda = 368$ nm and a grating depth of $d = 100$ nm. A high-RI polymer, HI01XP (Micro Resist Technology GmbH, Berlin, Germany), was diluted to 25% in ma-T 1050 (Micro Resist Technology GmbH) and spincoated at 3000 rpm for 60 s to form a homogenous, conformal layer. After at 3-min bakeout at 90 °C, the wafer was flood exposed in a nitrogen atmosphere for 5 min. Figure 2C illustrates the polymer stack comprising the optofluidic system after bonding.

Liquids were driven using a 4-channel digital pressure controller (MFCS Flex, Fluigent, Inc., Villejuif, France). Channels were first wetted using buffer, which for the case of glucose was merely MilliQ water, or phosphate buffered saline (PBS, Sigma Aldrich) for the case of bovine serum albumin (BSA, Sigma Aldrich). In the case of BSA, a full surface passivation was first performed, by leaving a 30 mg/mL solution in the channels for 30 min before starting the experiment.

4. Results and Discussion

A spectral image, such as the one illustrated in Figure 2D, was acquired every second, with a spectral resolution of 12 pm and a spatial resolution of 5 µm. The resonance wavelength λ_r appears as a bright peak at a given x-position, and was calculated as the weighted average $\lambda_r(x) = \sum \lambda_i I_i / \sum I_i$, after values of $I < 0.5(I_{\max} + I_{\min})$ had been set to zero. Resonance peaks at two representative positions are shown in Figure 2E. By probing the resonance peak at all 100 positions monitored simultaneously by the imaging spectrometer, a diffusion profile of the shape illustrated in Figure 2F was obtained every second.

Due to the no-slip boundary condition, at the stagnation point $y = 0$ where the two streams meet, the flow velocity v_y will be zero. At a certain distance y_L known as the entrance length, the normal parabolic flow profile will have developed to 99%. It is thus important that measurements be made well downstream from y_L, but as it is typically on the order of 100 µm [6], this is rarely a problem in practice. All measurements were performed at $y_{\text{glucose}} = 19.1$ mm and $y_{\text{BSA}} = 18.1$ mm for the two sample liquids, thus avoiding entrance effects.

The resonance wavelength distribution $\lambda_r(x)$ of each frame can be combined to form a kymograph displaying time on the first axis, as shown in Figure 3. It is evident that the RI boundary becomes sharper when the pressure difference increases, which decreases the time for diffusion and thus diffusion length. The figure also indicates the reference signals when the channel is entirely filled with sample or buffer, respectively. As the sharp boundaries on the temporal axis indicate, steady state is rapidly achieved. At the lowest flow rate shown here ($Q = 19.1$ nL/s), the convection time is $t_{\text{conv}} = ywh/Q = 9.15$ s. Following a change in flow rate, a delay of $t > t_{\text{conv}}$ should thus be permitted to ensure steady state. By temporal averaging of the resonance wavelengths within each section, steady-state diffusion profiles are obtained for various flow rates, as shown for glucose and BSA in Figure 4.

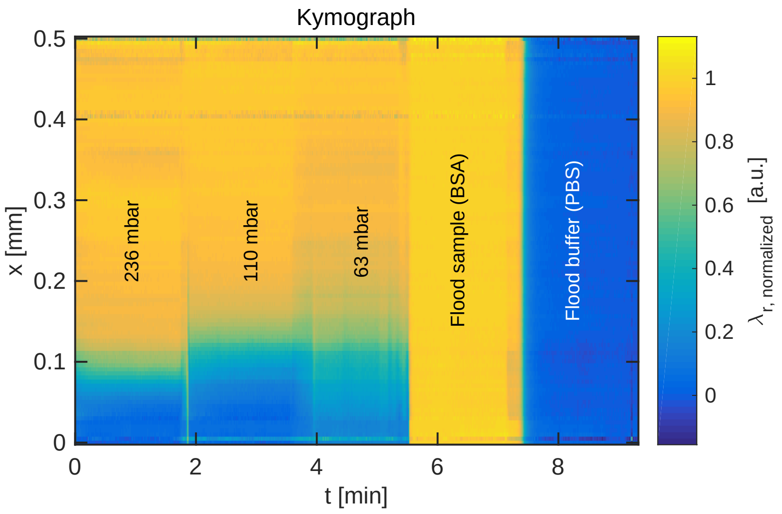

Figure 3. Kymograph of BSA diffusion experiment, obtained by end-to-end fusing the resonance wavelength distribution for each frame. The color corresponds to resonance wavelength shift normalized to the reference values in pure PBS buffer ($\lambda_r = 0$) and pure BSA ($\lambda_r = 1$). The sharpness of the transition increases with measured pressure.

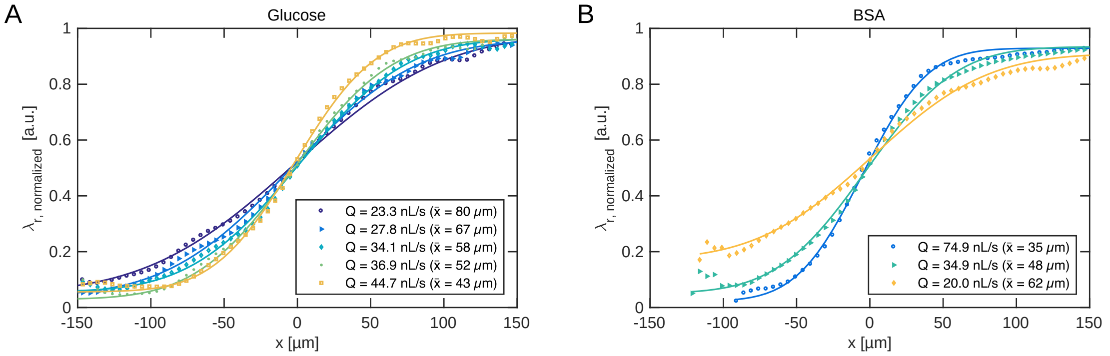

Figure 4. Experimental diffusion profiles for (**A**) glucose and (**B**) BSA. Higher flow rates (Q in the legends) lead to sharper transition (smaller $\bar{x}$) at a given downstream position. Solid lines indicate best fits to Equation (1).

Fitting Equation (1) to the experimentally obtained diffusion profiles directly reveals diffusion length $\bar{x}$, which governs the separation efficiency of the H-filter. The ability to monitor the extent of diffusion in real-time allows the operator to adjust flow conditions during an experiment, rather than waiting for results of a subsequent off-line analysis to determine whether the conditions were in fact suitable. Often such adjustments must otherwise be made “in the dark” for real samples, which may neither be absorbing nor fluorescing, as usually the diffusion boundary cannot be visualized.

For complex samples, such as mixtures of protein fragments, each different component would exhibit a size-dependent diffusion, and the measured refractive index profile would comprise a superposition of multiple error functions Equation (1). An analysis of the concentration gradient would reveal an average diffusion length, which may be sufficient for certain applications.

To summarize, a PCSS-embedded microfluidic H-filter was presented, which enables label-free, real-time monitoring of concentration gradients. As a proof of concept, the device was used to monitor diffusion of glucose and BSA, and the diffusion length in response to various flow rates was determined. This upgrade to a classic microfluidic component could enable many new applications previously precluded by the need for samples to be fluorescing or absorbing. The demonstrated sensor-integrated optofluidic device enables informed decision-making on the basis of diffusion-length, which could further act as input for an automated feedback loop. In this work we focus on measuring diffusion length. This could be extended to determining diffusion constants. However, for high-viscosity samples, the mutual diffusion coefficient would obtain a spatial dependence, which could be the topic of future investigations.

Acknowledgments: The authors gratefully acknowledge funding from the Danish Council for Strategic Research, DSF, under Grant Agreement No. 10-092322 (PolyNano).

Author Contributions: K.T.S. conceived, designed, and performed the experiments, analyzed the data and wrote the paper, A.K. supervised the work and corrected the paper.

Conflicts of Interest: The authors declare no conflict of interest.

References

1. Bujacz, A. Structures of bovine, equine and leporine serum albumin. *Acta Crystallogr. Sect. D Biol. Crystallogr.* **2012**, *68*, 1278–1289.
2. Weigl, B.H.; Yager, P. Microfluidic Diffusion-Based Separation and Detection. *Science* **1999**, *283*, 346–347.
3. Brody, J.P.; Yager, P.; Goldstein, R.E.; Austin, R.H. Biotechnology at low Reynolds numbers. *Biophys. J.* **1996**, *71*, 3430–3441.
4. Brody, J.P.; Yager, P. Diffusion-based extraction in a microfabricated device. *Sens. Actuators A* **1997**, *58*, 13–18.
5. Kamholz, A.E.; Yager, P. Theoretical analysis of molecular diffusion in pressure-driven laminar flow in microfluidic channels. *Biophys. J.* **2001**, *80*, 155–160.
6. Kamholz, A.E.; Weigl, B.H.; Finlayson, B.A.; Yager, P. Quantitative analysis of molecular interaction in a microfluidic channel: The T-sensor. *Anal. Chem.* **1999**, *71*, 5340–5347.
7. Maruyama, T.; Kaji, T.; Ohkawa, T.; Sotowa, K.I.; Matsushita, H.; Kubota, F.; Kamiya, N.; Kusakabe, K.; Goto, M. Intermittent partition walls promote solvent extraction of metal ions in a microfluidic device. *Analyst* **2004**, *129*, 1008–1013.
8. Ciceri, D.; Perera, J.M.; Stevens, G.W. The use of microfluidic devices in solvent extraction. *J. Chem. Technol. Biotechnol.* **2014**, *89*, 771–786.
9. Zheng, W.C.; Xie, R.; He, L.Q.; Xi, Y.H.; Liu, Y.M.; Meng, Z.J.; Wang, W.; Ju, X.J.; Chen, G.; Chu, L.Y. Enhanced H-filter based on fåhræus-Lindqvist effect for efficient and robust dialysis without membrane. *Biomicrofluidics* **2015**, *9*, 044112.
10. Ferrigno, R.; Stroock, A.D.; Clark, T.D.; Mayer, M.; Whitesides, G.M. Membraneless vanadium redox fuel cell using laminar flow. *J. Am. Chem. Soc.* **2002**, *124*, 12930–12931.
11. Costin, C.D.; Synovec, R.E. A Microscale-Molecular Weight Sensor: Probing Molecular Diffusion between Adjacent Laminar Flows by Refractive Index Gradient Detection. *Anal. Chem.* **2002**, *74*, 4558–4565.
12. Golden, J.P.; Justin, G.A.; Nasir, M.; Ligler, F.S. Hydrodynamic focusing—A versatile tool. *Anal. Bioanal. Chem.* **2012**, *402*, 325–335.
13. Kuntaegowdanahalli, S.S.; Bhagat, A.A.S.; Kumar, G.; Papautsky, I. Inertial microfluidics for continuous particle separation in spiral microchannels. *Lab Chip* **2009**, *9*, 2973–2980.
14. Hermannsson, P.G.; Sørensen, K.T.; Vannahme, C.; Smith, C.L.; Klein, J.J.; Russew, M.M.; Grützner, G.; Kristensen, A. All-polymer photonic crystal slab sensor. *Opt. Express* **2015**, *23*, 16529–16539.
15. Magnusson, R.; Wang, S.S. New principle for optical filters. *Appl. Phys. Lett.* **1992**, *61*, 1022–1024.
16. Magnusson, R.; Shokooh-Saremi, M. Physical basis for wideband resonant reflectors. *Opt. Express* **2008**, *16*, 3456–3462.
17. Bougot-Robin, K.; Li, S.; Zhang, Y.; Hsing, I.M.; Benisty, H.; Wen, W. "Peak tracking chip" for label-free optical detection of bio-molecular interaction and bulk sensing. *Analyst* **2012**, *137*, 4785–4794.
18. Cunningham, B.T. Label-Free Assays on the BIND System. *J. Biomol. Screen.* **2004**, *9*, 481–490.
19. Orgovan, N.; Kovacs, B.; Farkas, E.; Szabó, B.; Zaytseva, N.; Fang, Y.; Horvath, R. Bulk and surface sensitivity of a resonant waveguide grating imager. *Appl. Phys. Lett.* **2014**, *104*, 083506.

20. Nazirizadeh, Y.; Behrends, V.; Prosz, A.; Orgovan, N.; Horvath, R.; Ferrie, A.M.; Fang, Y.; Selhuber-Unkel, C.; Gerken, M. Intensity interrogation near cutoff resonance for label-free cellular profiling. *Sci. Rep.* **2016**, *6*, 1–6.
21. Hermannsson, P.G.; Vannahme, C.; Smith, C.L.C.; Kristensen, A. Absolute analytical prediction of photonic crystal guided mode resonance wavelengths. *Appl. Phys. Lett.* **2014**, *105*, 071103, doi:10.1063/1.4893664.
22. Vannahme, C.; Leung, M.C.; Richter, F.; Smith, C.L.C.; Hermannsson, P.G.; Kristensen, A. Nanoimprinted distributed feedback lasers comprising TiO_2 thin films: Design guidelines for high performance sensing. *Laser Photonics Rev.* **2013**, *7*, 1036–1042.
23. Ismagilov, R.F.; Stroock, A.D.; Kenis, P.J.A.; Whitesides, G.; Stone, H.A. Experimental and theoretical scaling laws for transverse diffusive broadening in two-phase laminar flows in microchannels. *Appl. Phys. Lett.* **2000**, *76*, 2376–2378,
24. Bruus, H. *Theoretical Microfluidics*; Oxford University Press: Oxford, UK, 2007; p. 45.
25. Glover, F.A.; Goulden, D.S. Relationship between refractive index of solutions. *Nature* **1963**, *200*, 1165–1166.

(12) INTERNATIONAL APPLICATION PUBLISHED UNDER THE PATENT COOPERATION TREATY (PCT)

(19) World Intellectual Property Organization
International Bureau

(43) International Publication Date
3 August 2017 (03.08.2017)

WIPO | PCT

(10) International Publication Number
WO 2017/129196 A1

---

(51) International Patent Classification:
G01N 21/77 (2006.01) ***G02B 1/00*** (2006.01)
G01N 21/25 (2006.01) ***G02B 6/122*** (2006.01)
G01N 21/41 (2006.01) ***B01L 3/00*** (2006.01)

(21) International Application Number: PCT/DK2017/050018

(22) International Filing Date: 26 January 2017 (26.01.2017)

(25) Filing Language: English

(26) Publication Language: English

(30) Priority Data:

16152817.9	26 January 2016 (26.01.2016)	EP
PA 2016 70814	14 October 2016 (14.10.2016)	DK
16194025.9	14 October 2016 (14.10.2016)	EP

(71) Applicant: DANMARKS TEKNISKE UNIVERSITET [DK/DK]; Anker Engelunds Vej 101 A, 2800 Kgs. Lyngby (DK).

(72) Inventors: KRISTENSEN, Anders; Harsdorffsvej 6B, st.tv., 1874 Frederiksberg C (DK). **SØRENSEN, Kristian Tølbøl**; Bülowsvej 24B, 2.tv., 1870 Frederiksberg C (DK). **HØJLUND-NIELSEN, Emil**; Victor Bendix Gade 20, 4.tv., 2100 Copenhagen Ø (DK).

(74) Agent: PLOUGMANN VINGTOFT A/S; Rued Langgaards Vej 8, 2300 Copenhagen S (DK).

(81) Designated States *(unless otherwise indicated, for every kind of national protection available)*: AE, AG, AL, AM, AO, AT, AU, AZ, BA, BB, BG, BH, BN, BR, BW, BY, BZ, CA, CH, CL, CN, CO, CR, CU, CZ, DE, DJ, DK, DM, DO, DZ, EC, EE, EG, ES, FI, GB, GD, GE, GH, GM, GT, HN, HR, HU, ID, IL, IN, IR, IS, JP, KE, KG, KH, KN, KP, KR, KW, KZ, LA, LC, LK, LR, LS, LU, LY, MA, MD, ME, MG, MK, MN, MW, MX, MY, MZ, NA, NG, NI, NO, NZ, OM, PA, PE, PG, PH, PL, PT, QA, RO, RS, RU, RW, SA, SC, SD, SE, SG, SK, SL, SM, ST, SV, SY, TH, TJ, TM, TN, TR, TT, TZ, UA, UG, US, UZ, VC, VN, ZA, ZM, ZW.

(84) Designated States *(unless otherwise indicated, for every kind of regional protection available)*: ARIPO (BW, GH, GM, KE, LR, LS, MW, MZ, NA, RW, SD, SL, ST, SZ, TZ, UG, ZM, ZW), Eurasian (AM, AZ, BY, KG, KZ, RU, TJ, TM), European (AL, AT, BE, BG, CH, CY, CZ, DE, DK, EE, ES, FI, FR, GB, GR, HR, HU, IE, IS, IT, LT, LU, LV, MC, MK, MT, NL, NO, PL, PT, RO, RS, SE, SI, SK, SM, TR), OAPI (BF, BJ, CF, CG, CI, CM, GA, GN, GQ, GW, KM, ML, MR, NE, SN, TD, TG).

Published:

— *with international search report (Art. 21(3))*

— *before the expiration of the time limit for amending the claims and to be republished in the event of receipt of amendments (Rule 48.2(h))*

---

(54) Title: CUVETTE AND METHOD FOR MEASURING REFRACTIVE INDEX IN A SPECTROPHOTOMETER

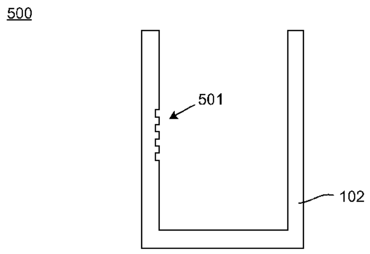

Fig. 5

(57) Abstract: Embodiments of the present invention include a cuvette (100) for use in determining a refractive index of a sample matter in a spectrophotometer (600), the cuvette comprising a container (102) for holding the sample matter, the container (102) having an entry window (121) that allows input radiation to reach the sample matter, the container furthermore having an exit window (122) that allows a part of the input radiation to exit the container part, the entry window and the exit window defining a radiation path; and comprising a photonic crystal (101) rigidly attached to the container or integrally formed in the container and arranged in the radiation path, the photonic crystal having a grating part (111) causing a reflectance spectrum of the photonic crystal to exhibit a resonance. A spectrophotometer is also provided.

WO 2017/129196 A1

Cuvette and method for measuring refractive index in a spectrophotometer

Background of the invention

Spectrophotometers are ubiquitous in science, technology, education and medicine, and can generally measure absorbance of for instance a liquid as a function of wavelength. The liquid is contained in a so-called cuvette, which can be made for instance from polymer, glass or quartz. The cuvette is placed into a slot in the spectrophotometer. By correlating the resulting absorption spectrum to a known calibration curve for a specific compound, the concentration of that compound can easily be calculated using Lambert-Beers law.

However, for non-absorbing compounds, spectrophotometers are not usually suitable for determining concentrations. An alternative method to determining concentrations uses a refractometer, which measures refractive index of the liquid. However, such equipment can be expensive and is much less common. In particular, refractometers that can measure at multiple wavelengths are prohibitively expensive. Since concentration of a specific compound in e.g. a liquid sample is often correlated with the index of refraction of the liquid sample including the compound, a calibration for that specific compound in the liquid can be used to obtain the concentration based on a measurement of the index of refraction.

Summary of the invention

A first aspect of the present invention provides a cuvette for use in determining a refractive index of a matter sample in a spectrophotometer. The cuvette comprises

- a container for holding the matter sample, the container having an entry window that allows input radiation to reach the matter sample, the container furthermore having an exit window that allows a part of the input radiation to exit the container part, the entry window and the exit window defining a radiation path,
- a photonic crystal rigidly attached to a side of the container or integrally formed in a side of the container and arranged in the radiation path, the photonic

crystal having a grating part causing a reflectance spectrum of the photonic crystal to exhibit a resonance.

Such a cuvette is useful for determining for instance a refractive index of a matter sample, such as a liquid sample, or a concentration of a compound in a liquid.

The fact that the photonic crystal is arranged in the side of the container means that at least some precipitates in a matter sample can settle at the bottom of the cuvette where they do not interfere with input radiation, whereby they in turn do not influence measurements.

Cuvettes having a photonic crystal arranged at the bottom of their container part are unable to provide this very important effect.

The grating part may have a uniform grating. Alternatively or additionally, the grating is pseudo-periodic. Alternatively or additionally, the grating part has a chirped grating part. In some embodiments, the grating part has two or more sections having different grating structures. For instance, a first section has a first grating period and a second section has a second grating period different from the first grating period. The grating part may have further sections.

Having multiple sections allows for a method of determining a dispersion of a compound, comprising: measuring a refractive index at least at a first and a second resonance wavelength in a photonic crystal comprising at least the first and second sections, and optionally further sections, just described.

In some embodiments, the grating part comprises a one-dimensional grating. Some embodiments comprise a two-dimensional grating in the grating part. Some embodiments comprise a three-dimensional grating in the grating part.

Preferably, the cuvette is suitable for use in a spectrophotometer.

In some embodiments, the grating part is formed at least partially from a polymer material. The polymer could be PMMA, EFiRon, or HI01XP, or equivalent or similar polymers.

Some embodiments of the first aspect are suitable for existing spectrophotometers, the container is preferably of a size suitable for existing spectrophotometers. In some embodiments, the cuvette has a footprint of 12.5 mm x 12.5 mm. In other embodiments, the cuvette is cylindrical to suit cuvette receptacles in spectrophotometers having a cylindrical receptacle. Preferably the cuvette has a square footprint, since this allows the cuvette to accurately be inserted in two ways in the spectrophotometer: 1) The photonic crystal is in the radiation path of the spectrophotometer light source, 2) The photonic crystal is not in the radiation path of the spectrophotometer light source. This is obtained simply by rotating the cuvette with respect to the spectrophotometer's cuvette receptacle. In some embodiments, absorption and refractive index can be determined simultaneously in one measurement.

In some embodiments, the grating part is a planar grating and the photonic crystal is arranged so that the planar grating is normal to the radiation path. This enables normal radiation incidence, which often provides the most efficient coupling of the radiation into the matter sample.

Some embodiments comprise a polarization filter at the entry window. Some embodiments comprise polarization filter at the exit window. This may for instance prevent mixing of TE and TM polarization specific features such as resonances, in the spectrum, making them simpler to interpret. In some embodiments, the grating part is a planar grating and the photonic crystal is arranged so that a normal to the planar grating is within 10 degrees of a normal to a surface part of the container to which the photonic crystal is attached. In some embodiments, the normal is within 20 degrees. In some embodiments, the normal is within 45 degrees.

In some embodiments, the cuvette is configured so that the radiation path coincides with a path followed by radiation from a spectrophotometer light source in a spectrophotometer in which the cuvette is suitable.

A second aspect provides a spectrophotometer for characterizing a refractive index of a matter sample. The spectrophotometer comprises

- a cuvette receptacle configured to receive a cuvette in accordance with an embodiment in accordance with the first aspect of the invention,
- a spectrophotometer light source arranged to provide input radiation along the radiation path of the cuvette,
- a spectrometer arranged to receive non-absorbed parts of the input radiation from the exit window and to determine a spectrum based on said non-absorbed parts, and to determine a resonance wavelength or resonance frequency or other resonance property in the spectrum,

the spectrophotometer being configured to determine the refractive index by solving a set of suitable optical equations that take into account at least 1) optical and physical characteristics of the photonic crystal, 2) the determined resonance wavelength or resonance frequency or said other resonance property, the refractive index being an unknown to be solved for in said set of suitable equations.

The skilled person will readily appreciate that "a set of suitable optical equations" means a set of equations or other model or empirical formulation that allows for determining the refractive index based on the optical elements involved, including the cuvette and ultimately a matter sample held by the cuvette. The selection of equations may be selected based for instance on limitations in available computing power (more complex equations typically require more computing power), and/or be selected based on the precision required of the solution representing the refractive index (more detailed models may give a more precise result, whereas approximations and simple models may lead to a less precise result). Accordingly, many different implementations can be applied in respect of the set of suitable optical equations. Among other sources, textbooks and scientific papers are available that will readily allow the person skilled in the art to provide a set of suitable optical equations that may be used in methods and apparatuses disclosed in the present specification.

As is evident for the person skilled in the art, the set of equations may comprise an analytical or a semi-analytical expression or experimentally determined relationship between relevant parameters.

In some embodiments, two or more spectral components in the spectrum are measured in the spectrophotometer and used to characterize the resonance, and in particular used as input to the set of optical equations in order to solve for the refractive index – described above – or other relevant characteristic. This allows for a determination that, to lesser or greater extent – take into account a shape of the resonance, such as a peak-to-width property determined based on the measured values. Alternatively or additionally, the model may compare an amplitude or equivalent value of each of a plurality of measured spectral components with an expected value (in relative terms) for said each spectral component, for instance as predicted by an at least partly analytical model and/or an at least partly semi-analytical model, or based at least partly on a table of expected values. An asymmetry in the resonance, determined based on measured spectral components, can in some cases be used to determine the relevant parameter, such as the refractive index, as part of the set of optical equations.

In some embodiments, the spectrophotometer further comprises a mirror system configured to guide input light reflected by the photonic crystal to the spectrometer.

A third aspect provides a method for determining a refractive index of a matter sample in a spectrophotometer. The method comprises

- inserting a cuvette in accordance with an embodiment of the first aspect of the invention into a cuvette receptacle of a suitable spectrophotometer, the cuvette comprising the matter sample,
- irradiating the matter sample with input radiation along the radiation path,
- recording a spectrum of non-absorbed parts of the input radiation using the spectrometer,
- determining the refractive index of the matter sample by solving a set of suitable optical equations that take into account at least 1) optical and physical characteristics of the photonic crystal, 2) the determined resonance wavelength or resonance frequency, the refractive index being an unknown to be solved for in said set of suitable equations.

In an aspect, the invention also provides, more generally: A method for determining an optical characteristic or material characteristic of a matter sample in a spectrophotometer, the method comprising

- inserting a cuvette in accordance with an embodiment of the first aspect of the invention into a cuvette receptacle of a suitable spectrophotometer, the cuvette comprising the matter sample,
- irradiating the matter sample with input radiation along the radiation path,
- recording a spectrum of non-absorbed parts of the input radiation using the spectrometer,
- determining said characteristic of the matter sample by solving a set of suitable optical equations that take into account at least 1) optical and physical characteristics of the photonic crystal, 2) a determined resonance wavelength or resonance frequency or other resonance property of the spectrum, said characteristic being an unknown to be solved for in said set of suitable equations.

In some embodiments, the characteristic is a refractive index of the material, and the method is accordingly adapted to solve for the refractive index.

In some embodiments, the characteristic is a concentration of the material in the matter sample. The set of suitable optical equations further comprises a predetermined relationship for converting, for said material, a resonance wavelength or resonance frequency determined by the spectrophotometer into a concentration of said material.

A fourth aspect provides software which, when executed on a digital processor arranged in a suitable spectrophotometer, enables the spectrophotometer to perform the irradiating, recording and determining steps in embodiments of a method aspect of the present invention, such as the third aspect or the more general aspect for determining an optical characteristic or a material characteristic.

A fifth aspect provides a spectrophotometer for determining a concentration of a material in a matter sample. The spectrophotometer comprises

- a cuvette receptacle configured to receive a cuvette in accordance with an embodiment in accordance with the first aspect of the invention,

- a spectrophotometer light source arranged to provide input radiation along the radiation path of the cuvette,
- a spectrometer arranged to receive non-absorbed parts of the input radiation from the exit window and to determine a spectrum based on said non-absorbed parts, and to determine a resonance wavelength or resonance frequency or other resonance property in the spectrum,

the spectrophotometer further being configured to determine the concentration by solving a set of suitable optical equations that take into account at least 1) optical and physical characteristics of the photonic crystal, 2) the determined resonance wavelength or resonance frequency or said other resonance property, 3) a predetermined relationship for converting, for said material, a resonance wavelength or resonance frequency or other resonance property determined by the spectrophotometer into a concentration of said material.

The material may be a single chemical compound or mix of multiple compounds, fluids (both liquid and gaseous), polymer or polymers; biological or synthetic fluid or fluids; acid or acids; base or bases; raw or pre-processed materials, or any other material that is suitable for being a least partly characterized using a spectrophotometer. In any case, the material may be liquid or solid, or a mixture thereof, whether it comprises one or several different materials, such as the ones mentioned in the present paragraph or elsewhere in the present specification. In some cases, certain materials falling within the group of materials described above are not suitable, at least for some concentrations within the matter sample, for being characterized in a spectrophotometer. Embodiments of spectrophotometers in accordance with the present invention may or may not be able to overcome such limitations.

In some embodiments of the fifth aspect, the spectrophotometer comprises a selector unit allowing a user to select between at least two different materials or mixture of materials, and in response, the spectrophotometer determines the concentration by using the predetermined relationship corresponding to the selected material or mixture of materials.

In some embodiments, the predetermined relationship for the material the concentration of which is to be determined, represents the relationship for the material mixed in a (substantially) known medium, such as but not limited to: water, alcohol, acid or acids, base or bases, or other medium, fluid or solid, or a mix of such materials.

The discussion above relating to "a set of suitable optical equations" applies equally to the fifth aspect and any other aspects that involve such a set of suitable optical equations. Persons skilled in the art will also appreciate that similar considerations apply to the "predetermined relationship".

A sixth aspect provides a method for manufacturing a cuvette in accordance with an embodiment of the first aspect of the invention. The method comprises:

- providing a cuvette having a container part for holding a fluid sample,
- providing a photonic crystal having a first side with a grating part,
- adding curable liquid to the photonic crystal on a side opposite the first side, or to part of an inside of the container part,
- positioning the crystal with curable liquid inside the container part in a position with the curable liquid in contact with the inside of the container part, in a position where a fluid sample can get into contact with the photonic crystal,
- curing the curable liquid by exposing it to curing radiation, whereby the photonic crystal becomes rigidly attached to the container part.

In a seventh aspect, the invention provides a method for manufacturing a cuvette in accordance with an embodiment of the first aspect of the invention. The method comprises:

- providing a photonic crystal having a first side having a grating part, and having a second side opposite the first side,
- providing a cuvette mold having a first mold part defining an inside surface of the cuvette and having a second mold part defining an outside surface of the cuvette,
- arranging and maintaining the photonic crystal with the first side facing the first mold part in a position corresponding to a cuvette side wall,

- filling the mold with cuvette material, whereby the photonic crystal becomes partly embedded in the cuvette due to the cuvette material getting into contact at least with the second side of the photonic crystal.

The photonic crystal can for instance be maintained in the position by using a cuvette mold having a hole in the first mold part and providing suction at the hole and placing, before or after providing the suction, the photonic crystal at the hole with the first side of the photonic crystal facing the hole. Alternatively, the photonic crystal is held in position by an adhesive. When the first mold part is removed, the adhesive can be removed from the grating part.

The cuvette material is preferably made of a polymer, such as polystyrene poly(methyl methacrylate), polypropylene or polycarbonate.

An eighth aspect of the invention provides a method for manufacturing a cuvette in accordance with an embodiment of the first aspect of the invention. The method comprises:

- providing a first cuvette part having a slab with an in-plane photonic crystal with a grating part at a first side of the slab, the slab corresponding to at least a part of a side wall of the cuvette,
- providing a second cuvette part having an opening corresponding to a size of the slab,
- arranging the slab in the opening with the grating part facing an inside of the cuvette,
- establishing a seal between the slab and the second cuvette part.

Often, the cuvette has a square footprint. In that case, the slab could constitute an entire side wall of the cuvette, or it could be a part of a side wall.

The slab and second cuvette parts are sealed together for instance by adhesion bonding, ultrasonic bonding or thermal bonding.

Brief description of the drawings

Figure 1 illustrates a cuvette in accordance with an embodiment of the invention.

Figure 2 illustrates a radiation path in a cuvette in accordance with an embodiment of the invention for a transmission measurement.

Figure 3 shows measurement of spectra for a prior art cuvette and a cuvette in accordance with an embodiment of the invention.

Figure 4 illustrates a radiation path in a cuvette in accordance with an embodiment of the invention for a reflection measurement.

Figure 5 illustrates a photonic crystal integrally formed with a container.

Figure 6 illustrates schematically a spectrophotometer in accordance with an embodiment of the invention.

Figure 7 illustrates schematically a photonic crystal suitable for use in a cuvette in accordance with an embodiment of the invention.

Figure 8 illustrates a method for determining a refractive index of a sample using a cuvette in a spectrometer.

Figure 9 illustrates two methods of fabricating photonic crystals suitable for use in a cuvette in accordance with an embodiment of the invention.

Figure 10 illustrates an embodiment of a method of manufacturing a cuvette.

Detailed description of selected embodiments

Fig. 1 illustrates a cuvette in accordance with an embodiment of the present invention. It has a container 102 for holding a sample, such as a fluid sample. Inside the container is a photonic crystal 101 that has been attached to the container. The photonic crystal comprises a grating part 111 and a substrate part

112. In this specification, the cuvette will be referred to as a nanocuvette, due to the presence of the grating in the cuvette. For many applications, a typical grating period is on the nanometer-scale, such as in the range 100 nm to 1000 nm.

The container part has an entry window 121 and an exit window 122. Input radiation can enter the entry window in order to reach the fluid sample. There, the radiation interacts with the photonic crystal and the fluid, while propagating towards the exit window 122, where it exits the nanocuvette.

Fig. 2 illustrates the radiation path in a nanocuvette used in a transmission-type setup. This is the standard mode of operation in a spectrophotometer. The nanocuvette in Fig. 2 contains a fluid sample that covers the photonic crystal. Input radiation schematically illustrated with dashed arrow 131 enters the cuvette where it propagates through the fluid sample, as illustrated schematically by dashed arrow 133. At the other side of the cuvette, radiation exits the nanocuvette along the radiation path, as schematically illustrated by dashed arrow 132.

The container part may be of a standard size, whereby it can be used in existing spectrometers. When the nanocuvette 100 is used in a spectrophotometer, the transmission spectrum will differ from the transmission spectrum that would be obtained with the same spectrophotometer, had a conventional cuvette been used. The presence of the photonic crystal causes resonant reflection. Light with wavelengths near the resonance wavelength are not transmitted.

The grating part is defined by a periodically varying modulation of the refractive index. The grating part may have recesses that are susceptible to being filled with material with which it is brought into contact, for instance a liquid sample in the container. Thus, when the container 102 is filled with fluid, the photonic crystal recesses will be filled by fluid. Alternatively, the grating part is buried, for instance by a polymer. In yet another embodiment, the grating part is uniform in a direction normal to the grating plane.

The photonic crystal has a resonance wavelength, λ_R, at which normally incident light with a particular polarization, for instance transverse-electric (TE) polarized, is reflected with almost 100 % efficiency. The resonance wavelength depends on the grating characteristics, i.e. the distribution of materials with high and low refractive indices. The photonic crystal resonance can be characterized for instance by determining a transmission spectrum.

When the photonic crystal becomes immersed in fluid, the resonance wavelength shifts depending on the characteristics of the fluid.

Fig.3 shows spectra provided by a Thermo Scientific NanoDrop 2000c spectrophotometer measuring transmitted light through a nanocuvette in accordance with an embodiment of the invention. Fig. 3 shows three spectra measured in the wavelength range 400 nm to 700 nm. The first spectrum is the absorbance for an empty standard cuvette (i.e. a cuvette without a photonic crystal). The measured absorbance data are calibrated so that the absorbance spectrum for the empty cuvette is substantially flat and zero.

Fig. 3 also shows the spectrum for an empty nanocuvette in accordance with an embodiment of the invention. The corresponding graph in Fig. 3 is labeled "NanoCuvette with air". When the cuvette is empty, the photonic crystal is in contact with air, air acting as a fluid sample. (The data in Fig. 3 are the raw data provided by the spectrophotometer.) The spectrum varies substantially across the wavelength range from 400 nm to 700 nm. One feature is a clear resonance near 558 nm, which is the result of resonant reflection by the photonic crystal in contact with the fluid.

Fig. 3 furthermore shows the spectrum when the nanocuvette is filled with water. The water is in contact with the photonic crystal, changing (in this case red-shifting) the resonant reflection wavelength compared to the measurement in air. Accordingly, the spectrum changes from that of the empty nanocuvette. For instance, the resonance moves to a longer wavelength of 581 nm. The general spectral shape is similar for measurements in air and water. The general tendency is that features move to longer wavelengths for higher refractive index of the fluid sample.

By analyzing the spectrum of a filled nanocuvette, it is possible to determine the refractive index of the fluid. This can for instance be done numerically by an iterative process, taking refractive index dispersion of the constituent materials into account. Alternatively, spectrum measurements on a set of refractive index calibration liquids provide references for the relationship between resonance wavelength and refractive index, for one particular photonic crystal. Such relationships are typically non-linear. The references can be used to infer a refractive index for a sample with an unknown refractive index.

Alternatively, the reference data can be provided using computer simulations, where absorbance spectra are calculated for different fluids.

Another method of determining the refractive index of the sample based on the measured absorbance spectrum involves solving a set of electromagnetic equations by digital computer means. The photonic crystal structure is known, whereas the fluid is presumed not to be. The solving amounts to finding a refractive index that gives the resonance seen in the measured spectrum. A person skilled in the art will readily know how to provide equations suitable for obtaining the refractive index. Exemplary suitable equations and underlying principles are described in detail for instance in "Absolute analytical prediction of photonic crystal guided mode resonance wavelengths" (APPLIED PHYSICS LETTERS 105, 071103 (2014)) by Hermannsson et al. In the context of this article, the value to be determined for the purpose of the present invention is the index of the "superstrate". The article "Refractive index dispersion sensing using an array of photonic crystal resonant reflectors" (APPLIED PHYSICS LETTERS 107, 061101 (2015) by Hermannsson et al. describes an example in which an analytical expression is provided for the index of refraction of the "superstrate", see equation (6) therein. This method can be used for the purpose of determining the index of refraction of the liquid sample in the present invention. The two references are hereby incorporated by reference.

To summarize, the inventors have provided a cuvette that makes it possible to determine the index of refraction of a fluid using a standard spectrophotometer and specially configured software adapted to enable the calculations described above.

Fig. 4 illustrates operation in a reflection-type setup. The entry window also acts as exit window. Input radiation, schematically illustrated by dashed arrow 431, enters the nanocuvette through entry window 121 and interacts with the photonic crystal and any fluid in contact with the photonic crystal. Reference number 433 is situated in the region where the interaction is primarily taking place. Instead of, or in addition to, determining the transmitted radiation (arrow 132 in Fig. 2), the reflected radiation, schematically illustrated by dashed arrow 432, can be characterized in a manner similar to that with which the transmitted radiation was characterized, described above. The electromagnetic equations are similar to those used for determining the refractive index in the transmission setup. In the transmission setup, the resonance shows up as a peak in the absorbance spectrum. In the reflection setup, the resonance will show up as a peak in the reflectance spectrum. The purpose of the calculations is to determine that refractive index which, when assumed to be in contact with the photonic crystal and extending away from it on the opposite side of the substrate part 112, results in the resonance seen in the reflectance spectrum.

For illustrative purposes only, the highly schematic illustration of the radiation path in Fig. 4 shows incoming radiation 431 and outgoing radiation 432 as not overlapping. In practice, they overlap in many advantageous embodiments. This would be the case for instance when the input radiation enters the cuvette in a direction normal to the cuvette surface plane and the grating is parallel with the cuvette surface plane. In any case, the dashed arrows illustrating radiation in Figs. 2 and 4 should not be construed as limiting the nanocuvette design or imposing requirement on the method by which the nanocuvette is used.

Fig. 5 illustrates another embodiment of a cuvette 500 in accordance with the invention. In this embodiment, the photonic crystal 501 is an integrated part of the cuvette container 102. As such, the container part 102 acts as a substrate for the grating part. The principles are entirely the same as described above for a photonic crystal 101 attached to the container part 102. Both transmission and reflection setups can be used. The electromagnetic equations are also similar, but take into account the different geometry and material choices.

Fig. 6 illustrates schematically a standard spectrophotometer 600. It has a light source 601, a receptacle 603 for receiving a cuvette, and a spectrometer 605 with a light entry window 606 arranged to receive light from the cuvette, and a microcontroller (MCU) 607. This spectrophotometer also has a display 609 for displaying information related to measurements from the spectrometer. It also has a data interface 611 allowing data to be transferred from the spectrophotometer to another device. It may also be configured to receive data from an external device. This could for instance be software for controlling the operation of the MCU (often referred to as firmware). The data interface may be wireless or configured to be used with a cable.

The spectrometer in Fig. 6 is in accordance with an embodiment of the invention, although this is not readily apparent. The MCU can be specifically configured to be capable of internally performing the calculations described above for determining the refractive index or concentration based on measurements obtained by the spectrometer with a nanocuvette in the receptacle, or the calculation can be done externally after transfer of a measured spectrum.

Fig. 7 illustrates schematically a photonic crystal 700 for use in a cuvette in accordance with an embodiment of the invention. It comprises a low index layer having an index of refraction n_L. There is a substrate part and a grating part on top of the substrate part. The grating part also comprises a high index material having an index of refraction, n_H. Above the grating part, there is a layer of high index material. An example of a photonic crystal is described below. In that example, the substrate part is made of PMMA. The grating is further characterized by a grating height, t_g, a thickness, t_f, of the high index layer, a grating duty cycle, d, and a grating constant, Δ. The grating may be planar, and the dashed line 701 indicates the grating's plane. Fig. 7 also illustrates schematically a "sensing region". This is to indicate that this region, which comprises sample fluid during a measurement, affects the measured index of refraction.

Fig. 8 illustrates a measurement method in accordance with an embodiment of the invention. The method is for obtaining a refractive index of a fluid sample. In step 801, a nanocuvette with a sample is inserted into the receptacle of a spectrophotometer. Then, in step 803, the sample is irradiated by the spectrophotometer light source. Light transmitted through the photonic crystal and fluid sample reaches the spectrometer, where it is characterized. Finally, in step 807, the refractive index is determined based on characteristics of the photonic crystal and on the measured spectrum. The determining is described earlier in this document.

Fig. 9 illustrates a method of fabricating a photonic crystal for use as a photonic crystal in a nanocuvette. Step 1 illustrates the provision of an anti-stiction coated grating master. In step 2, a liquid low refractive index polymer is added on the master. In step 3, a flat transparent substrate, for instance comprising PMMA or glass, is pressed onto the liquid low refractive index polymer. This causes the liquid low refractive index polymer to become flattened. Next, in step 4, radiation is used in order to cure the liquid low refractive index polymer, producing a solid low refractive index polymer layer that is attached to both the master and the substrate. In step 5+6, the anti-stiction coated master is detached from the cured low refractive index polymer layer, exposing the grating structure. In step 7a, TiO_2 is sputtered onto the grating structure. The result is a corrugated top layer.

An alternative nanocuvette fabrication step is illustrated in Fig. 9’s step 7b. Instead of sputtering TiO_2 onto the grating structure, a high refractive index polymer is added on the now-exposed grating structure and spun in order to obtain a flat layer.

Fig. 10 illustrates a method for manufacturing a nanocuvette. The method comprises, in step 1001, providing a cuvette having a container part for holding a fluid sample. In step 1003, a photonic crystal is provided. Curable liquid is then added to the photonic crystal on the side opposite the grating part, in step 1005. Next, in step 1007, the photonic crystal with curable liquid is positioned inside the container part of the cuvette where a fluid sample will get into contact with the photonic crystal. Then, in step 1009, the curable liquid is exposed to curing radiation that cures the curable liquid, whereby the photonic crystal becomes rigidly attached to the container part.

Other embodiments of the manufacturing method include the same steps, but performed in a different order, where possible. Those embodiments are encompassed by the corresponding claim(s).

“Spectrophotometer” shall be construed broadly as being a single apparatus or a collection of two or more separate electrical hardware apparatuses that in combination can carry out one or more of the described methods.

Claims

1. A cuvette for use in determining a refractive index of a matter sample in a spectrophotometer, comprising
   - a container for holding the matter sample, the container having an entry window that allows input radiation to reach the matter sample, the container furthermore having an exit window that allows a part of the input radiation to exit the container part, the entry window and the exit window defining a radiation path,
   - a photonic crystal rigidly attached to a side of the container or integrally formed in a side of the container and arranged in the radiation path, the photonic crystal having a grating part causing a reflectance spectrum of the photonic crystal to exhibit a resonance.

2. A cuvette in accordance with claim 1, wherein the photonic crystal is attached to the side of the container.

3. A cuvette in accordance with claim 1, wherein the photonic crystal is integrally formed in the side of the container.

4. A cuvette in accordance with one of the preceding claims, wherein the cuvette has a square footprint.

5. A cuvette in accordance with claim 4, wherein the cuvette is configured to be insertable into a spectrophotometer in a first configuration and in a second configuration, wherein in the first configuration the photonic crystal is in a radiation path of the spectrophotometer, and in the second configuration the photonic crystal is not in a radiation path of the spectrophotometer.

6. A cuvette in accordance with one of the preceding claims, wherein the grating part is formed at least partially from a polymer material.

7. A cuvette in accordance with one of the preceding claims, wherein the grating part is a planar grating and wherein the photonic crystal is arranged

so that the planar grating is normal to the radiation path.

8. A cuvette in accordance with one of the preceding claims, wherein the grating part is a planar grating and wherein the photonic crystal is arranged so that a normal to the planar grating is within 10 degrees of a normal to a surface part of the container to which the photonic crystal is attached.

9. A cuvette in accordance with one of the preceding claims, wherein the cuvette is configured so that the radiation path coincides with a path followed by radiation from a spectrophotometer light source in a spectrophotometer in which the cuvette is suitable.

10. A spectrophotometer for characterizing a refractive index of a matter sample, comprising
    - a cuvette receptacle configured to receive a cuvette in accordance with one of claims 1-9,
    - a spectrophotometer light source arranged to provide input radiation along the radiation path of the cuvette,
    - a spectrometer arranged to receive non-absorbed parts of the input radiation from the exit window and to determine a spectrum based on said non-absorbed parts, and to determine a resonance wavelength or resonance frequency or other resonance property in the spectrum,

    the spectrophotometer being configured to determine the refractive index by solving a set of suitable optical equations that take into account at least 1) optical and physical characteristics of the photonic crystal, 2) the determined resonance wavelength or resonance frequency or said other resonance property, the refractive index being an unknown to be solved for in said set of suitable equations.

11. A spectrophotometer in accordance with claim 10, further comprising a mirror system configured to guide input light reflected by the photonic crystal to the spectrometer.

12. A method for determining an optical characteristic or material characteristic of a matter sample in a spectrophotometer, comprising
    - inserting a cuvette in accordance with one of claims 1-9 into a cuvette receptacle of a suitable spectrophotometer, the cuvette comprising the matter sample,
    - irradiating the matter sample with input radiation along the radiation path,
    - recording a spectrum of non-absorbed parts of the input radiation using the spectrometer,
    - determining said characteristic of the matter sample by solving a set of suitable optical equations that take into account at least 1) optical and physical characteristics of the photonic crystal, 2) a determined resonance wavelength or resonance frequency or other resonance property of the spectrum, said characteristic being an unknown to be solved for in said set of suitable equations.

13. A method in accordance with claim 12, wherein the characteristic is a refractive index of the material.

14. A method in accordance with claim 12, wherein the characteristic is a concentration of the material in the matter sample, and wherein the set of suitable optical equations further comprises a predetermined relationship for converting, for said material, a resonance wavelength or resonance frequency determined by the spectrophotometer into a concentration of said material.

15. A spectrophotometer for determining a concentration of a material in a matter sample, comprising
    - a cuvette receptacle configured to receive a cuvette in accordance with one of claims 1-9,
    - a spectrophotometer light source arranged to provide input radiation along the radiation path of the cuvette,
    - a spectrometer arranged to receive non-absorbed parts of the input radiation from the exit window and to determine a spectrum based on

said non-absorbed parts, and to determine a resonance wavelength or resonance frequency or other resonance property in the spectrum,

the spectrophotometer further being configured to determine the concentration by solving a set of suitable optical equations that take into account at least 1) optical and physical characteristics of the photonic crystal, 2) the determined resonance wavelength or resonance frequency or said other resonance property, 3) a predetermined relationship for converting, for said material, the resonance wavelength or resonance frequency or said other resonance property determined by the spectrophotometer into a concentration of said material.

16. A spectrophotometer in accordance with claim 15, further comprising a selector unit allowing a user to select between at least two different materials or mixture of materials, and in response, the spectrophotometer determines the concentration by using the predetermined relationship corresponding to the selected material or mixture of materials.

17. Software which, when executed on a digital processor arranged in a suitable spectrophotometer, enables the spectrophotometer to carry out the irradiating, recording and determining steps in accordance with one of claims 9-11.

18. A method for manufacturing a cuvette in accordance with one of claims 1-9, comprising:

- providing a cuvette having a container part for holding a fluid sample,
- providing a photonic crystal having a first side with a grating part,
- adding curable liquid to the photonic crystal on a side opposite the first side, or to part of an inside of the container part,
- positioning the crystal with curable liquid inside the container part in a position with the curable liquid in contact with the inside of the container part, in a position where a fluid sample can get into contact with the photonic crystal,
- curing the curable liquid by exposing it to curing radiation, whereby the photonic crystal becomes rigidly attached to the container part.

19. A method for characterizing a matter sample using a cuvette in accordance with one of claims 1-9 in a spectrophotometer, the cuvette having a square footprint, the method being characterized by steps of:
    - inserting the cuvette into the spectrophotometer in such a way that the photonic crystal is in the radiation path of the spectrophotometer light source, and measuring a reflectance or transmission spectrum of the matter sample and determining a resonance in said reflectance or transmission spectrum,
    - inserting the cuvette into the spectrophotometer in such a way that the photonic crystal is not in the radiation path of the spectrophotometer light source, and performing an absorption measurement on the matter sample.

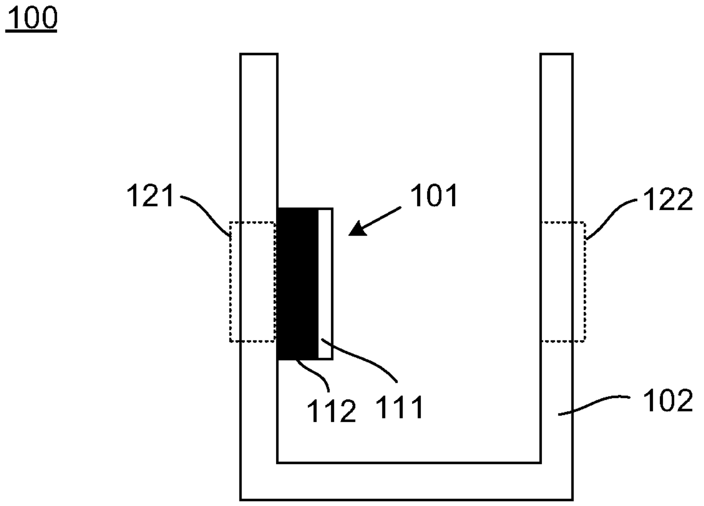
100
121
101
122
112
111
102

Fig. 1

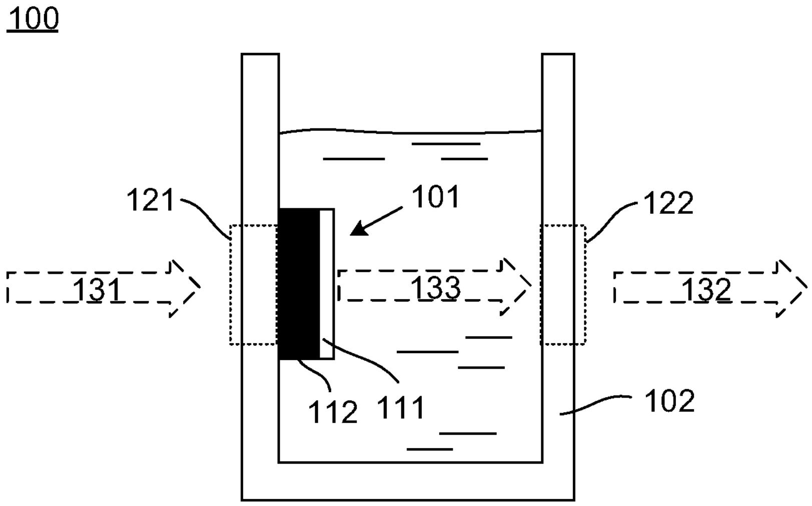
100
121
101
122
131
133
132
112
111
102

Fig. 2

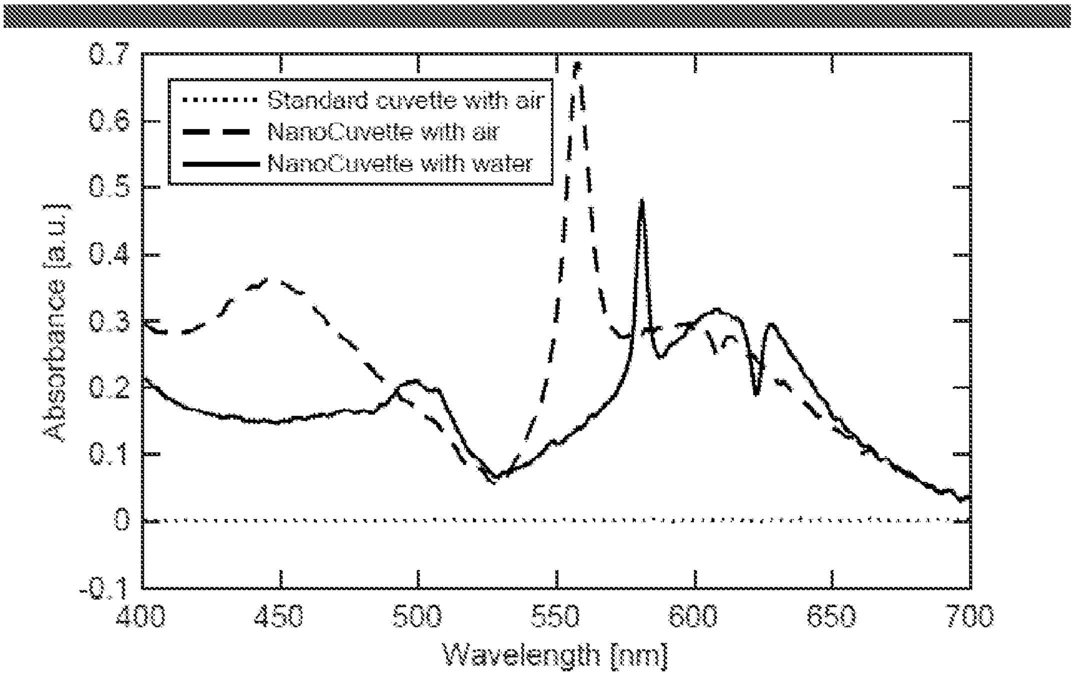
Standard cuvette with air
NanoCuvette with air
NanoCuvette with water
Absorbance [a.u.]
Wavelength [nm]
0.7
0.6
0.5
0.4
0.3
0.2
0.1
0
-0.1
400
450
500
550
600
650
700

Fig. 3

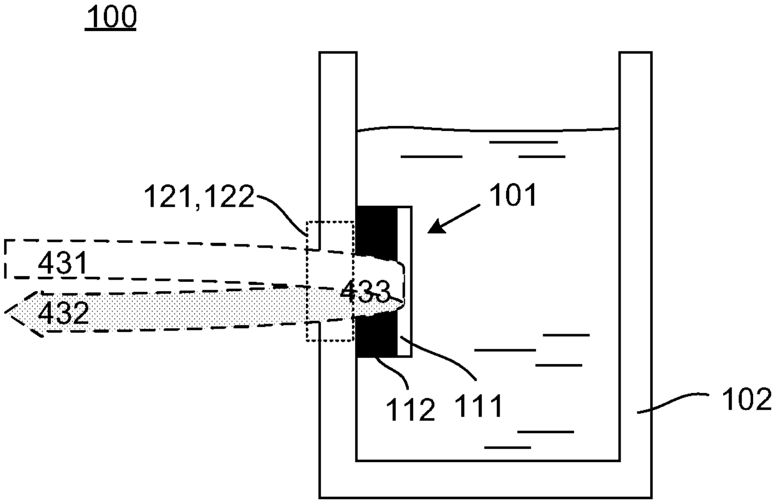
100
121,122
101
431
433
432
112
111
102

Fig. 4

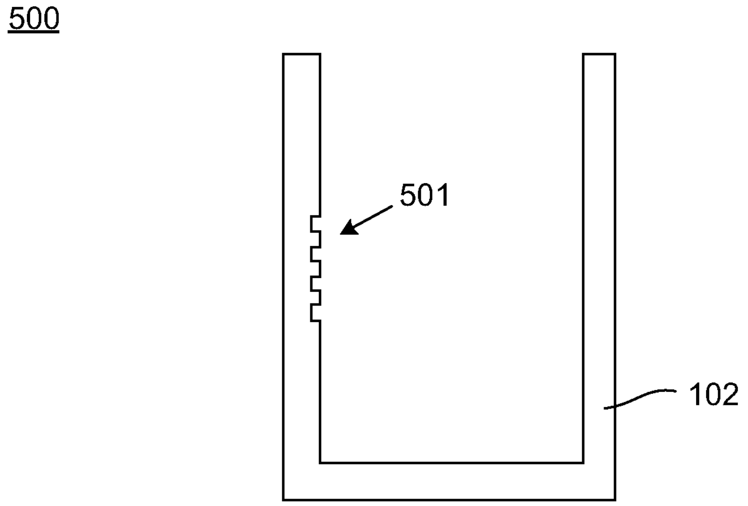

Fig. 5

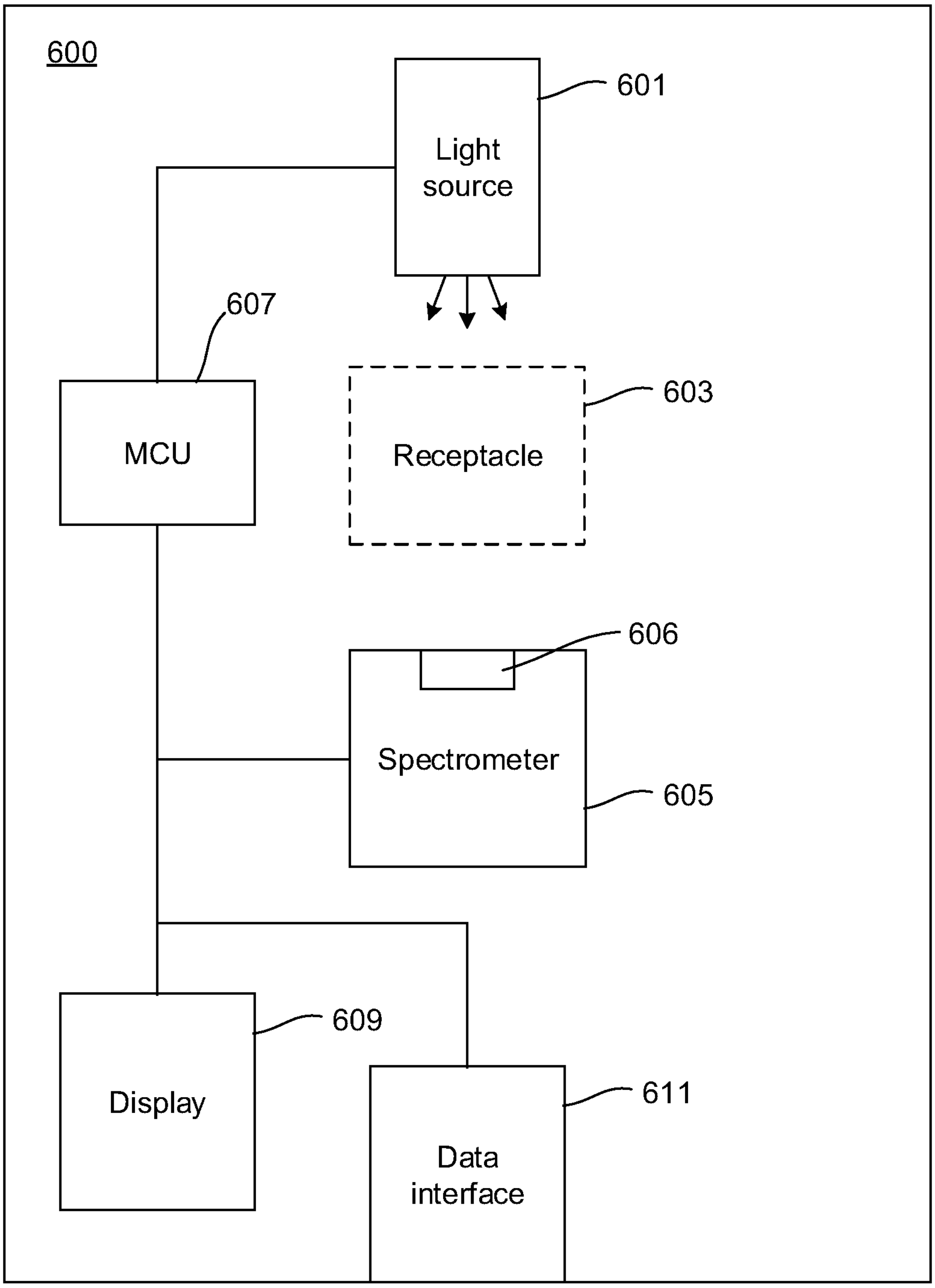
600
Light source
601
607
MCU
Receptacle
603
606
Spectrometer
605
609
Display
611
Data interface

Fig. 6

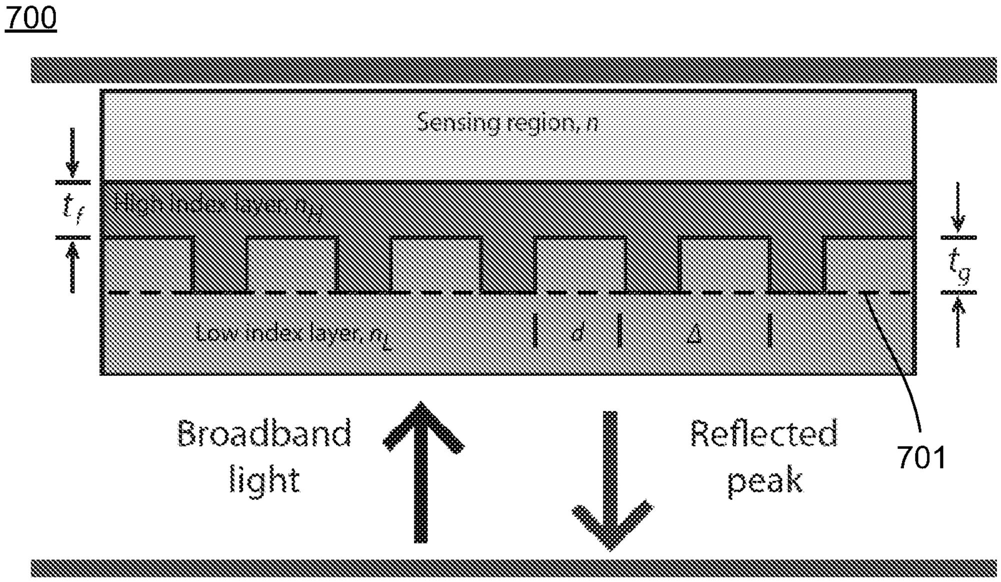
700
Sensing region, n
High index layer, n_H
t_f
t_g
Low index layer, n_L
d
Δ
Broadband light
Reflected peak
701

Fig. 7

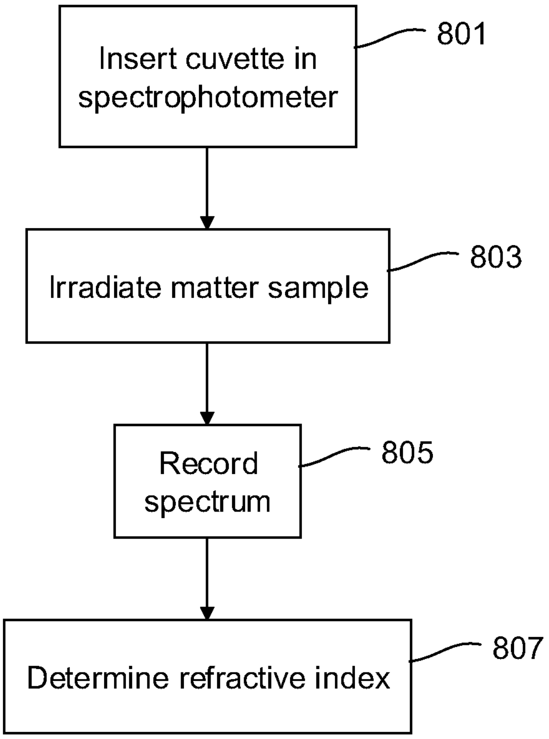
Insert cuvette in spectrophotometer
801
Irradiate matter sample
803
Record spectrum
805
Determine refractive index
807

Fig. 8

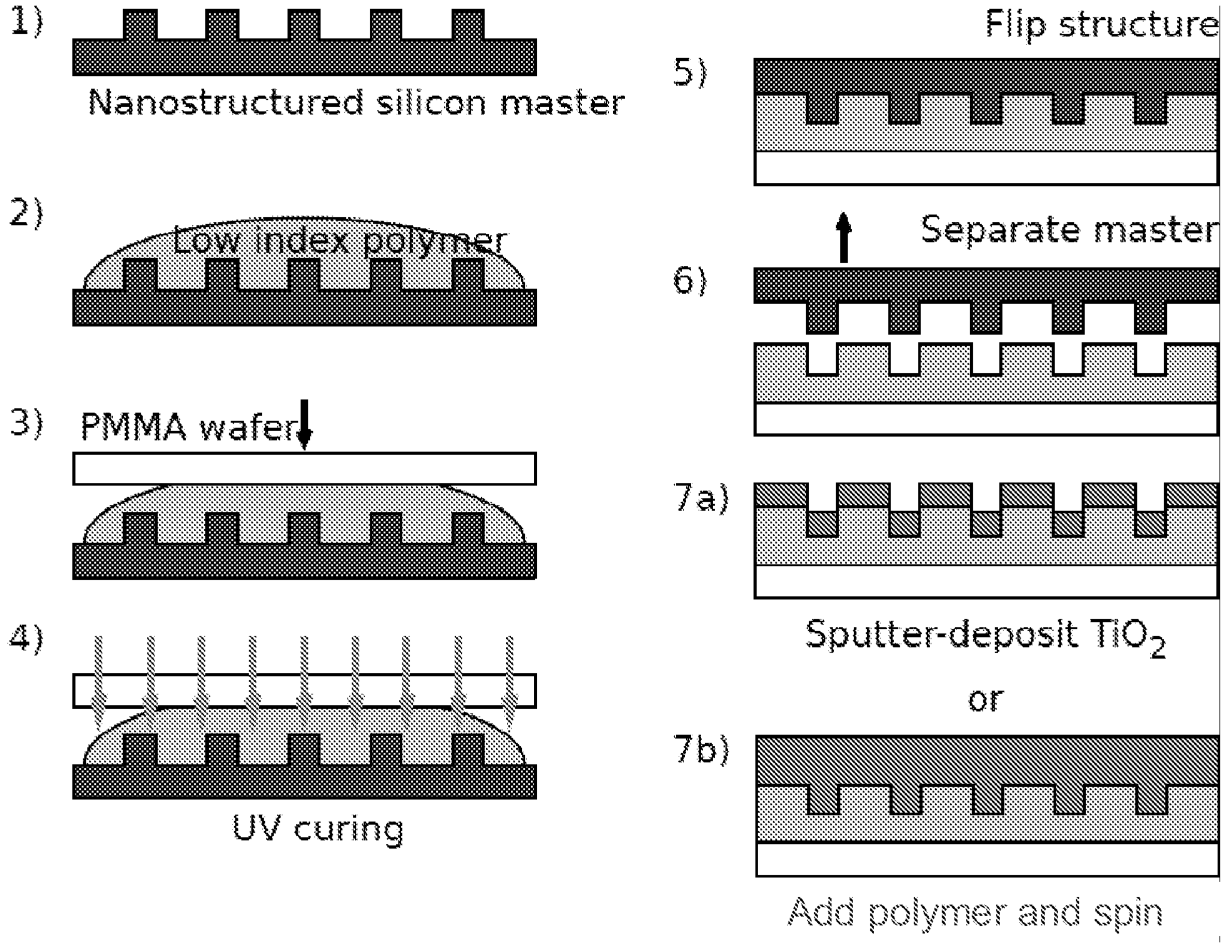
1)
Nanostructured silicon master
2)
Low index polymer
3)
PMMA wafer
4)
UV curing
Flip structure
5)
Separate master
6)
7a)
Sputter-deposit TiO_2
or
7b)
Add polymer and spin

Fig. 9

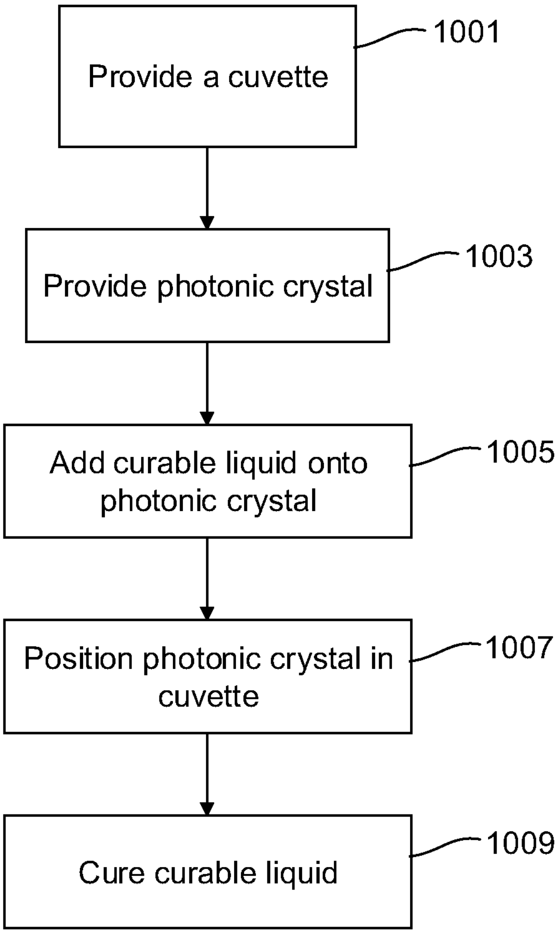
Provide a cuvette
1001
Provide photonic crystal
1003
Add curable liquid onto photonic crystal
1005
Position photonic crystal in cuvette
1007
Cure curable liquid
1009

Fig. 10

INTERNATIONAL SEARCH REPORT

International application No
PCT/DK2017/050018

A. CLASSIFICATION OF SUBJECT MATTER
INV. G01N21/77 G01N21/25 G01N21/41 G02B1/00 G02B6/122
B01L3/00
ADD.

According to International Patent Classification (IPC) or to both national classification and IPC

B. FIELDS SEARCHED

Minimum documentation searched (classification system followed by classification symbols)
G01N B01L G02B

Documentation searched other than minimum documentation to the extent that such documents are included in the fields searched

Electronic data base consulted during the international search (name of data base and, where practicable, search terms used)

EPO-Internal, WPI Data

C. DOCUMENTS CONSIDERED TO BE RELEVANT

Category*	Citation of document, with indication, where appropriate, of the relevant passages	Relevant to claim No.
X	US 2012/309080 A1 (CUNNINGHAM BRIAN T [US] ET AL) 6 December 2012 (2012-12-06) [0003], [0008], [0017], [0020], [0030], [0074], [0077], [0080]-[0081], [0096], [0098], [0109], [0125], [0134], [0146], [0127], [0150], [0154]; figures 1-2, 6, 8 -----	1-3,5-9, 17-19
X	US 2013/093936 A1 (SCHEELINE ALEXANDER [US] ET AL) 18 April 2013 (2013-04-18) [0002], [0009], [0048]-[0050], [0052], [0077], [0087], [0089]; figures 1A-1B, 9A-9C ----- -/--	1-9,11, 12,14-18

☒ Further documents are listed in the continuation of Box C. ☒ See patent family annex.

* Special categories of cited documents :

"A" document defining the general state of the art which is not considered to be of particular relevance

"E" earlier application or patent but published on or after the international filing date

"L" document which may throw doubts on priority claim(s) or which is cited to establish the publication date of another citation or other special reason (as specified)

"O" document referring to an oral disclosure, use, exhibition or other means

"P" document published prior to the international filing date but later than the priority date claimed

"T" later document published after the international filing date or priority date and not in conflict with the application but cited to understand the principle or theory underlying the invention

"X" document of particular relevance; the claimed invention cannot be considered novel or cannot be considered to involve an inventive step when the document is taken alone

"Y" document of particular relevance; the claimed invention cannot be considered to involve an inventive step when the document is combined with one or more other such documents, such combination being obvious to a person skilled in the art

"&" document member of the same patent family

Date of the actual completion of the international search 8 May 2017	Date of mailing of the international search report 22/05/2017
Name and mailing address of the ISA/ European Patent Office, P.B. 5818 Patentlaan 2 NL - 2280 HV Rijswijk Tel. (+31-70) 340-2040, Fax: (+31-70) 340-3016	Authorized officer Mason, William

1

INTERNATIONAL SEARCH REPORT

International application No
PCT/DK2017/050018

C(Continuation). DOCUMENTS CONSIDERED TO BE RELEVANT

Category*	Citation of document, with indication, where appropriate, of the relevant passages	Relevant to claim No.
X	JP 2007 163181 A (ADVANTEST CORP) 28 June 2007 (2007-06-28) [0029], [0040], [0042]-[0044], [0058], [0081], [0090]-[0091]; figures 8-10	1-13,17, 18
X	US 2003/049693 A1 (GOH M CYNTHIA [CA] ET AL) 13 March 2003 (2003-03-13) [0055], [0058], [0069], [0082], [0093]-[0097], [0099], [0101]-[0102]; figures 1, 2, 6a	1-15
A	US 2006/057707 A1 (CUNNINGHAM BRIAN T [US] ET AL) 16 March 2006 (2006-03-16) [0100]-[0122]; page 9, column 1 - page 11, column 1; claims 1-3, 21-23; figures 1-2, 8-10, 20-21,28-33, 35, 48	1-19
A	US 2008/246961 A1 (ZHANG WEI [US] ET AL) 9 October 2008 (2008-10-09) [0009], [0024], [0039], [0045]-[0046]; figures 1-2	1-19
A	US 2009/079976 A1 (CUNNINGHAM BRIAN T [US] ET AL) 26 March 2009 (2009-03-26) figures 1, 4, 11	1-19
A	US 2012/258549 A1 (LU MENG [US] ET AL) 11 October 2012 (2012-10-11) figures 5-6, 8-9	1-19

1

INTERNATIONAL SEARCH REPORT

Information on patent family members

International application No
PCT/DK2017/050018

Patent document cited in search report	Publication date	Patent family member(s)	Publication date
US 2012309080 A1	06-12-2012	NONE	
US 2013093936 A1	18-04-2013	NONE	
JP 2007163181 A	28-06-2007	JP 4911965 B2	04-04-2012
		JP 2007163181 A	28-06-2007
US 2003049693 A1	13-03-2003	CA 2460233 A1	20-03-2003
		CA 2743332 A1	20-03-2003
		EP 1434994 A2	07-07-2004
		JP 4554205 B2	29-09-2010
		JP 2005502065 A	20-01-2005
		JP 2009282046 A	03-12-2009
		US 2003049693 A1	13-03-2003
		US 2008180692 A1	31-07-2008
		US 2011111487 A1	12-05-2011
		WO 03023400 A2	20-03-2003
US 2006057707 A1	16-03-2006	US 2006057707 A1	16-03-2006
		US 2009264314 A1	22-10-2009
		US 2011201132 A1	18-08-2011
US 2008246961 A1	09-10-2008	US 2008246961 A1	09-10-2008
		WO 2008123927 A1	16-10-2008
US 2009079976 A1	26-03-2009	US 2009079976 A1	26-03-2009
		US 2010221847 A1	02-09-2010
US 2012258549 A1	11-10-2012	NONE	

Bibliography

[1] Hakan Inan, Muhammet Poyraz, Fatih Inci, Mark A. Lifson, Murat Baday, Brian T. Cunningham, and Utkan Demirci. Photonic crystals: emerging biosensors and their promise for point-of-care applications. *Chem. Soc. Rev.*, 46(2):366–388, 2017.

[2] Jennifer L. Osborn, Barry Lutz, Elain Fu, Peter Kauffman, Dean Y. Stevens, and Paul Yager. Microfluidics without pumps: reinventing the T-sensor and H-filter in paper networks. *Lab on a Chip*, 10(20):2659, 2010.

[3] Line Hagner Nielsen, Thomas Rades, Ben Boyd, and Anja Boisen. Microcontainers as an oral delivery system for spray dried cubosomes containing ovalbumin. *European Journal of Pharmaceutics and Biopharmaceutics*, 118:13–20, 2017.

[4] Maria Fernanda Pineda, Leo Li-Ying Chan, Theresa Kuhlenschmidt, Charles J. Choi, Mark Kuhlenschmidt, and Brian T. Cunningham. Rapid Specific and Label-Free Detection of Porcine Rotavirus Using Photonic Crystal Biosensors. *IEEE Sensors Journal*, 9(4):470–477, 2009.

[5] Daniela Threm, Yousef Nazirizadeh, and Martina Gerken. Photonic crystal biosensors towards on-chip integration. *Journal of Biophotonics*, 5(8-9):601–616, aug 2012.

[6] Janos Vörös. The density and refractive index of adsorbing protein layers. *Biophysical Journal*, 87(1):553–561, 2004.

[7] Jennifer Y. Chen, Lynn S. Penn, and Jun Xi. Quartz crystal microbalance: Sensing cell-substrate adhesion and beyond. *Biosensors and Bioelectronics*, 99(August 2017):593–602, 2018.

[8] Jung A. Lee, Seongpil Hwang, Juhyoun Kwak, Se Il Park, Seung S. Lee, and Kwang Cheol Lee. An electrochemical impedance biosensor with aptamer-modified pyrolyzed carbon electrode for label-free protein detection. *Sensors and Actuators, B: Chemical*, 129(1):372–379, 2008.

[9] Kerstin Länge, Bastian E. Rapp, and Michael Rapp. Surface acoustic wave biosensors: A review. *Analytical and Bioanalytical Chemistry*, 391(5):1509–1519, 2008.

[10] Marek Piliarik and Jiří Homola. Surface plasmon resonance (SPR) sensors: approaching their limits? *Optics Express*, 17(19):16505, 2009.

[11] Noemi Kovacs, Daniel Patko, Norbert Orgovan, Sandor Kurunczi, Jeremy J. Ramsden, Ferenc Vonderviszt, and Róbert Horváth. Optical Anisotropy of Flagellin Layers: In Situ and Label-Free Measurement of Adsorbed Protein Orientation Using OWLS. *Analytical Chemistry*, 85(11):5382–5389, jun 2013.

[12] Meikun Fan, Gustavo F.S. Andrade, and Alexandre G. Brolo. A review on the fabrication of substrates for surface enhanced Raman spectroscopy and their applications in analytical chemistry. *Analytica Chimica Acta*, 693(1-2):7–25, 2011.

[13] Christoph Vannahme, Michael C. Leung, Frank Richter, Cameron L C Smith, Pétur G. Hermannsson, and Anders Kristensen. Nanoimprinted distributed feedback lasers comprising TiO2 thin films: Design guidelines for high performance sensing. *Laser and Photonics Reviews*, 7(6):1036–1042, 2013.

[14] Brian T. Cunningham. Label-Free Assays on the BIND System. *Journal of Biomolecular Screening*, 9(6):481–490, 2004.

[15] Ian D. Block, Leo L. Chan, and Brian T. Cunningham. Large-area submicron replica molding of porous low-k dielectric films and application to photonic crystal biosensor fabrication. *Microelectronic Engineering*, 84(4):603–608, 2007.

[16] Garet G Nenninger, Marek Piliarik, and Jiří Homola. Data analysis for optical sensors based on spectroscopy of surface plasmons. *Measurement Science and Technology*, 13(12):2038–2046, dec 2002.

[17] Robert Magnusson and S. S. Wang. New principle for optical filters. *Applied Physics Letters*, 61(9):1022–1024, aug 1992.

[18] Yousef Nazirizadeh, Julia Reverey, Ulf Geyer, Uli Lemmer, Christine Selhuber-Unkel, and Martina Gerken. Material-based three-dimensional imaging with nanostructured surfaces. *Applied Physics Letters*, 102(1), 2013.

[19] Yousef Nazirizadeh, Volker Behrends, Aurél Prósz, Norbert Orgovan, Róbert Horváth, Ann M. Ferrie, Ye Fang, Christine Selhuber-Unkel, and Martina Gerken. Intensity interrogation near cutoff resonance for label-free cellular profiling. *Scientific Reports*, 6(1):24685, jul 2016.

[20] Moritz Paulsen, Sabrina Jahns, and Martina Gerken. Intensity-based readout of resonant-waveguide grating biosensors: Systems and nanostructures. *Photonics and Nanostructures - Fundamentals and Applications*, 26:69–79, 2017.

[21] Róbert Horváth, Henrik C. Pedersen, Nina Skivesen, Dóvid Selmeczi, and Niels Bent Larsen. Optical waveguide sensor for on-line monitoring of bacteria. *Optics Letters*, 28(14):1233, 2003.

[22] Sabrina Jahns, Marion Bräu, Björn-Ole Meyer, Torben Karrock, Sören B. Gutekunst, Lars Blohm, Christine Selhuber-Unkel, Raymund Buhmann, Yousef Nazirizadeh, and Martina Gerken. Handheld imaging photonic crystal biosensor for multiplexed, label-free protein detection. *Biomedical Optics Express*, 6(10):3724, 2015.

[23] Yu Chung Lin, Wen Hsin Hsieh, Lai Kwan Chau, and Guo En Chang. Intensity-detection-based guided-mode-resonance optofluidic biosensing system for rapid, low-cost, label-free detection. *Sensors and Actuators, B: Chemical*, 250:659–666, 2017.

[24] Yue Zhuo, Huan Hu, Weili Chen, Meng Lu, Limei Tian, Hojeong Yu, Kenneth D. Long, Edmond Chow, William P. King, Srikanth Singamaneni, and Brian T. Cunningham. Single nanoparticle detection using photonic crystal enhanced microscopy. *The Analyst*, 139(5):1007–1015, 2014.

[25] Pétur G. Hermannsson, Christoph Vannahme, Cameron L C Smith, Kristian Tølbøl Sørensen, and Anders Kristensen. Refractive index dispersion sensing using an array of photonic crystal resonant reflectors. *Applied Physics Letters*, 107(6):1–4, 2015.

[26] Pétur G. Hermannsson, Kristian Tølbøl Sørensen, Christoph Vannahme, Cameron L.C. Smith, Jan J Klein, Maria-Melanie Russew, Gabi Grützner, and Anders Kristensen. All-polymer photonic crystal slab sensor. *Optics Express*, 23(13):16529–16539, jun 2015.

[27] Robert Magnusson, Debra Wawro, Shelby Zimmerman, and Yiwu Ding. Resonant photonic biosensors with polarization-based multiparametric discrimination in each channel. *Sensors*, 11(2):1476–1488, 2011.

[28] Z S Liu, S. Tibuleac, D Shin, P P Young, and Robert Magnusson. High-efficiency guided-mode resonance filter. *Optics Letters*, 23(19):1556, oct 1998.

[29] Iryna Yaremchuk, Tomas Tamulevičius, Volodymyr Fitio, Ieva Gražulevičiute, Yaroslav Bobitski, and Sigitas Tamulevičius. Guide-mode resonance characteristics of periodic structure on base of diamond-like carbon film. *Optics Communications*, 301-302:1–6, 2013.

[30] Christoph Vannahme, Martin Dufva, and Anders Kristensen. High frame rate multi-resonance imaging refractometry with distributed feedback dye laser sensor. *Light: Science & Applications*, 4(4):e269, 2015.

[31] Róbert Horváth, Lars R. Lindvold, and Niels Bent Larsen. Reverse-symmetry waveguides: Theory and fabrication. *Applied Physics B: Lasers and Optics*, 74(4-5):383–393, 2002.

[32] Róbert Horváth, Henrik C. Pedersen, and Niels Bent Larsen. Demonstration of reverse symmetry waveguide sensing in aqueous solutions. *Applied Physics Letters*, 81(12):2166–2168, 2002.

[33] Yue Zhuo and Brian T. Cunningham. Label-free biosensor imaging on photonic crystal surfaces. *Sensors (Switzerland)*, 15(9):21613–21635, 2015.

[34] Javier Atencia and David J. Beebe. Controlled microfluidic interfaces. *Nature*, 437(7059):648–655, 2005.

[35] Ali Fallah-Araghi, Jean-Christophe Baret, Michael Ryckelynck, and Andrew D. Griffiths. A completely in vitro ultrahigh-throughput droplet-based microfluidic screening system for protein engineering and directed evolution. *Lab on a Chip*, 12(5):882, 2012.

[36] Mira T. Guo, Assaf Rotem, John A. Heyman, and David A. Weitz. Droplet microfluidics for high-throughput biological assays. *Lab on a Chip*, 12(12):2146, 2012.

[37] Bo Zheng, Joshua D. Tice, L. Spencer Roach, and Rustem F. Ismagilov. A droplet-based, composite PDMS/glass capillary microfluidic system for evaluating protein crystallization conditions by microbatch and vapor-diffusion methods with on-chip X-ray diffraction. *Angewandte Chemie - International Edition*, 43(19):2508–2511, 2004.

[38] J. Giddings, F. Yang, and M. Myers. Flow-field-flow fractionation: a versatile new separation method. *Science*, 193(4259):1244–1245, sep 1976.

[39] Erik Häusler, Piotr Domagalski, Marcel Ottens, and André Bardow. Microfluidic diffusion measurements: The optimal H-cell. *Chemical Engineering Science*, 72:45–50, apr 2012.

[40] Jianwei Li and Peter W Carr. Accuracy of Empirical Correlations for Estimating Diffusion Coefficients in Aqueous Organic Mixtures. *Analytical Chemistry*, 69(13):2530–2536, 1997.

[41] R. H. Stokes. An Improved Diaphragm-cell for Diffusion Studies, and Some Tests of the Method. *Journal of the American Chemical Society*, 72(2):763–767, feb 1950.

[42] W Krahn, G Schweiger, and K Lucas. Light scattering measurements of mutual diffusion coefficients in binary liquid mixtures. *Journal of Physical Chemistry*, vol.87(no.22):4515–4519, 1983.

[43] E. O. Stejskal and J. E. Tanner. Spin Diffusion Measurements: Spin Echoes in the Presence of a Time-Dependent Field Gradient. *The Journal of Chemical Physics*, 42(1):288–292, jan 1965.

[44] Marc André Gagnon and Michel Lafleur. Self-Diffusion and Mutual Diffusion of Small Molecules in High-Set Curdlan Hydrogels Studied by 31P NMR. *Journal of Physical Chemistry B*, 113(27):9084–9091, 2009.

[45] Kanji Miyabe, Jun ichi Nagai, and Georges Guiochon. Peak parking-moment analysis: A strategy for the measurement of molecular diffusivity in liquid phase. *Chemical Engineering Science*, 65(12):3859–3864, 2010.

[46] Christopher T Culbertson, Stephen C Jacobson, and J Michael Ramsey. Diffusion coefficient measurements in microfluidic devices. *Talanta*, 56(2):365–73, feb 2002.

[47] R.W. Wood. On a remarkable case of uneven distribution of light in a diffraction grating spectrum. *Philosophical Magazine Series 6*, 4(21):396–402, sep 1902.

[48] Ann M Ferrie, Oberon D Deichmann, Qi Wu, and Ye Fang. High resolution resonant waveguide grating imager for cell cluster analysis under physiological condition. *Applied Physics Letters*, 100(223701):1–4, 2012.

[49] Kristelle Bougot-Robin, Shunbo Li, Yinghua Zhang, I-Ming Hsing, Henri Benisty, and Weijia Wen. “Peak tracking chip” for label-free optical detection of bio-molecular interaction and bulk sensing. *The Analyst*, 137(20):4785–4794, 2012.

[50] Amnon Yariv and Pochi Yeh. *Photonics: Optical electronics in modern communications.* 6th edition, 2007.

[51] Henrik Bruus. *Theoretical Microfluidics.* 2007.

[52] Pétur G. Hermannsson, Christoph Vannahme, Cameron L C Smith, and Anders Kristensen. Absolute analytical prediction of photonic crystal guided mode resonance wavelengths. *Applied Physics Letters*, 105(7):071103, aug 2014.

[53] Kailash K. Sharma. *Optics: Principles and Applications.* Elsevier, 1st edition, 2006.

[54] Daniel Patko, Zsolt Mártonfalvi, Boglarka Kovacs, Ferenc Vonderviszt, Miklós Kellermayer, and Robert Horvath. Microfluidic channels laser-cut in thin double-sided tapes: Cost-effective biocompatible fluidics in minutes from design to final integration with optical biochips. *Sensors and Actuators, B: Chemical*, 196:352–356, 2014.

[55] Peter Friis Østergaard, Joanna Lopacinska-Jørgensen, Jonas Nyvold Pedersen, Niels Tommerup, Anders Kristensen, Henrik Flyvbjerg, Asli Silahtaroglu, Rodolphe Marie, and Rafael J. Taboryski. Optical mapping of single-molecule human DNA in disposable, mass-produced all-polymer devices. *Journal of Micromechanics and Microengineering*, 25(10), 2015.

[56] K. Kistrup, C. E. Poulsen, M. F. Hansen, and A. Wolff. Ultrasonic welding for fast bonding of self-aligned structures in lab-on-a-chip systems. *Lab Chip*, 15(9):1998–2001, 2015.

[57] Chen Wang, Shuangcheng Yu, Wei Chen, and Cheng Sun. Highly Efficient Light-Trapping Structure Design Inspired By Natural Evolution. *Scientific Reports*, 3(1):1025, 2013.

[58] Mehrdad Shokooh-saremi and Robert Magnusson. Particle swarm optimization and its application to the Design of Diffraction Grating Filters. *Optics Letters*, 32(8):894–896, 2007.

[59] Robert Magnusson and Mehrdad Shokooh-Saremi. Physical basis for wideband resonant reflectors. *Optics express*, 16(5):3456–3462, 2008.

[60] Robert Magnusson. Wideband reflectors with zero-contrast gratings. *Optics letters*, 39(15):4337–40, 2014.

[61] Kristian Tølbøl Sørensen. asasim: Adaptive Sampling for Electromagnetic Simulations. *submitted to Computer Physics Communications*, 2017.

[62] Bertrand Rouet-Leduc, Kipton Barros, Emmanuel Cieren, Venmugil Elango, Christoph Junghans, Turab Lookman, Jamaludin Mohd-Yusof, Robert S. Pavel, Axel Y. Rivera, Dominic Roehm, Allen L. McPherson, and Timothy C. Germann. Spatial adaptive sampling in multiscale simulation. *Computer Physics Communications*, 185(7):1857–1864, 2014.

[63] Omar Awile, Ferit Büyükkeçeci, Sylvain Reboux, and Ivo F. Sbalzarini. Fast neighbor lists for adaptive-resolution particle simulations. *Computer Physics Communications*, 183(5):1073–1081, 2012.

[64] D. Rosenblatt, A. Sharon, and A.A. Friesem. Resonant grating waveguide structures. *IEEE JOURNAL OF QUANTUM ELECTRONICS*, 33(11):2038–2059, 1997.

[65] Richard K Johnson. *The Elements of MATLAB Style*. Cambridge University Press, 1st edition, 2011.

[66] Kristian Tølbøl Sørensen, Charlotte Bonde Ingvorsen, Line Hagner Nielsen, and Anders Kristensen. On the practical achievement of high performance using a polymeric photonic crystal slab sensor. *submitted to Optics Express*, 2017.

[67] Christoph Vannahme, Kristian Tølbøl Sørensen, Carsten Gade, Martin Dufva, and Anders Kristensen. Refractometric monitoring of dissolution and fluid flow with distributed feedback dye laser sensor. *Optics Express*, 23(5):6562+, 2015.

[68] Christoph Vannahme, Martin Dufva, and Anders Kristensen. Multi-wavelength Distributed Feedback Dye Laser Sensor for High Frame Rate Label-free Imaging. *Laser & Photonics Reviews*, pages 1–4, 2014.

[69] Timothy M. Chinowsky, Linda S. Jung, and Sinclair S. Yee. Optimal linear data analysis for surface plasmon resonance biosensors. *Sensors and Actuators, B: Chemical*, 54(1):89–97, 1999.

[70] Masahiko Daimon and Akira Masumura. Measurement of the refractive index of distilled water from the near-infrared region to the ultraviolet region. *Applied Optics*, 46(18):3811, 2007.

[71] Andrew Evan Kamholz, Bernhard H. Weigl, Bruce A. Finlayson, and Paul Yager. Quantitative analysis of molecular interaction in a microfluidic channel: The T-sensor. *Analytical Chemistry*, 71(23):5340–5347, 1999.

[72] Andrew Evan Kamholz, Eric A Schilling, and Paul Yager. Optical Measurement of Transverse Molecular Diffusion in a Microchannel. *Biophysical Journal*, 80:1967–1972, 2001.

[73] Daniel A. Beard. Taylor dispersion of a solute in a microfluidic channel. *Journal of Applied Physics*, 89(8):4667–4669, apr 2001.

[74] Kevin D. Dorfman and Howard Brenner. Comment on "taylor dispersion of a solute in a microfluidic channel" [J. Appl. Phys. 89, 4667 (2001)]. *Journal of Applied Physics*, 90(12):6553–6554, 2001.

[75] Daniel A. Beard. Response to “Comment on ‘Taylor dispersion of a solute in a microfluidic channel’ [J. Appl. Phys. 90 , 6553 (2001)]”. *Journal of Applied Physics*, 90(12):6555–6556, dec 2001.

[76] Morten Hannibal Madsen, Nikolaj a Feidenhans’l, Poul-Erik Hansen, Jørgen Garnæs, and Kai Dirscherl. Accounting for PDMS shrinkage when replicating structures. *Journal of Micromechanics and Microengineering*, 24(12):127002, 2014.

[77] J. B. Taylor and J. S. Rowlinson. The thermodynamic properties of aqueous solutions of glucose. *Transactions of the Faraday Society*, 51(0):1183–1192, 1955.

[78] Rustem F. Ismagilov, Abraham D. Stroock, Paul J. a. Kenis, George Whitesides, and Howard a. Stone. Experimental and theoretical scaling laws for transverse diffusive broadening in two-phase laminar flows in microchannels. *Applied Physics Letters*, 76(17):2376–2378, 2000.

[79] Kanji Miyabe and Ryo Isogai. Estimation of molecular diffusivity in liquid phase systems on the basis of the absolute rate theory. *Analytical sciences : the international journal of the Japan Society for Analytical Chemistry*, 29(4):467–72, 2013.

[80] Yutaka Kazoe and Minami Yoda. Measurements of the near-wall hindered diffusion of colloidal particles in the presence of an electric field. *Applied Physics Letters*, 99(124104):1–3, 2011.

[81] Patrick T. Spicer, William B. Small II, William B. Small, Matthew L. Lynch, and Janet L. Burns. Dry powder precursors of cubic liquid crystalline nanoparticles (cubosomes). *Journal of Nanoparticle Research*, 4(4):297–311, 2002.

[82] Christoffer von Halling Laier, Marco van de Weert, Ben J. Boyd, Thomas Rades, Anja Boisen, and Line Hagner Nielsen. Spray drying of a nanoparticulate dry powder vaccine formulation. *(submitted)*, 2018.

[83] Yousef Nazirizadeh, Uwe Bog, Sylwia Sekula, Timo Mappes, Uli Lemmer, and Martina Gerken. Low-cost label-free biosensors using photonic crystals embedded between crossed polarizers. *Opt. Express*, 18(18):19120–19128, 2010.

[84] Dustin Gallegos, Kenneth D. Long, Hojeong Yu, Peter P. Clark, Yixiao Lin, Sherine George, Pabitra Nath, and Brian T. Cunningham. Label-free biodetection using a smartphone. *Lab on a Chip*, 13(11):2124, 2013.

[85] Corning. *Corning Epic System Commercial Specifications*.

[86] Huaying Zhao, Patrick H. Brown, and Peter Schuck. On the distribution of protein refractive index increments. *Biophysical Journal*, 100(9):2309–2317, 2011.

Index

Published by:
DTU Nanotech
Department of Micro- and Nanotechnology
Technical University of Denmark
Ørsteds Plads, building 345C
DK-2800 Kgs. Lyngby